

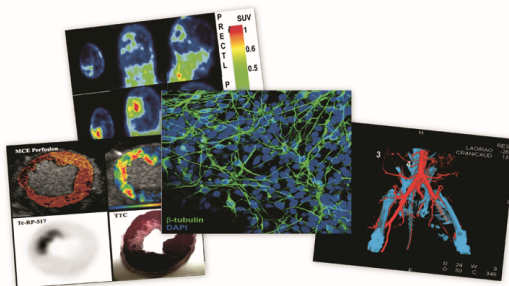
Colour Illustrations *from*

Stem Cell Labeling for Delivery and Tracking Using Non-Invasive Imaging

Dara L. Kraitchman and Joseph Wu

SERIES IN MEDICAL PHYSICS AND BIOMEDICAL ENGINEERING

STEM CELL LABELING FOR DELIVERY AND TRACKING USING NON-INVASIVE IMAGING



Edited by
Dara L. Kraitchman and Joseph C. Wu

 **CRC Press**
Taylor & Francis Group
A TAYLOR & FRANCIS BOOK

This document reproduces full color images from *Stem Cell Labeling for Delivery and Tracking Using Non-Invasive Imaging* that are reproduced in greyscale in the book.

Introduction

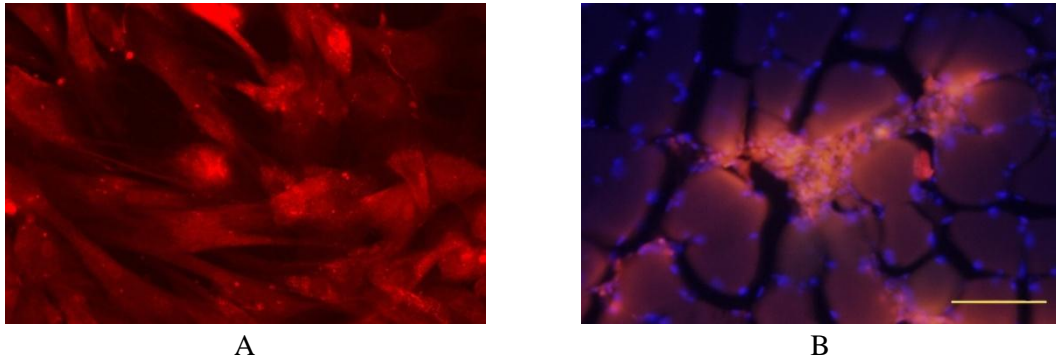


Figure I.1 **A** Mesenchymal stem cells (MSCs) exogenously labeled with cell tracker orange (CTO) appears bright orange using an epifluorescent microscope. **B** Photomicrograph showing orange fluorescent is present in both skeletal muscle and MSCs. However, only the MSCs were exogenously labeled with CTO. When implanted in vivo, the CTO label was released from dying MSCs and taken up by bystander cells. Thus, with direct labeling schemes, the label may no longer reflect the distribution of the labeled cells. Cell nuclei appear blue due to DAPI staining.

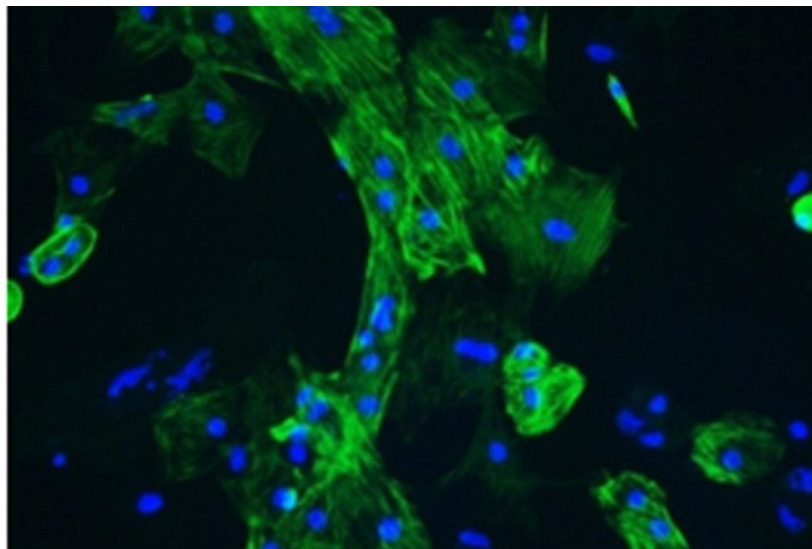


Figure I.2 A cell expressing the reporter gene for green fluorescent protein (GFP) appears bright green microscopically. One theoretical advantage of reporter gene imaging is that only viable cells will produce the reporter gene product, thereby limiting the bystander effect of direct labeling. (Cell nuclei appear blue due to DAPI staining.)

1

Human Embryonic Stem Cells

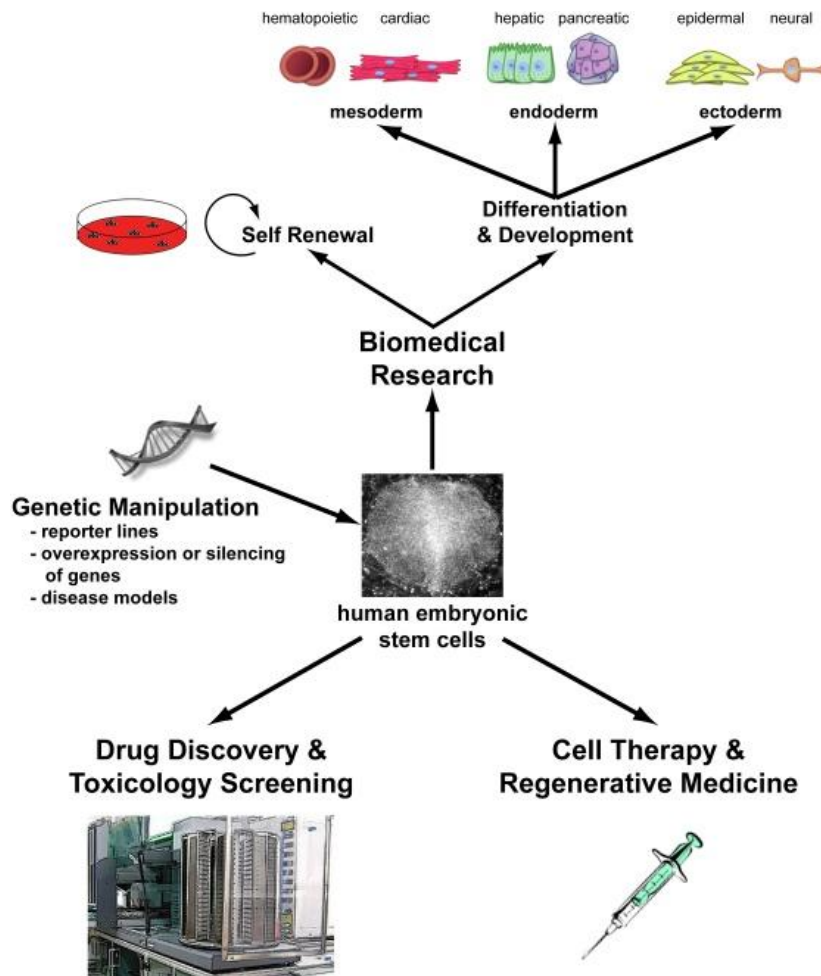


Figure 1.1 Applications for human embryonic stem cells (hESCs) and their derivatives in research and medicine. hESCs are amenable to genetic manipulation, allowing for the generation of cell lines that will be useful tools for assisting in deriving lineages and cell types of interest for developmental biology, drug discovery and regenerative medicine. For example, the introduction of reporter genes under the control of a lineage-specific promoter enables screening for factors involved in differentiation and self-renewal. Additionally, ectopic expression or silencing of key developmental genes can assist in developing directed differentiation protocols. Genetic modification can also be used to generate in vitro models of monogenetic diseases, and potentially to correct disorders in transplantable cells for therapy. As optimised differentiation protocols are developed, both genetically-modified and unmodified hESC-derived cardiac or hepatic cells are likely to be used in high throughput systems to test the efficacy and toxicity of different drugs/chemicals. Some hESC-derived cells (e.g., some neural cell types) could also be used for transplantations, however for most tissues, cell therapy is a long-term prospect. is a long-term prospect.

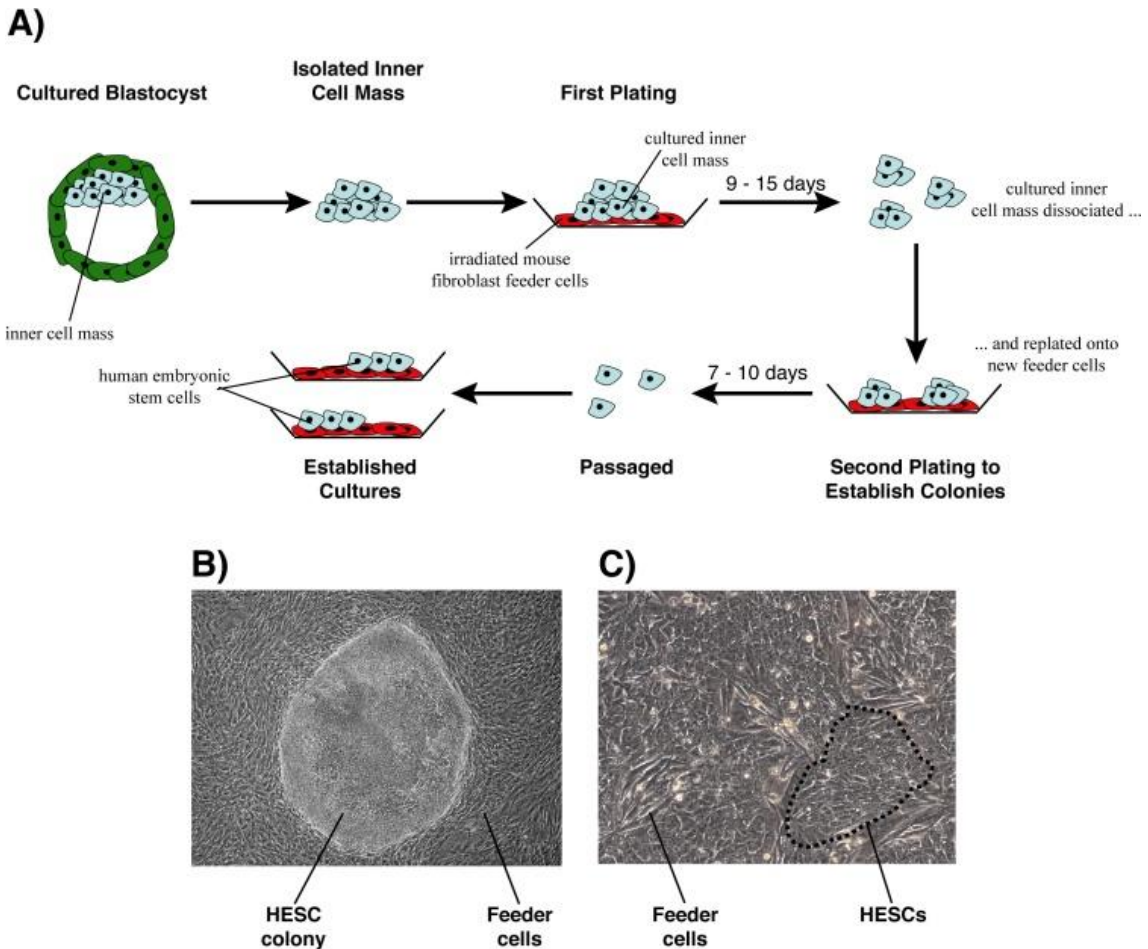


Figure 1.2 Derivation of human embryonic stem cells (hESCs). **A** The most common source of hESCs is the ICM of the blastocyst. To initiate new hESC lines, the cells of the ICM are plated on a feeder layer. As the ICM cells attach, they form colonies that can be isolated and passaged to derive new hESC lines. **B** An example of an undifferentiated hESC colony. **C** An example of enzymatically passaged hESCs grown on irradiated mouse fibroblast feeder cells.

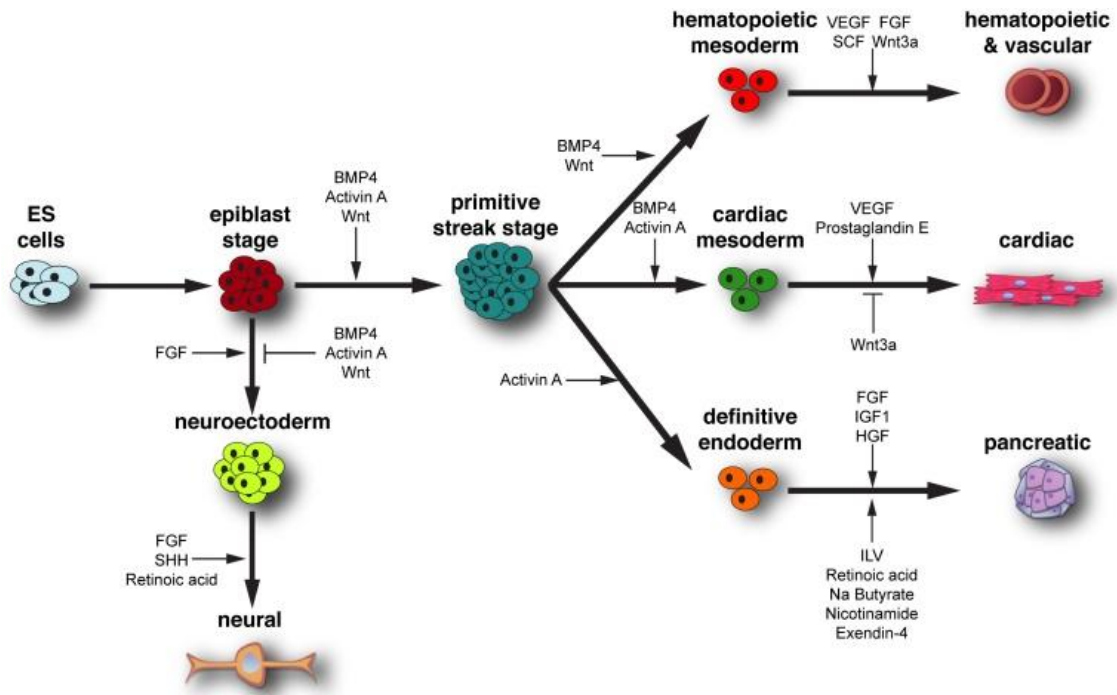


Figure 1.3 A schematic representation of in vitro ESC differentiation and factors involved in the generation of specific cell types. BMP, Activin A, or Wnt signals induce an epiblast-like cell population to commit to a primitive streak-like population, and subsequently to the mesoderm or definitive endoderm cell lineages. High concentrations of BMP are known to promote the formation of posterior-ventral hematopoietic mesoderm, while high amounts of Activin A induce definitive endoderm. A combination of BMP and Activin A induce anterior-dorsal cardiac mesoderm. If these signals are absent, the epiblast-like cells will differentiate to a neuroectodermal fate. Some of the growth factors and small molecules known to either promote or inhibit the formation of more differentiated cell types from the three germ layers are also depicted in the figure and referred to in the text.

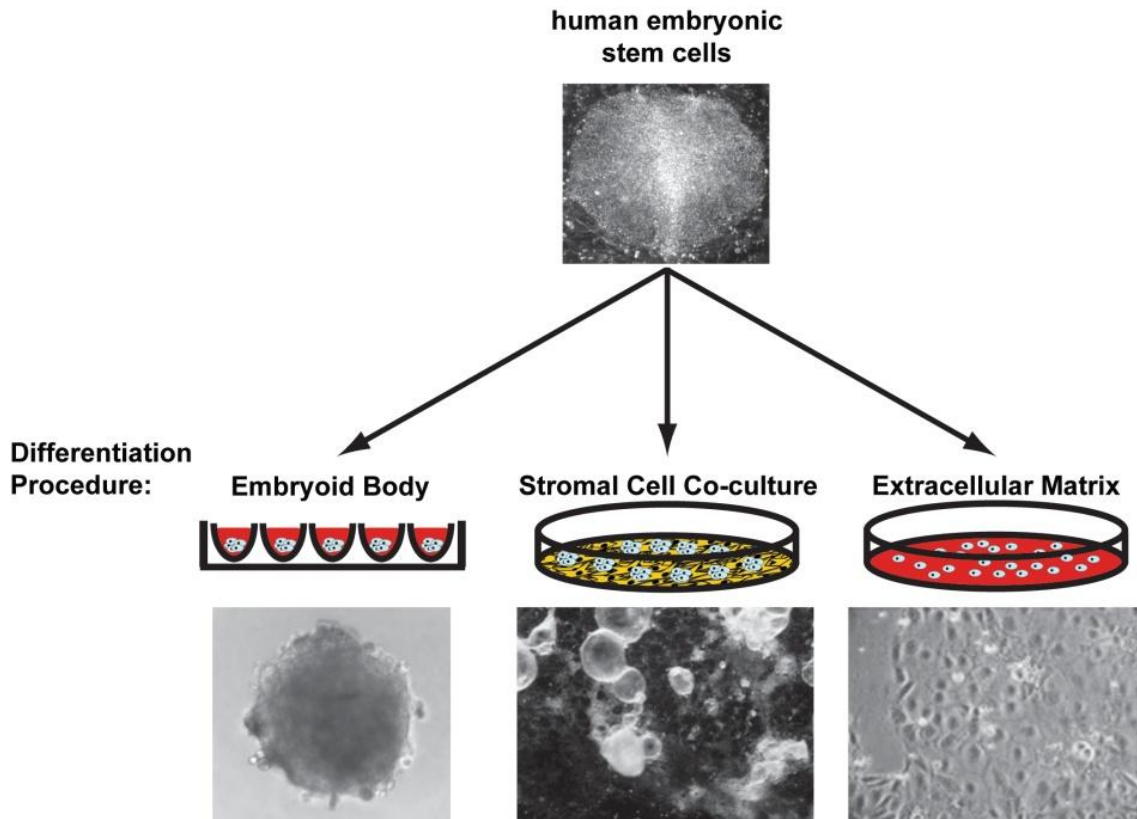


Figure 1.4 Three protocols for differentiating human embryonic stem cells (hESCs). Embryoid bodies (EBs) are initiated by culturing aggregates of hESCs in suspension. EBs are most commonly generated by suspension culture in bacterial grade dishes, as hanging drops, or by forced aggregation in round- or conical-bottomed multi-well plates (“Spin EBs”). An embryoid body generated by the “Spin EB” method is displayed in the left image. The embryoid bodies develop a 3-dimensional structure with the outer layer of cells though to be endodermal. Stromal cell co-culture differentiation involves plating the hESCs on a monolayer of cells that promotes differentiation of the hESCs to the desired cell type. The centre image shows hESCs being cultured on END-2 cells to promote cardiac differentiation. The third method involves culturing hESCs on extracellular matrix proteins. hESCs differentiated on Matrigel in the presence of BMP4 are pictured in the image on the right. Centre photo is courtesy of D. Ward; photo on the right is courtesy of S.R. Braam.

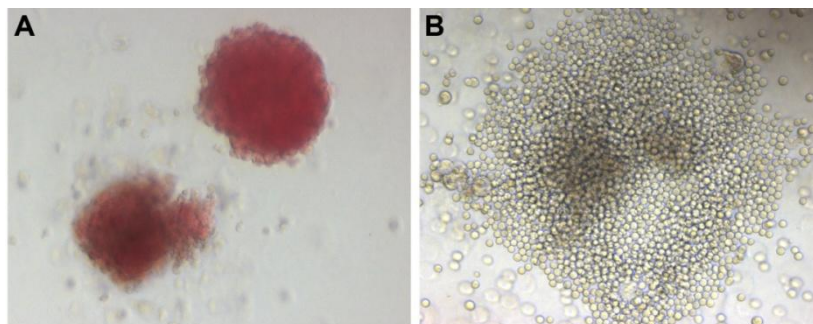


Figure 1.5 Hematopoietic cell types generated from hESCs. Differentiated hESCs were seeded as single cells in methylcellulose cultures containing hematopoietic-promoting growth factors. Erythroid (A) and myeloid (B) colonies can develop from these single cells. Original magnification 100x.

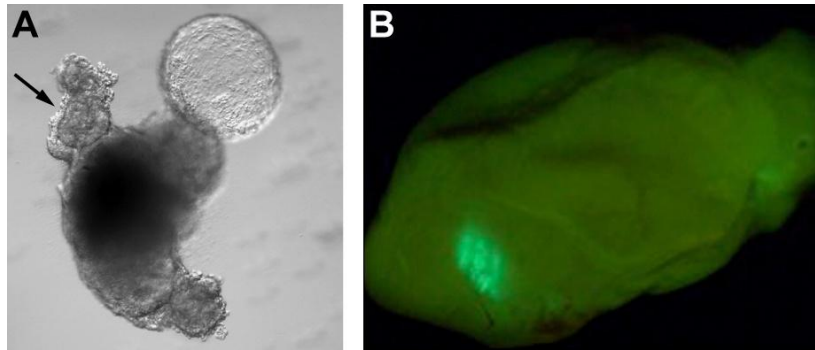


Figure 1.6 Differentiation of hESCs to cardiomyocytes and transplantation of hESC-derived cardiomyocytes. **A** Spontaneously contracting areas (black arrow) developed in hESCs differentiated as Spin EBs following culture in chemically defined media containing BMP4, VEGF, SCF, and Activin A. **B** hESC-CMs derived from a hESC line that expresses GFP were transplanted into a mouse infarcted heart model. The grafted cells, detected by GFP epifluorescence, were still present three weeks after transplantation. Panel B is courtesy of L. W. van Laake.

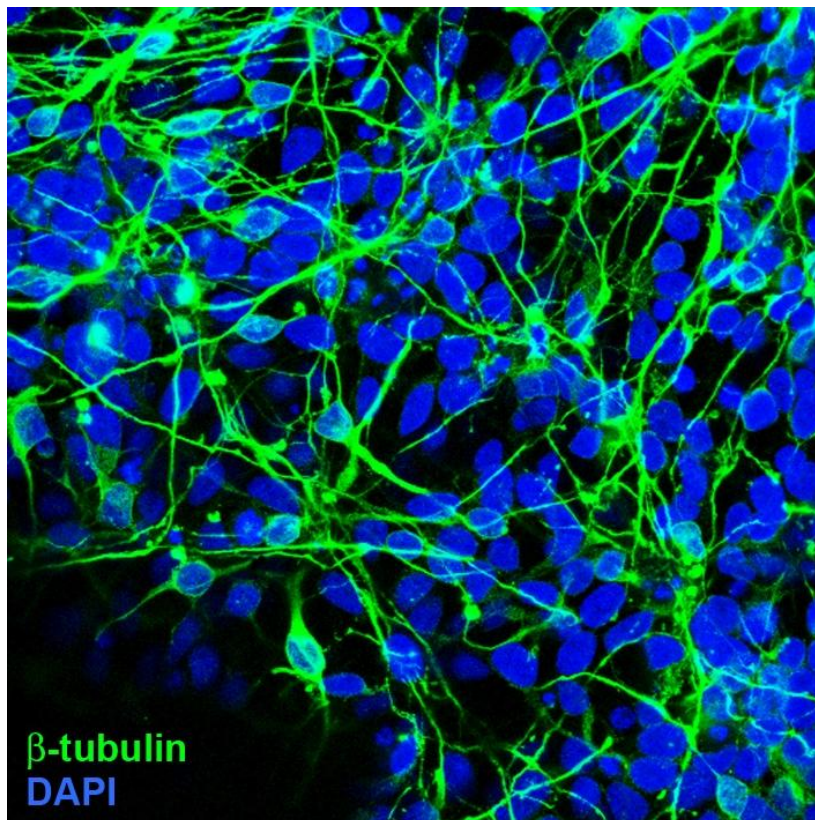


Figure 1.7 hESCs differentiated to neural cell types stained for the presence of β -tubulin, a marker expressed on neural cells. Image is courtesy of S.R. Braam.

2

Stem Cell Basics: Mesenchymal Stem Cells From Bone Marrow

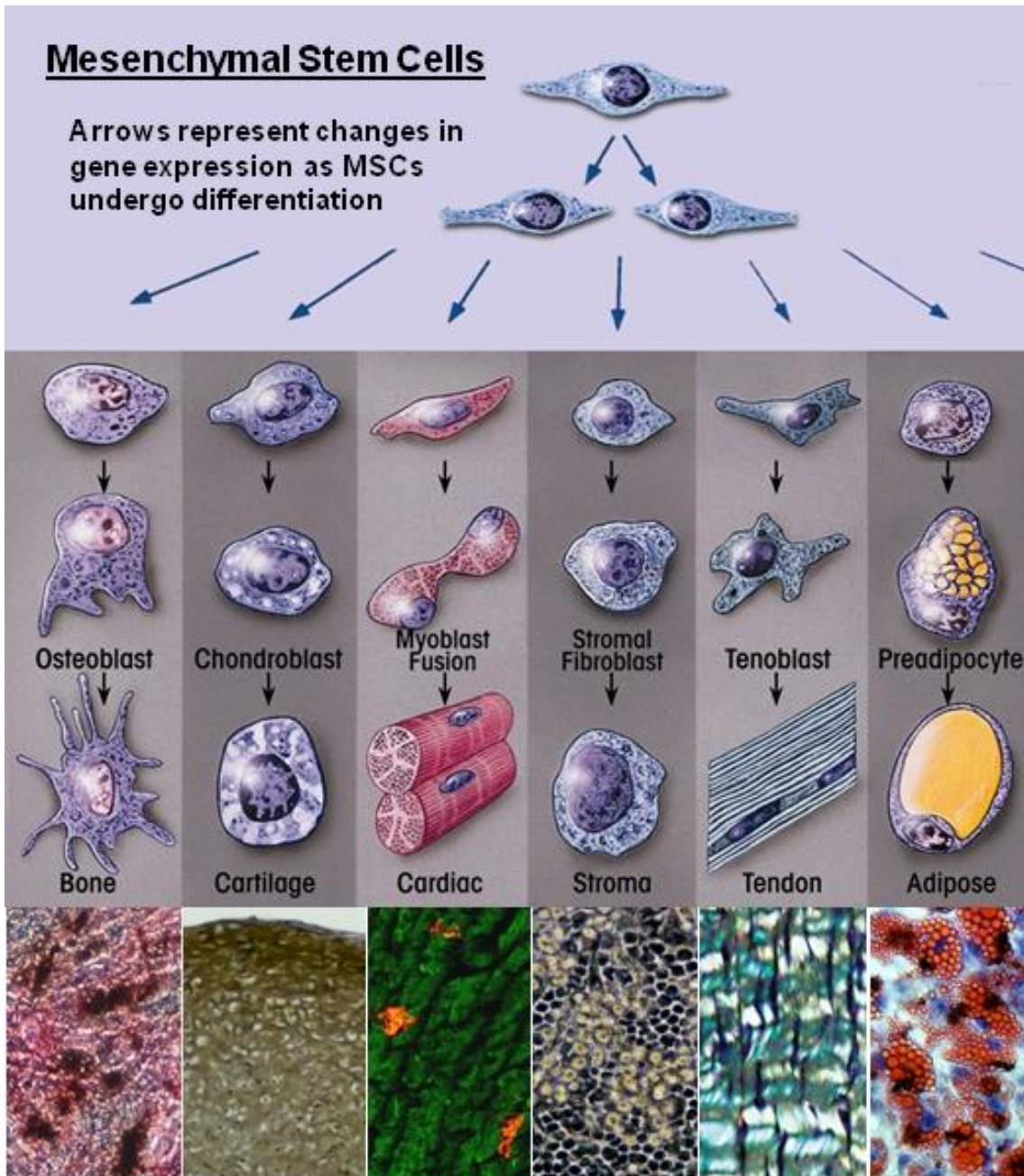


Figure 2.1 Mesenchymal stem cell differentiation to multiple lineages. Nucleated cells from a human bone marrow aspirate are cultured under appropriate conditions and produce a homogeneous population of cells as analyzed by flow cytometry. The cells can be cultured in different conditions to cause differentiation to particular lineages such as, left to right, osteoblasts, chondrocytes, cardiac muscle (in vivo), hematopoietic supporting stroma, tenocytes, and adipocytes.

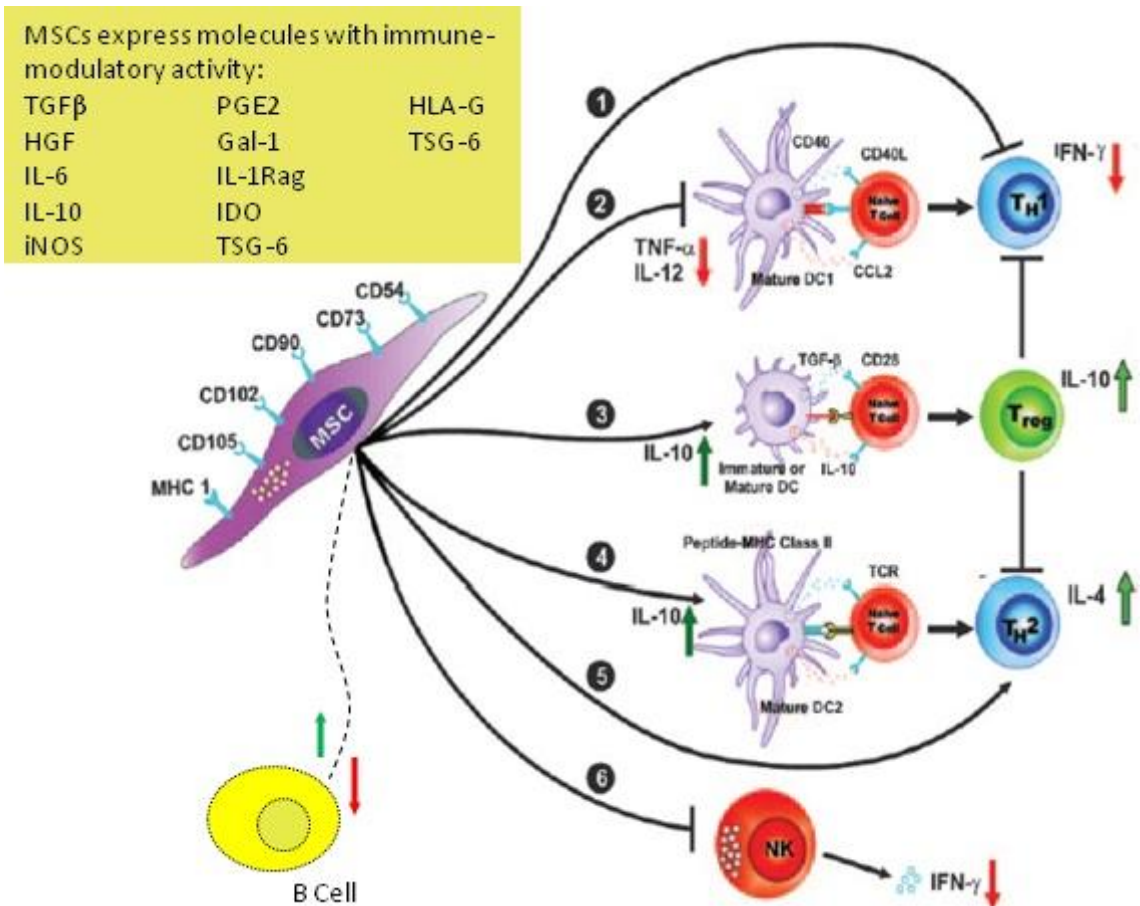


Figure 2.4 MSCs interact with immune cells in a complex manner. MSCs interact with T lymphocytes to reduce the inflammatory response by decreasing IFN γ expression from TH1 cells and increasing the expression of anti-inflammatory molecules IL-10 from T_{REG} and IL-4 from TH2 cells (pathway 1, 3, and 5) MSCs can also decrease the expression of TNF α and IL-12 from DC1 cells (pathway 2). MSCs can interact with immature DCs (pathway 3) to cause release of IL-10 and promote T_{REG} induction from immature T cells, and release of additional IL-10. MSCs interaction with NK cells decreased IFN γ expression and inhibited NK proliferation due to HLA-G (pathway 6). MSCs inhibit B-cell proliferation and maturation resulting in less secretion, but can also increase B-cell maturation responses in other conditions. *Updated from (Aggarwal and Pittenger 2004).*

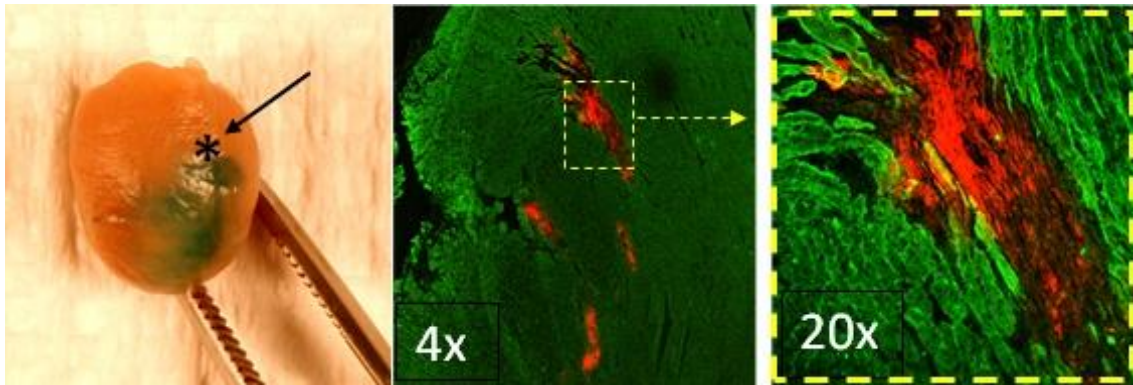


Figure 2.5 Migration (homing) of MSCs to sites of tissue injury. Human MSCs were transduced with the lacZ gene and infused via the tail vein into athymic rats. Three days later the rat received an experimental infarct by tying off the left anterior descending artery (at * in the left panel) for 30 minutes. The animal was allowed to recover and after 2 weeks was sacrificed and the heart stained overnight to reveal the location of lacZ containing cells (left panel). The hearts was then sectioned and stained with antibody to lacZ (red staining in center (4x objective) and right panel (20x objective). Note that the MSCs reside almost exclusively in the remodeling infarcted tissue

3

Hematopoietic Stem Cells

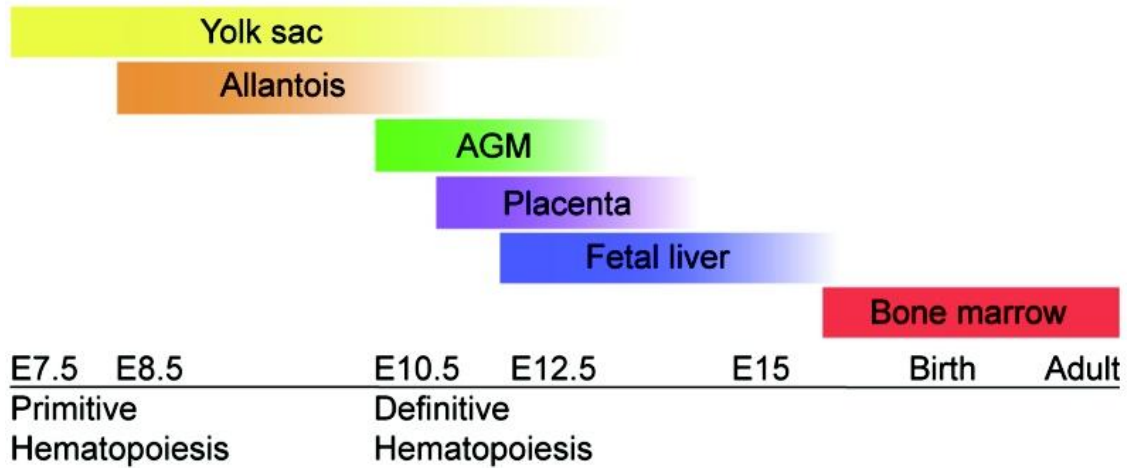


Figure 3.1 Timeline of murine hematopoietic development. Extraembryonic HSCs begin to give rise to blood around E7.5 in a wave known as primitive hematopoiesis. Both the yolk sac and allantois show early hematopoietic potential. Definitive hematopoiesis begins at E10.5 in the aorta-gonadal-mesonephros (AGM) region, later shifting to the fetal liver and finally to the bone marrow, where HSCs reside throughout adulthood.

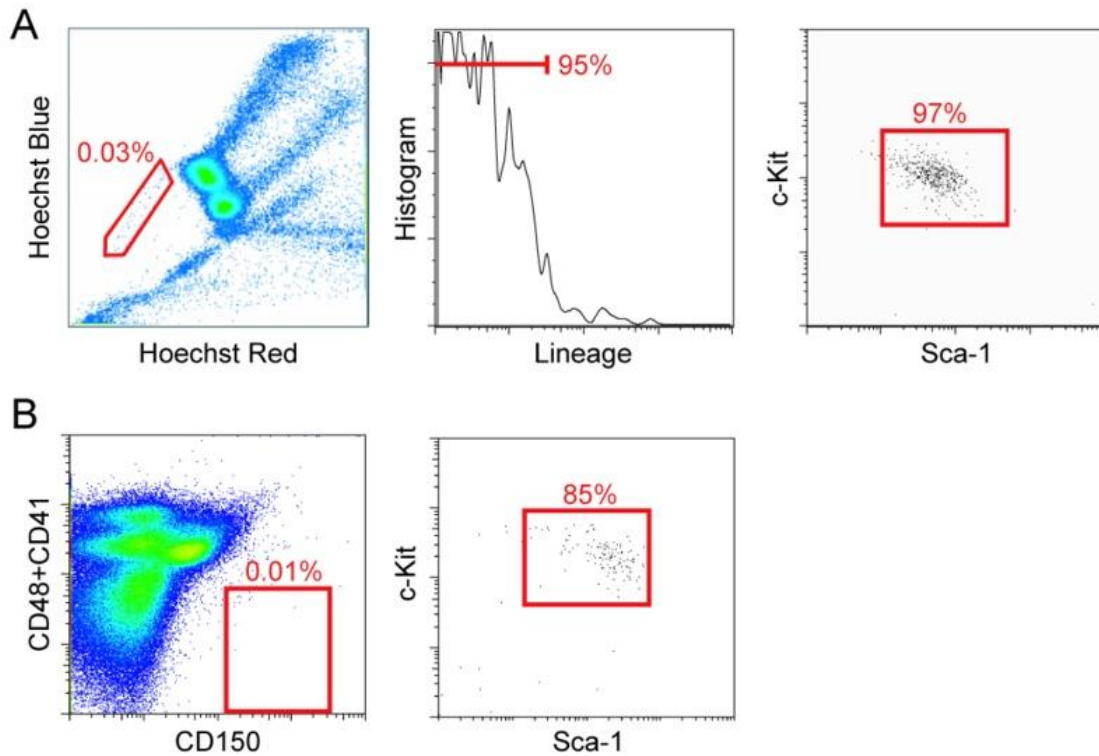


Figure 3.5 HSCs can be identified and isolated using several different flow cytometry marking systems. **A** HSCs preferentially efflux the fluorescent dye Hoechst 33342, allowing resolution of the “Side Population (SP)” of cells (gate) with low Hoechst fluorescence. SP cells represent a highly enriched stem cell population, and are largely negative for lineage markers, while displaying the positive stem cell markers Sca-1 and c-kit. SP cells are also predominantly CD34-/low and Flk2-. **B** HSCs can also be identified using the SLAM surface marker system. CD150+, CD48-, CD41- cells are strongly enriched for the positive HSC markers Sca-1 and c-kit (normally this population is only approximately 0.3% of whole bone marrow). Like the SP, SLAM cells are also CD34-/low and Flk2-.

4

Adipose-Derived Adult Stem Cells

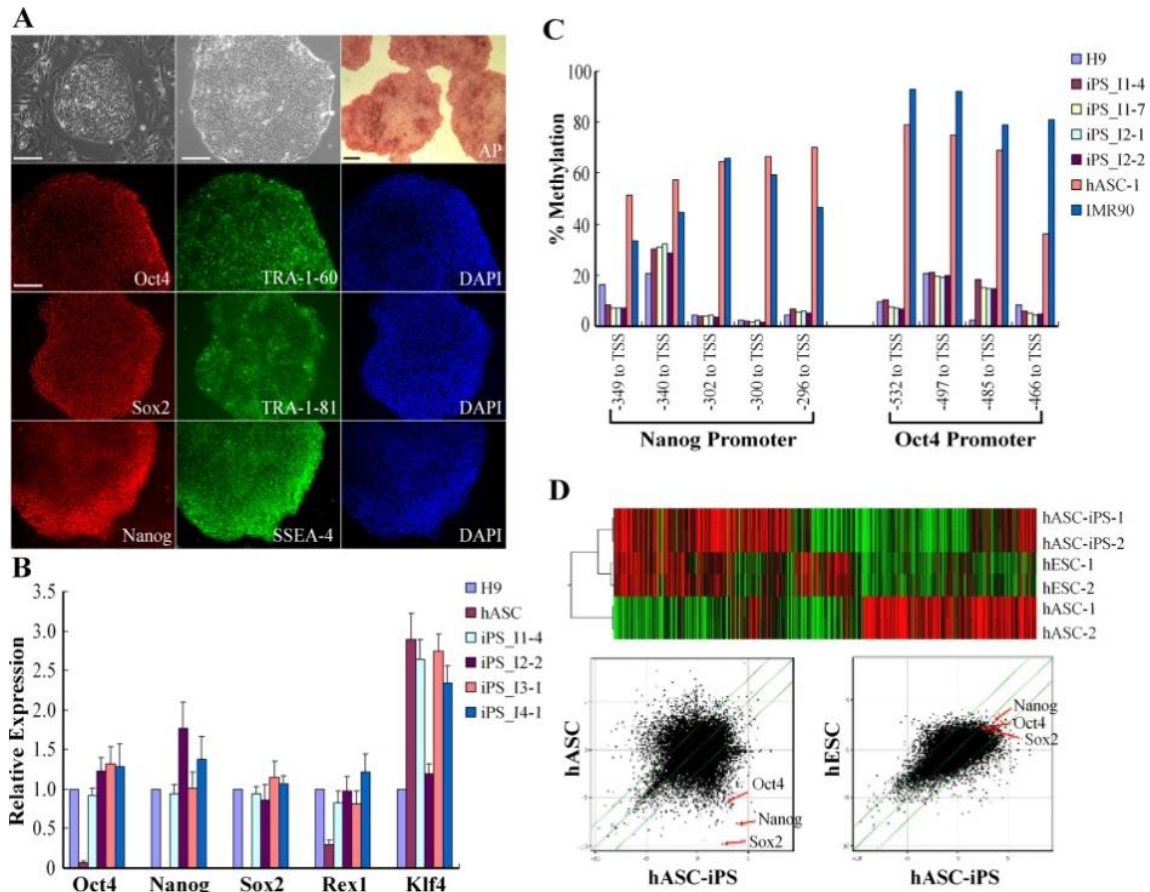


Figure 4.1 Characterization of human adipose stromal cell derived induced pluripotent stem cells (hASC-iPS cells). **A** Immunostaining of hASC-iPS cell colonies with common hES cell markers. The two phase contrast microscopies show a typical hASC-iPS cell colony growing on MEF feeder cells and feeder-free Matrigel surface, respectively (bars, 100 μm). **B** Quantitative-PCR analyzing pluripotency gene expression level within hASCs and hASC-iPS cells relative to those in H9 hES cells. iPS_11-4 denotes iPS cell line #4 derived from individual 1. **C** Bisulphite pyrosequencing measuring methylation status within the promoter region of Oct4 and Nanog genes in H9 hES cells, hASC-iPS cells, hASCs, and IMR90 cells. TSS, transcription start site. **D** Microarray data comparing global gene expression profiles of hASCs, hASC-iPS cells, and hES cells. Upper panel, heat map and hierarchical clustering analysis by Pearson correlation showing hASC-iPS cells are similar to hES cells and distinct from hASCs. Lower panel, scatter plots comparing global gene expression patterns between hASCs, hASC-iPS cells, and hES cells. Highlighted are the pluripotency genes Oct4, Sox2 and Nanog (red arrows). The green diagonal lines indicated linear equivalent and 5-fold changes in gene expression levels between paired samples.

6

Induced Pluripotent Stem Cells: Imaging Nuclear Reprogramming To Cardiac Regeneration

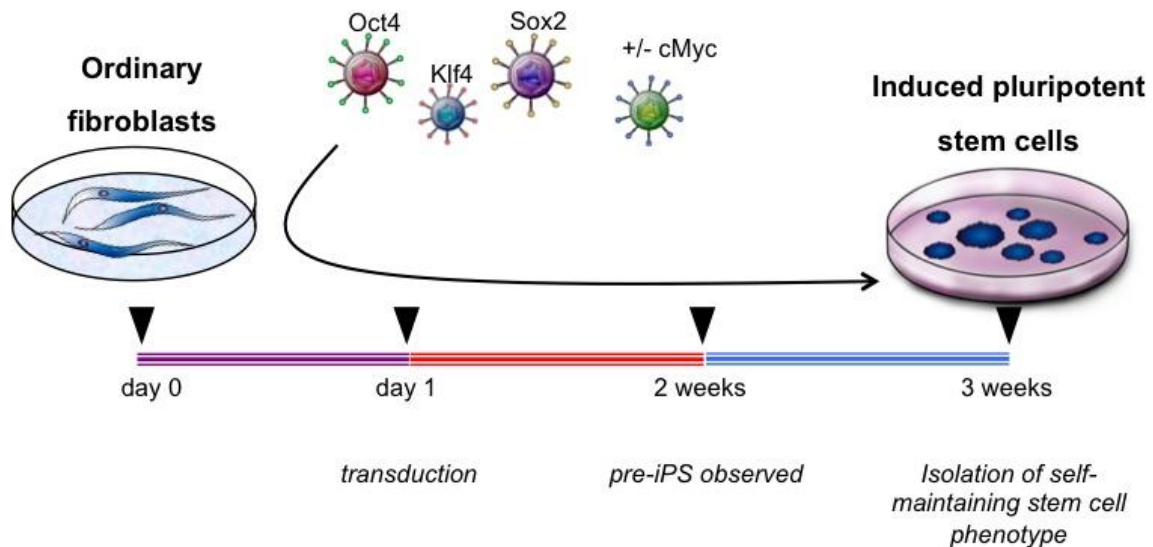


Figure 6.1 Nuclear reprogramming of somatic tissue into stem cell-like progenitors. Ordinary fibroblasts, derived from multiple sources including adult patient-specific tissues, are transduced with ectopic stemness factors, Oct3/4, Sox2, and Klf4 with or without c-Myc. The coerced expression of stemness-related factors induces global changes within the somatic cells over 2-4 weeks, and results in the production of a self-maintaining stem cell-like population. Clonal expansion of these induced pluripotent stem (iPS) cells demonstrates the ability to propagate indefinitely and allows subsequent detailed analysis of full stem cell functionality.

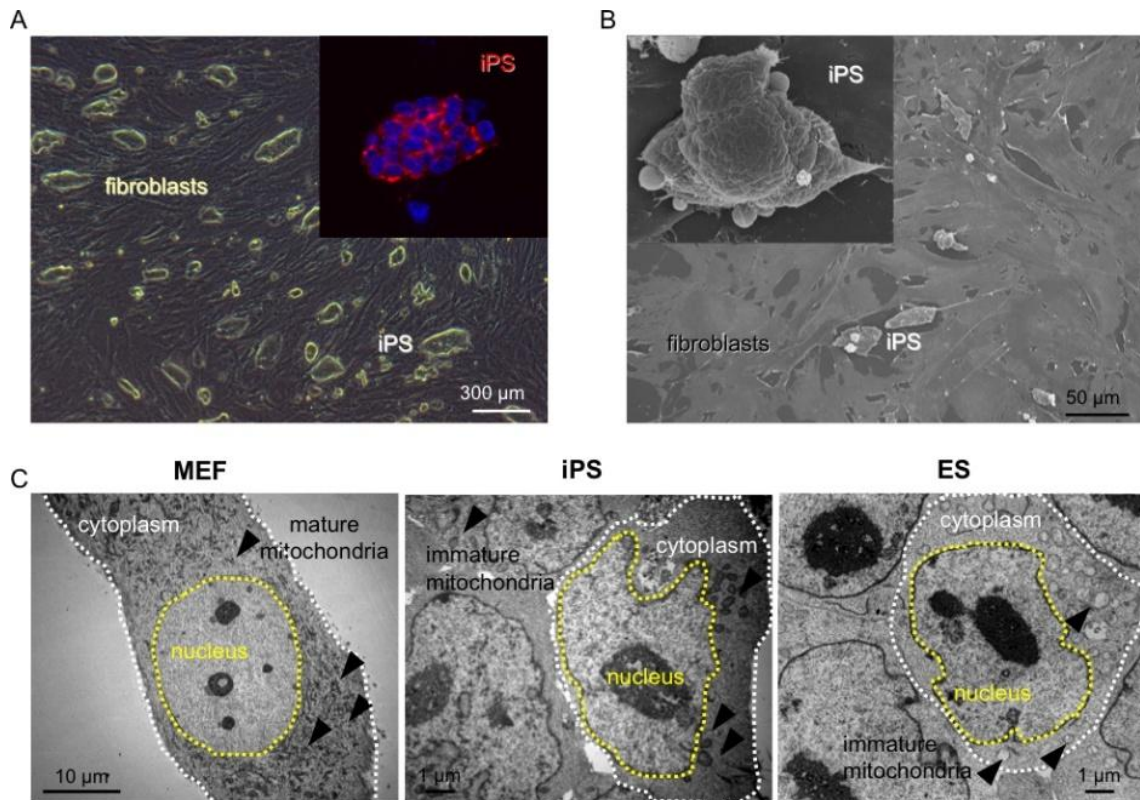


Figure 6.2 Microscopy to visualize induced pluripotent stem cell phenotype. **A** Bright field imaging demonstrates the characteristic growth pattern of induced pluripotent stem cells (iPS) as compact colonies on a monolayer of feeder cells. Confocal microscopy with immunofluorescence detection of pluripotent-associated antigens illustrates the established cell localization pattern of SSEA1 on iPS cells. **B** Scanning electron microscopy demonstrates at high resolution the densely compacted clusters of iPS as outgrowths from the parental fibroblast monolayer upon nuclear reprogramming. **C** Field emission scanning microscope of thin sections of parental fibroblasts illustrates a relatively small nuclear volume compared to large volume of the densely packed cytoplasm with mature mitochondria (left). Embryonic stem cells demonstrate low cytoplasmic density of immature mitochondria with a relatively large nuclear to cytoplasmic ratio (right). iPS recapitulate the pattern of embryonic stem (ES) cells with similar nuclear to cytoplasmic ratio and low density of immature mitochondria (middle).

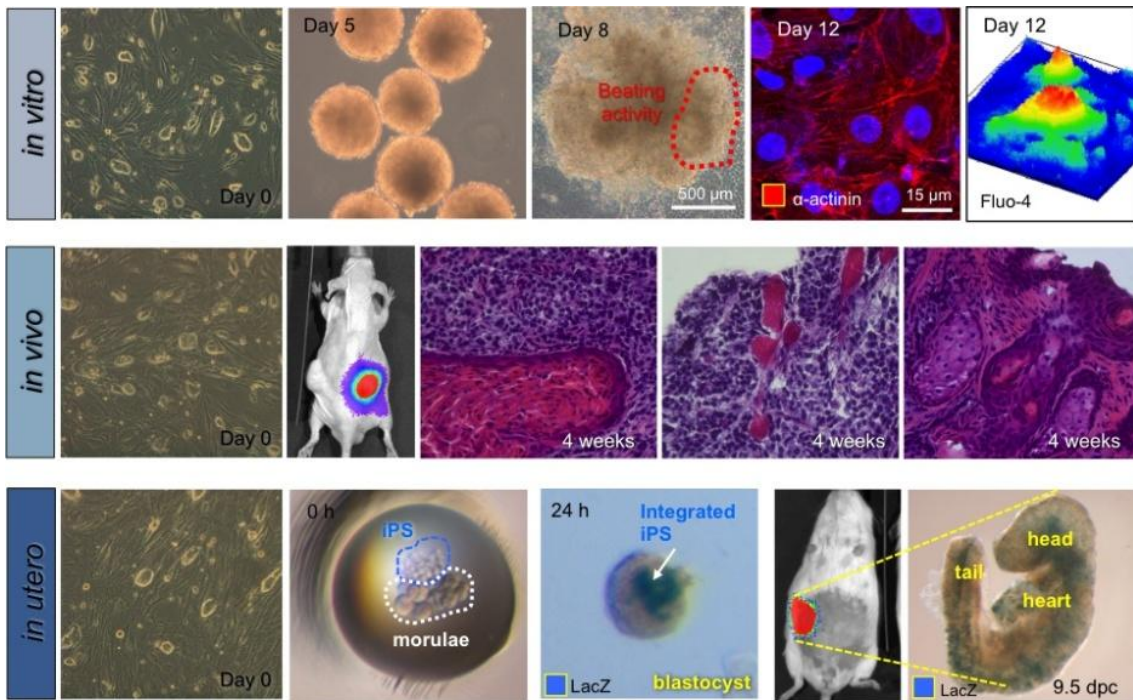


Figure 6.3 Imaging iPS differentiation from *in vitro* analysis to chimeric offspring. **A** Differentiating iPS *in vitro* produces day 5 embryoid bodies capable of multi-lineage differentiation, with *bona fide* cardiogenesis demonstrated by beating activity at day 8, expression of cardiac sarcomeric proteins (middle panels), and functional excitation-contraction coupling demonstrated by calcium transients (far right panel). **B** Injection of iPS into the subcutaneous tissue of immunodeficient host produces engraftment of labeled progeny detected by bioluminescence 4 weeks after transplantation. The stable engraftment enables teratoma formation to depict tri-lineage differentiation *in vivo* and validate pluripotent differentiation capacity of iPS. **C** Transplantation of labeled iPS into host morula demonstrates the functional equivalency of iPS compared to native blastomeres as the chimeric tissue develops through gastrulation and gives rise to early stage embryos. The growth of iPS-derived chimeric embryos can be monitored in real-time with *in vivo* imaging according to luciferase expression within pregnant mothers throughout development and confirmed with lacZ staining (far right panels).

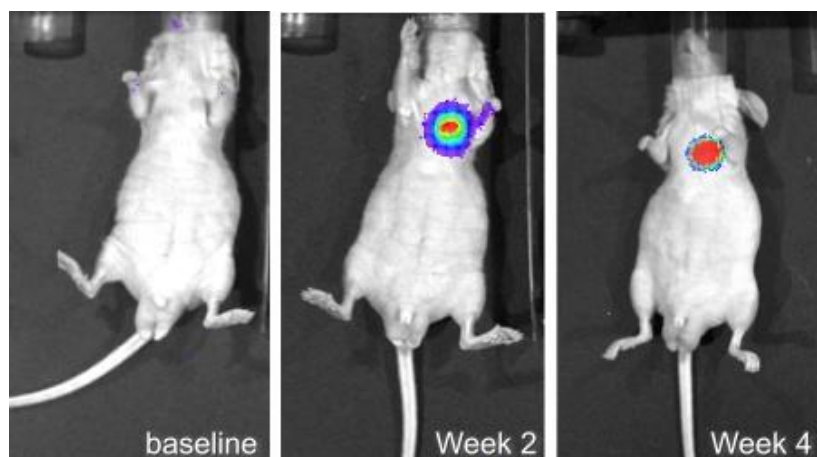


Figure 6.4 Imaging iPS engraftment with *in vivo* optical technology. Time course of intra-cardiac transplanted iPS labeled with luciferase enables high sensitivity detection of stably engrafted progeny over a 4 week follow-up. The lack of detectable cells in non-cardiac tissue suggests no metastatic dissemination within this model system of acute myocardial infarction. Stable expression of luciferase activity within the heart field suggests engraftment and persistent retention of iPS progeny.

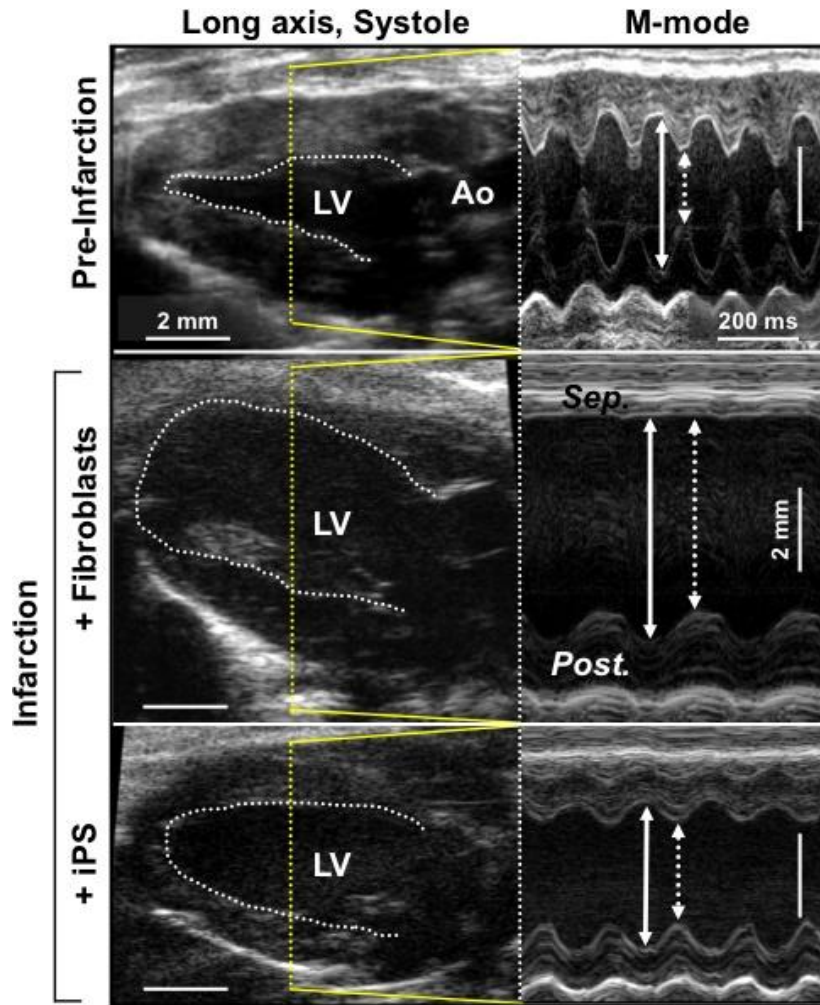


Figure 6.5 Echocardiography of cardiac structure and function following iPS-based treatment of acute myocardial infarction. Long axis views of mouse hearts prior to infarction demonstrates normal systolic function with representative M-mode imaging illustrating synchronized septal and posterior wall motion at the mid left ventricle (top row). Hearts infarcted by surgical ligation of the anterior coronary arteries consistently demonstrate decreased regional septal wall motion that does not significantly improve following transplantation with fibroblasts (middle row). Transplantation of iPS progeny into the peri-infarcted tissue of the left ventricle leads to recovery of anterior wall and septal wall motion with restoration of systolic function (bottom row). Solid arrow = diastole, dotted arrow = systole, LV = left ventricle, Ao = aorta, Sep = septal wall, Post. = posterior wall.

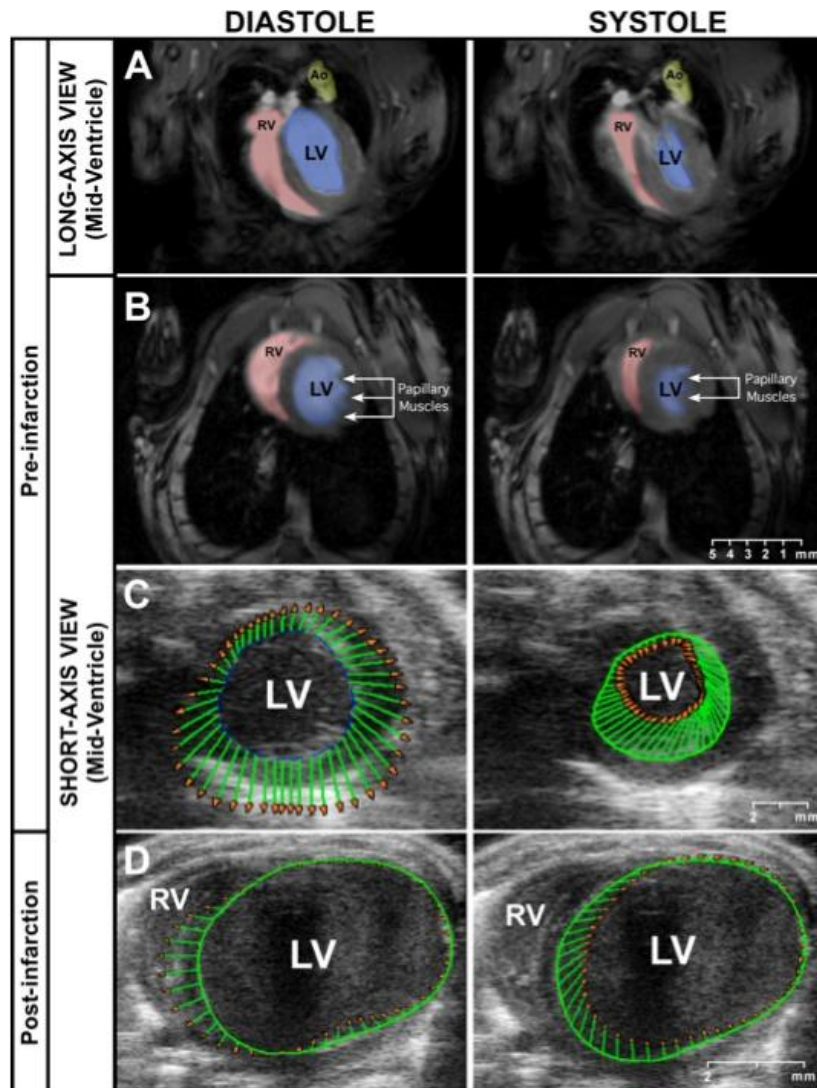


Figure 6.6 Advanced imaging techniques – cine MRI and echocardiography with strain data. Cine-derived gated MR-imaging of the murine cardiac-cycle of a non-infarcted heart using an upright wide-bore 17T NMR. Short (A) and long axis (B) sections are shown at mid-systole and mid-diastole. Short-axis echocardiographic views of a pre (C) and post-infarcted (D) murine heart demonstrate transition from normal (synchronized septal and posterior wall motion at the mid left ventricle) to abnormal (decreased regional septal wall motion) systolic function as depicted by green vector representations of regional strain tensors. RV = right ventricle (red in A & B), LV = left ventricle (blue in A & B), Ao = aorta (yellow in A & B).

7

Radionuclide Approaches To Imaging Stem Cells And Their Biological Effects On The Myocardium

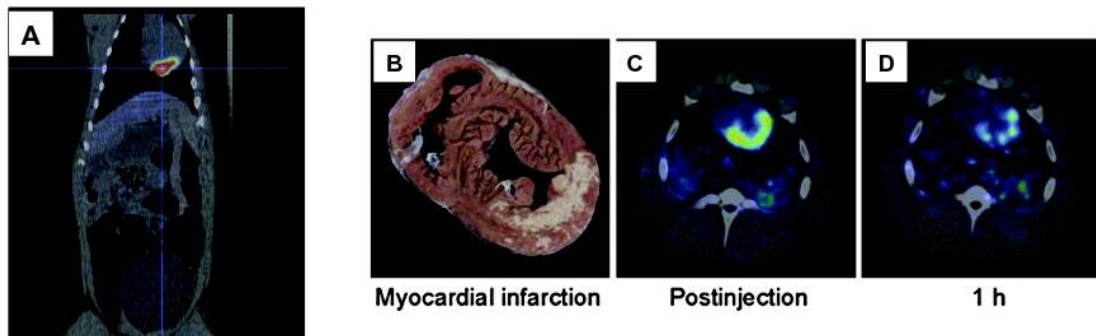


Figure 7.1 (A) Tracer uptake in the inferolateral wall of the LV following injection of ^{18}F -FDG labeled progenitor cells into the left circumflex coronary artery of a normal swine using a balloon-occlusion technique. B-D. Swine underwent LCx occlusion for 90 min followed by injection of ^{18}F -FDG labeled progenitor cells. Triphenyltetrazolium chloride stained myocardial section showing inferolateral necrosis (white) (B), single frame transverse hybrid PET/CT image taken immediately after intracoronary injection of labeled cells showing myocardial activity localized to infarct territory (C), and similar image taken 1 hr after injection showing decrease in activity in infarct zone when compared with post-injection image (D). From Doyle *et al.* *J Nucl Med* 2007;**48**:1711,1713.

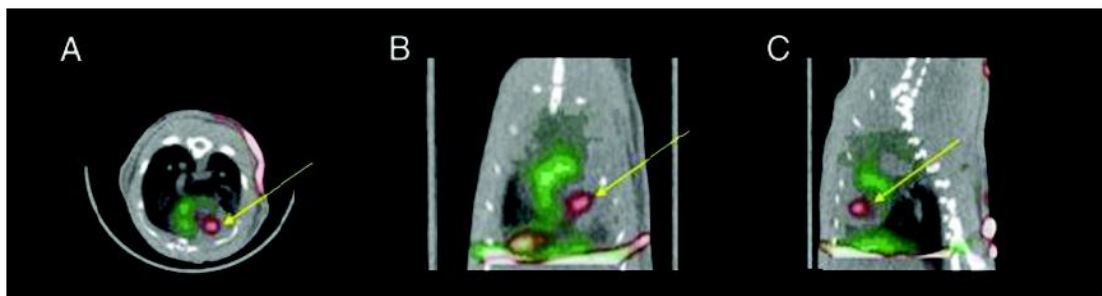
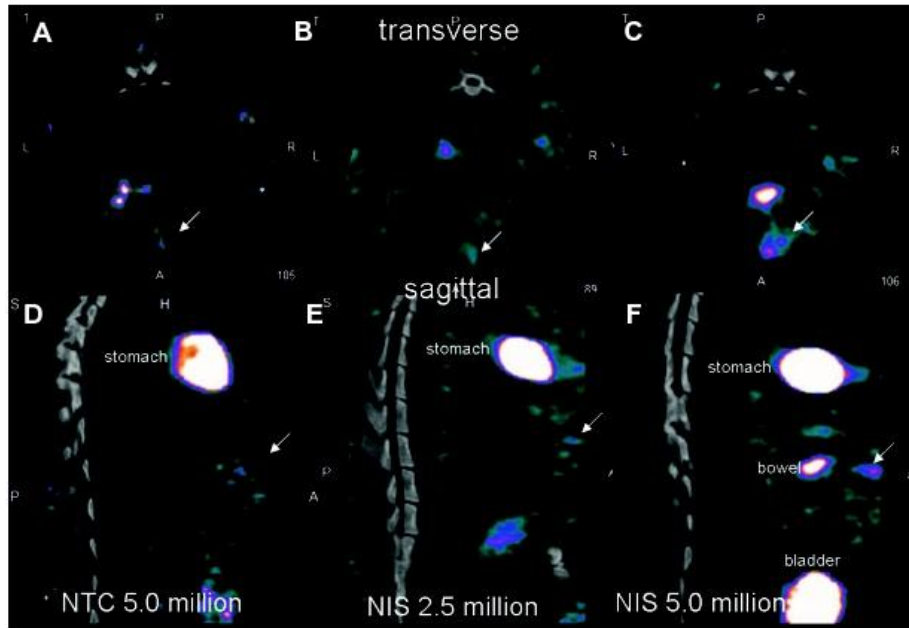


Figure 7.2 Injection of Tc-99m one day after engraftment of hNIS-expressing rat cardiac-derived stem cells into anterior wall following LAD ligation. Thallium-201 was injected to demarcate myocardial perfusion. Tc-99m activity is shown in red and thallium activity in green. The Tc-99m uptake corresponds to the stem cell graft that is localized within the infarct zone delineated by the thallium defect (yellow arrows). From Terrovitis J *J Am Coll Cardiol* 2008;**52**:1655.



	Non-transfected control hMPCs (5×10^6)	hNIS+ hMPCs (2.5×10^6)	hNIS+ hMPCs (5×10^6)
% ID scan	0.1×10^{-3}	1.28×10^{-3}	2.4×10^{-3}
Ex-vivo (counts/g)	109,885	236,341	952,167

Figure 7.3 In vivo SPECT/CT imaging of hNIS mRNA transfected hMPCs implanted with Matrigel into subcutaneous pocket in the abdomen of nude rats. Three days after transplantation rats were injected with Tc-99m and imaged. Minimal signal was detected with non-transfected cells (A,D), weak signal from 2.5×10^6 cells (B,E) and stronger signal from 5×10^6 cells (D,F). The table shows relationship between Tc-99m activity and cell number.

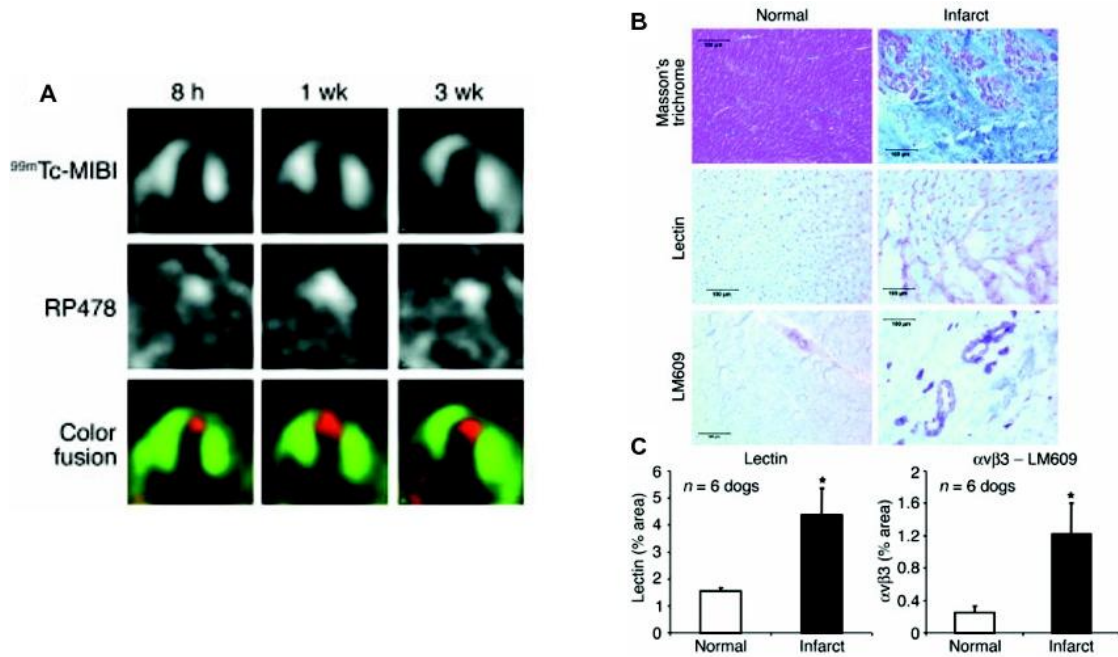


Figure 7.4 **A** Dual isotope SPECT serial imaging of dog with 2 hr LAD occlusion at 8 h, 1 wk, and 3 wk after injection of $^{111}\text{In-RP786}$ (RGD peptomimetic quinolone) targeting $\alpha\text{v}\beta\text{3}$ integrins. The color fusion images show uptake of the $^{111}\text{In-RP748}$ tracer (red color) corresponding to the thallium (green) perfusion defect in the LAD (apical) territory. **B** Immunohistochemical staining of canine infarct. Mason's trichrome staining demonstrates increased vascular density in the central infarct region. Angiogenesis was confirmed by lectin staining and staining for $\alpha\text{v}\beta\text{3}$ (LM609). From Meoli DF, *J. Clin. Invest.* 2004;113:1687,1689.

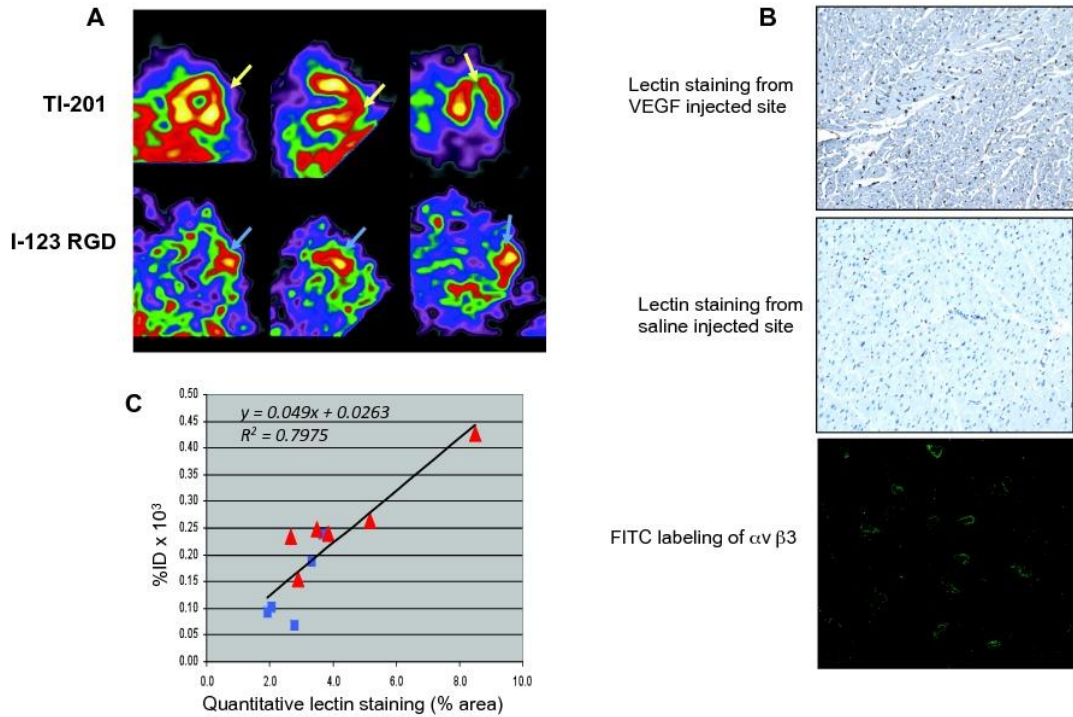


Figure 7.5 **A** Short-axis (SA), vertical long axis (VLA), and horizontal long axis (HLA) SPECT slices from a swine with chronic myocardial hibernation (ameroid constrictor on LCx) treated with phVEGF₁₆₅ delivered into the lateral wall and 20 days later injected with [¹²³I]Gluco-RGD targeting $\alpha v \beta 3$ and thallium-201 for myocardial perfusion. Focal uptake of [¹²³I]Gluco-RGD corresponds to the apical lateral wall perfusion defect on the thallium scan. **B** Immunohistochemical staining of tissue from the lateral wall from animal treated with VEGF and one treated with saline (control) shows evidence for angiogenesis on lectin staining and on fluorescent staining for $\alpha v \beta 3$. **C**. Percent injected dose (ID) per gram of tissue for [¹²³I]Gluco-RGD plotted versus lectin staining as percent area for VEGF injected animals (triangles) and saline injected (squares). From Johnson LL *et al. J Am Coll Cardiol Img* 2008;1:505,507,508.

8

Fluorescence Imaging Of Stem Cells In Vivo: Evolving Technologies And Applications

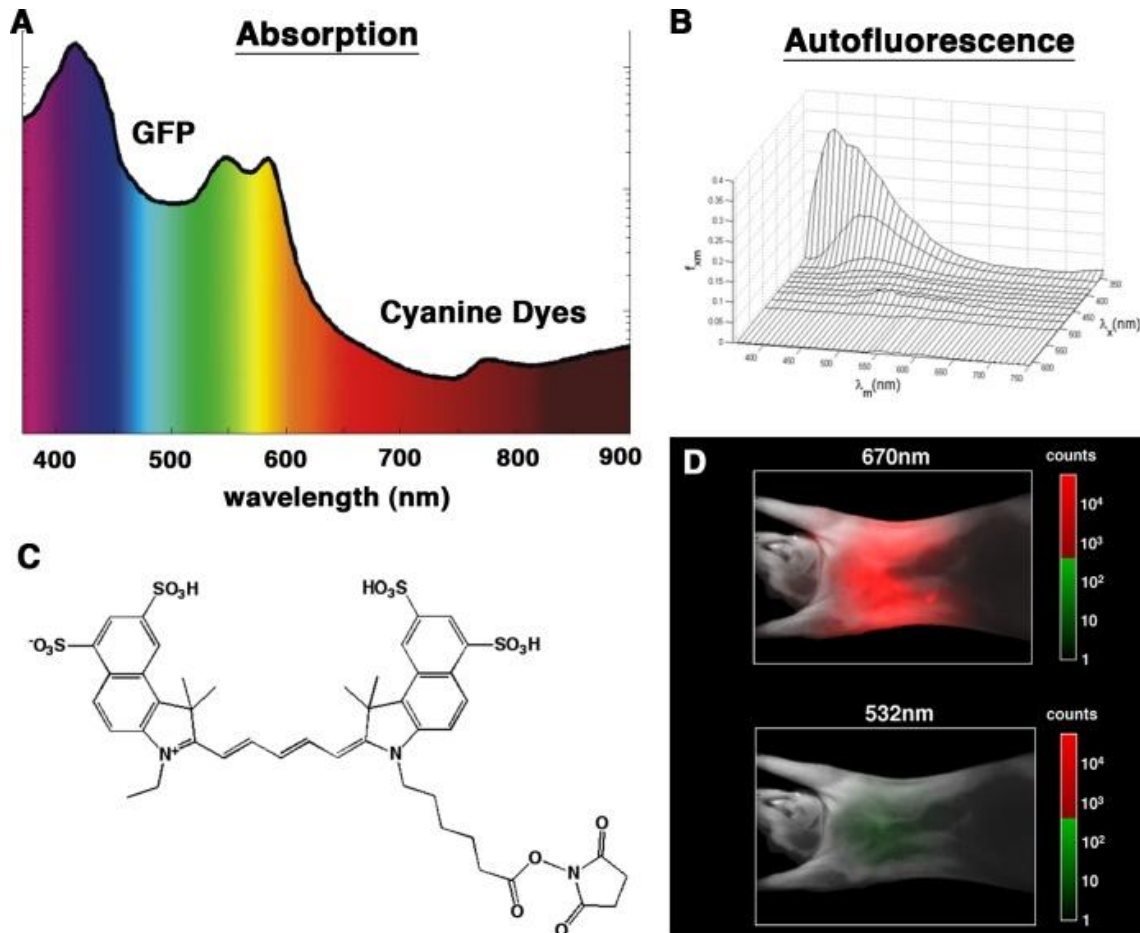


Figure 8.1 **A** The absorption of light by tissue is strongest in the visible spectrum and lowest in the near infrared portion of the spectrum. **B** Tissue autofluorescence is likewise significantly stronger in the visible portion of the spectrum than in the near infrared. **C** Schematic of Cy5.5, a prototypical near infrared cyanine fluorochrome. **D** Illumination of a mouse with light in the visible spectrum and the near infrared (670 nm). Transillumination is significantly higher in the near infrared. Panels A, B, D adapted with permission from (Weissleder and Ntziachristos 2003)

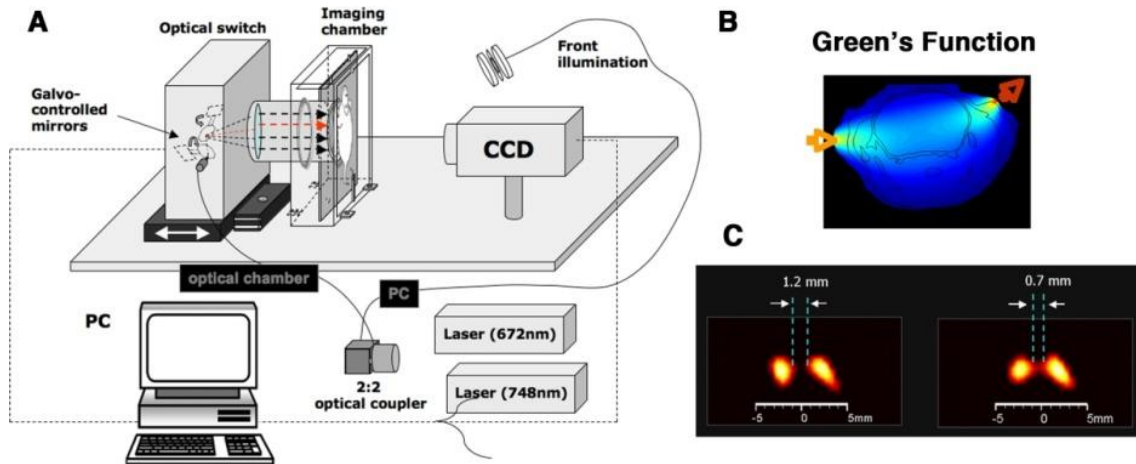
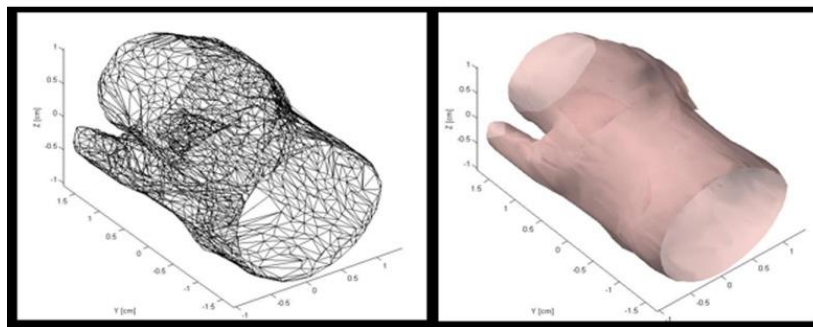


Figure 8.2 **A** Schematic of a second-generation FMT system. The mouse in this system is placed in an imaging chamber containing an optical matching medium. The illumination sources are arranged in a planar slab geometry in front of the mouse. **B** Green's function of light propagation in tissue. The radial width of the function is caused by tissue scattering of light. **C** Two fluorochrome-filled tubes imaged with FMT at variable separation distances. The width of the Green's functions leads to an ill-posed inverse problem and limits the spatial resolution of FMT to the macroscopic range. Panels A, C adapted with permission from.(Graves *et al.* 2003)

Surface Extraction



360° non-contact FMT reconstruction

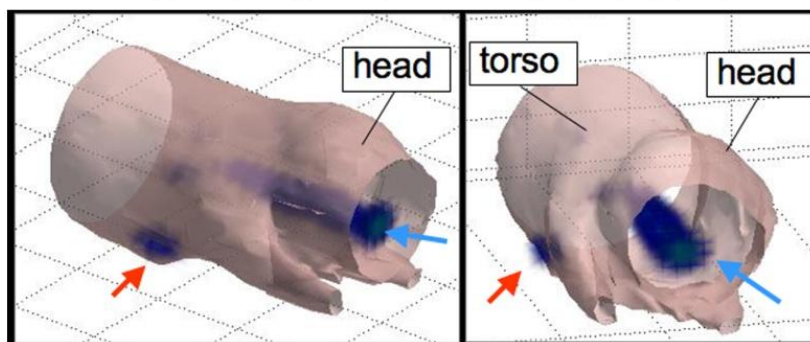


Figure 8.3 Third-generation 360° non-contact FMT systems. The mouse is rotated in the system and illuminated from 360°. Accurate extraction of surface features allows the effects of refraction at the tissue interface to be calculated. The mouse, therefore, does not need to be placed in an optical matching medium. Throughput and simplicity are thus significantly improved. Two fluorescent tubes (arrows) implanted in a mouse are accurately resolved with this system. Adapted with permission from.(N. Deliolanis *et al.* 2007)

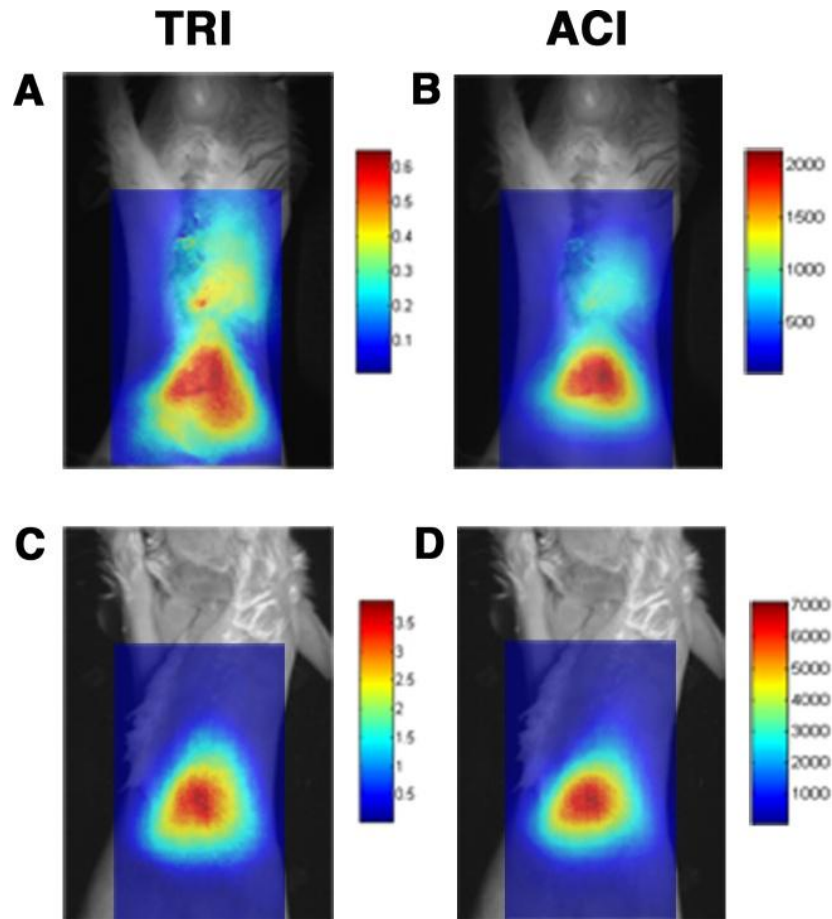


Figure 8.4 Planar transillumination fluorescence images in an infarcted mouse (**A**, **B**) and a sham-operated mouse (**C**, **D**). The mice have been injected with CLIO-Cy5.5, which is taken up by macrophages infiltrating the healing infarct. The fluorescence images have been superimposed on white light images of the mice. Two postprocessing schemes have been used: TRI = transillumination ratio image, ACI = attenuation corrected image. Substantial hepatic uptake of CLIO-Cy5.5 is seen in all mice. Thoracic uptake of the agent is seen only in the infarcted mice. Reproduced with permission from.(Sosnovik *et al.* 2007)

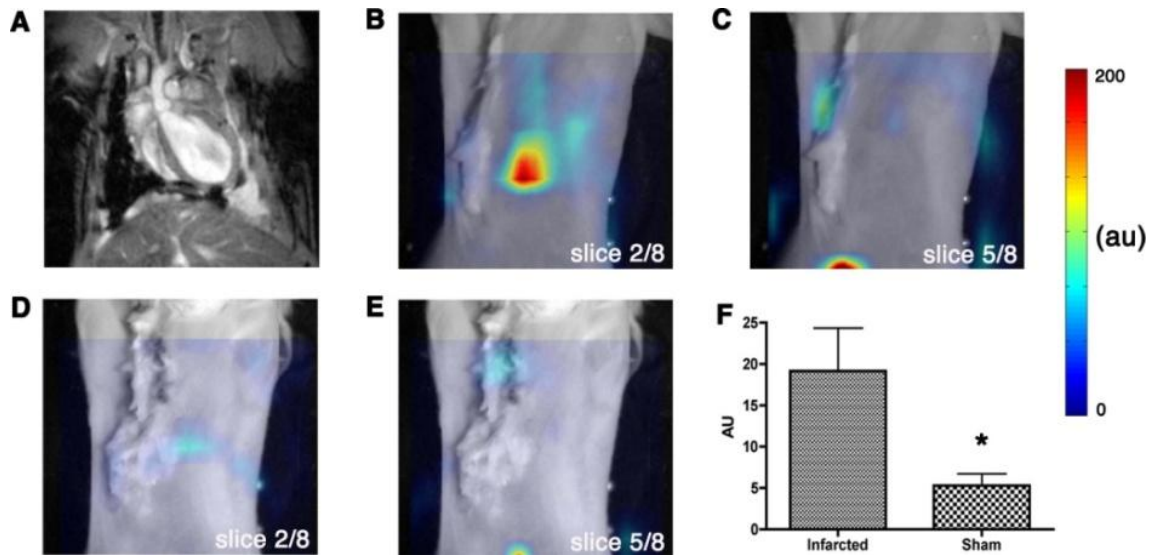


Figure 8.5 FMT of myocardial macrophage infiltration in vivo. Reconstructed coronal slices from the 3D FMT dataset have been superimposed on white light images of the mice. Slices 2-4 in the FMT dataset intersected the heart, while slices 5-8 passed posterior to it. **A** Long axis MRI in an infarcted mouse corresponding to, **B** slice 2 from the fluorescence dataset of that mouse which passed through the heart. **C** Slice 5 from the fluorescence dataset of the infarcted mouse, which passed posterior to the heart. The corresponding slices (**D** = slice 2, **E**= slice 5) of a sham-operated mouse are shown. **F** Depth-resolved fluorescence intensity in the heart was significantly greater (* $p < 0.05$) in the infarcted mice than the sham-operated mice. Reproduced with permission from.(Sosnovik *et al.* 2007)

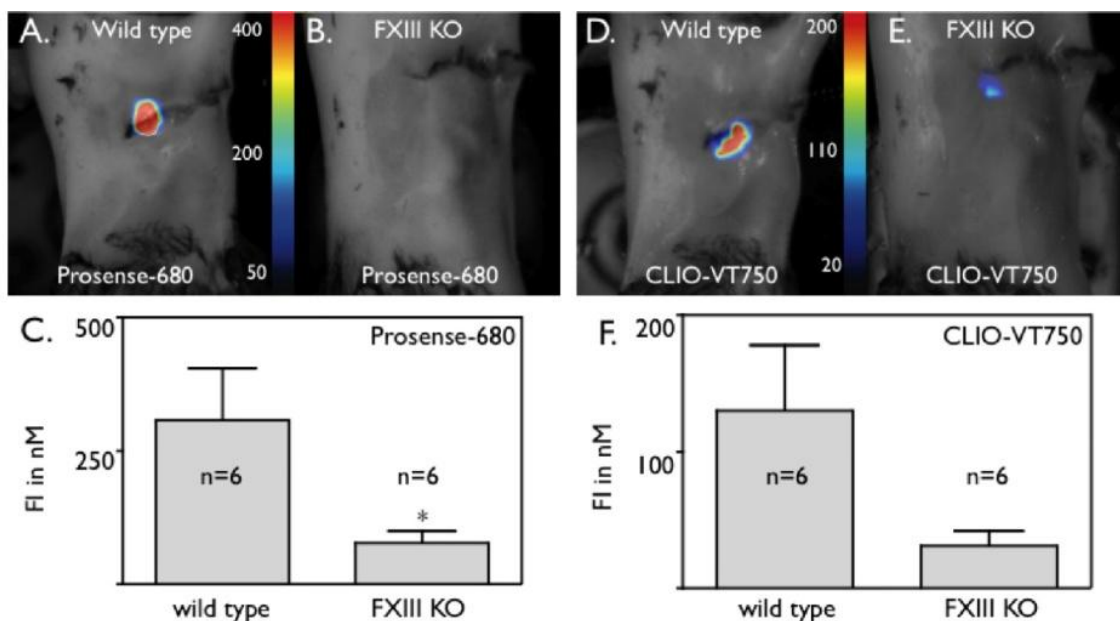


Figure 8.6 Multispectral FMT of the inflammatory response in healing infarcts. Prosense-680 is a protease-activatable Cy5.5 based fluorochrome with an emission wavelength of 680 nm. CLIO-VT750 is a magnetofluorescent nanoparticle with an emission wavelength of 750 nm. Nanoparticle uptake and protease secretion by infiltrating macrophages can be imaged in-vivo with FMT and spectrally resolved. In the example shown, Factor XIII knockout mice with healing infarcts have a significantly lower level of inflammatory activity than wildtype mice. Reproduced with permission from.(Nahrendorf *et al.* 2007)

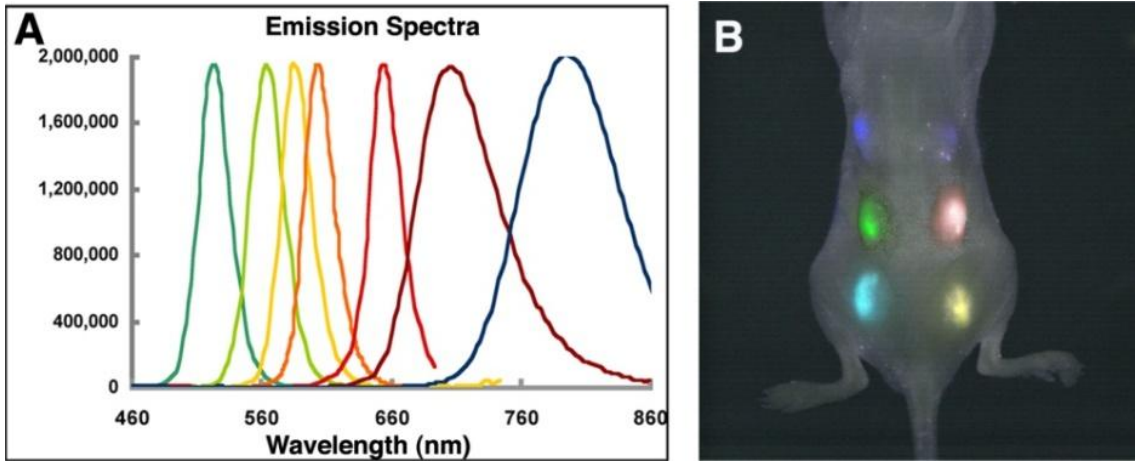


Figure 8.7 **A** Emission spectra of an array of quantum dots. The emission spectra of these quantum dots are narrow, supporting highly multispectral imaging approaches. **B** Fluorescence signals from 6 individual stem cell populations, each labeled with a distinct quantum dot and implanted superficially under the skin of a mouse, can be independently resolved. Reproduced with permission from.(Lin *et al.* 2007)

9

Ultrasound Imaging Basics

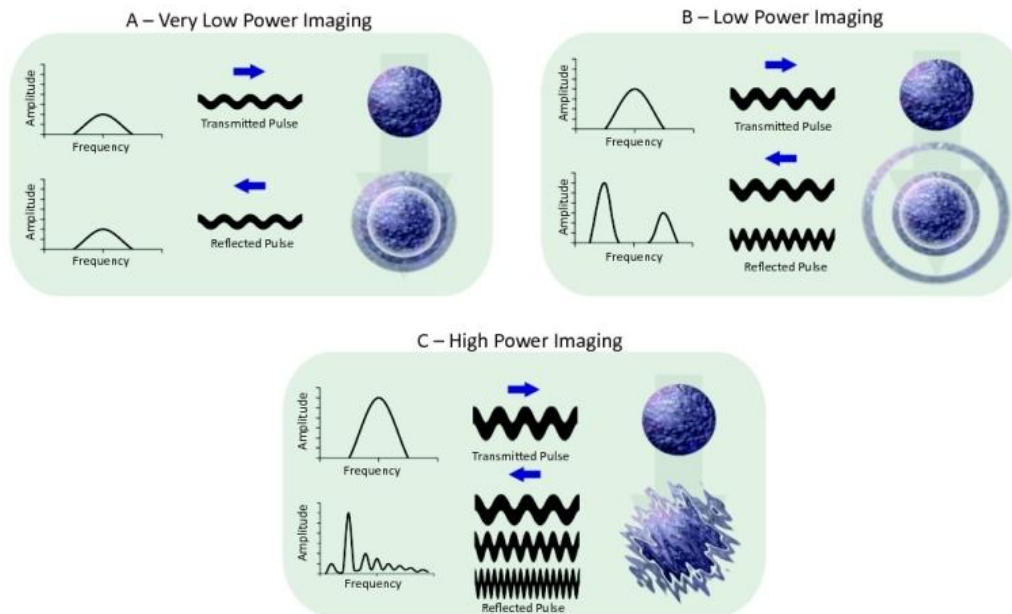


Figure 9.2 Microbubble responses to ultrasound at different acoustic powers or mechanical index (MI). **A.** At a very low MI, the bubbles oscillate, producing a linear acoustic response with the returning spectrum being similar to the transmitted pulse, centered around the fundamental transmit frequency; **B.** At a low to intermediate MI, the bubbles oscillate more vigorously, producing a stronger non-linear acoustic response, with the returning spectrum consisting of fundamental and harmonic components (multiples of the fundamental transmit frequency); **C.** At a high MI, microbubbles are destroyed producing a very strong non-linear signal consisting of multiple frequencies, including fundamental, subharmonic and varying harmonic frequencies.

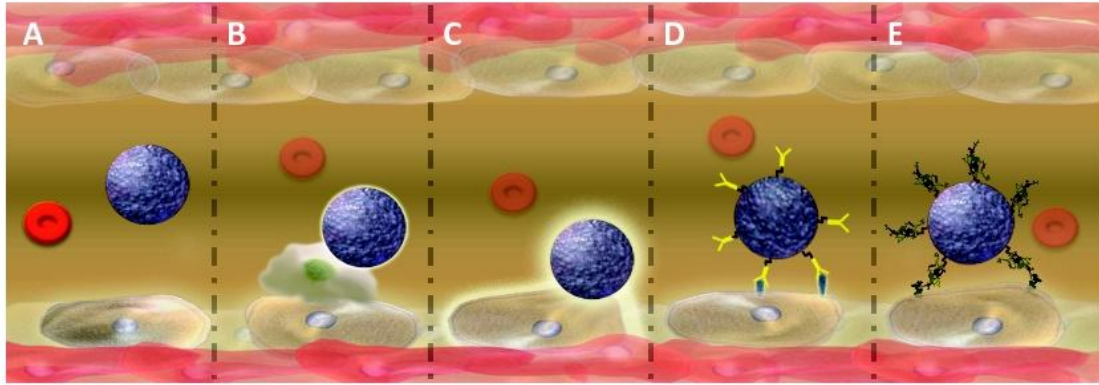


Figure 9.3 Methods of targeting microbubbles. **A.** Non-targeted freely circulating microbubble; **B.** Microbubble targeted by shell composition – in this case a leukocyte-avid bubble for the imaging of inflammation; **C.** Microbubble targeted by shell surface properties, in this case charge related binding; **D.** Microbubble targeted by attachment of a monoclonal antibody against a specific target; **E.** Microbubble targeted by attachment of a targeting peptide or small molecule, against a specific intravascular target.

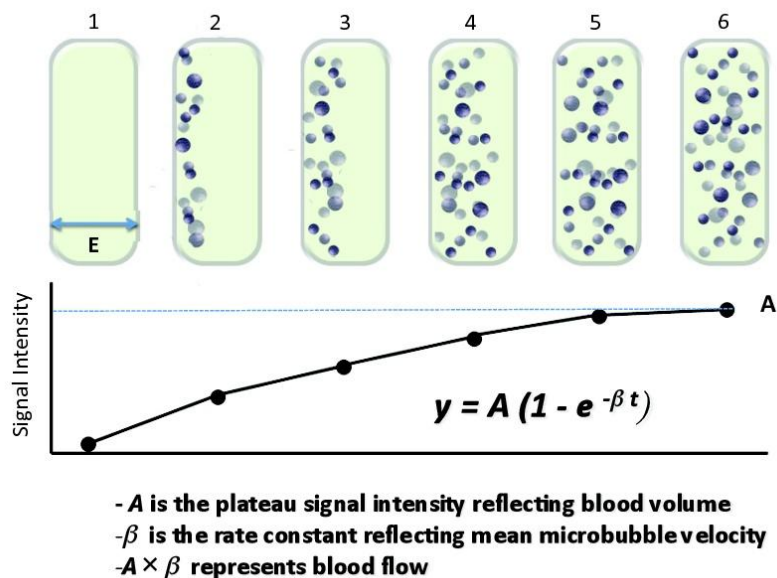


Figure 9.4 Schematic diagram of method to quantify blood flow using contrast-enhanced ultrasound and perfusion microbubbles. During a continuous infusion of microbubbles, after bubble destruction by high power ultrasound there is progressive filling of the vasculature within the ultrasound-beam thickness (elevation - E) by microbubbles, at increasing time intervals (panels 1 to 6). When the signal intensity from microbubbles is plotted against time, the points can be fitted to the 1-exponential equation: $y = A(1 - e^{-\beta t})$, where A is the plateau signal intensity reflecting blood volume, β is the rate constant reflecting microbubble or blood flow velocity, and the product of the two, $A \times \beta$ represents blood flow (19).

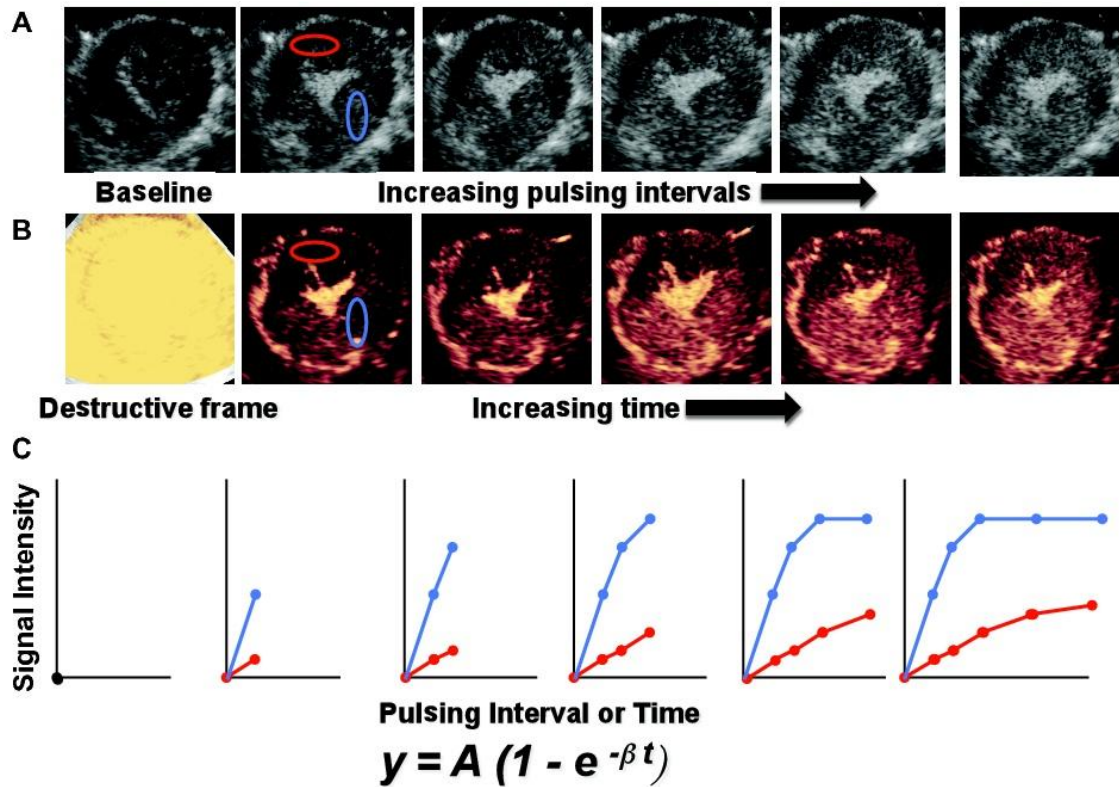


Figure 9.5 Examples of myocardial contrast echocardiographic perfusion images in a canine model of coronary artery stenosis, induced by an occluder on the left anterior descending (LAD) coronary artery. **A** High power contrast second harmonic imaging at increasing pulsing intervals, showing a perfusion defect (dark area) in the anterior myocardium. **B** Low power pulse inversion Doppler contrast imaging at increasing time points after high power destructive frames (leftmost panel), showing a perfusion defect (dark area) in the anterior myocardium. **C** Progressive plots of background-subtracted signal intensity versus pulsing intervals or time in the ischemic anterior myocardium (LAD territory – red region-of-interest) and normal posterolateral myocardium (left circumflex territory– blue region-of-interest), showing the reduced rate of replenishment (reflected by β) and the lower plateau signal intensity (A) in the ischemic LAD bed (red), as compared to the normal left circumflex bed (blue).

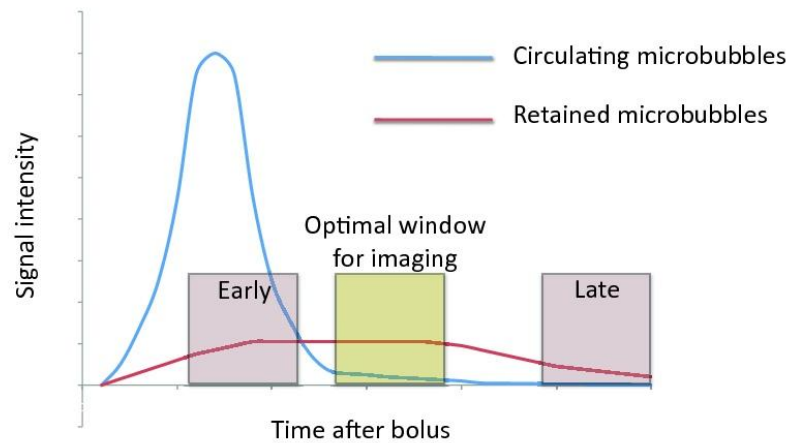


Figure 9.6 Representative graph of the acoustic signal from targeted and freely circulating microbubbles after an intravenous bolus. While the number and signal from circulating bubbles rises rapidly, the number and signal from retained targeted microbubbles rises slower as they accumulate within target tissues, and plateaus longer. If ultrasound imaging is performed too early, the signal from circulating bubbles is very high, and does not allow easy detection of adhered targeted microbubbles. If ultrasound imaging is performed too late the number of retained microbubbles are very low. The ideal time for imaging is during the plateau phase of targeted bubble retention, at a time when circulating bubbles have markedly decreased.

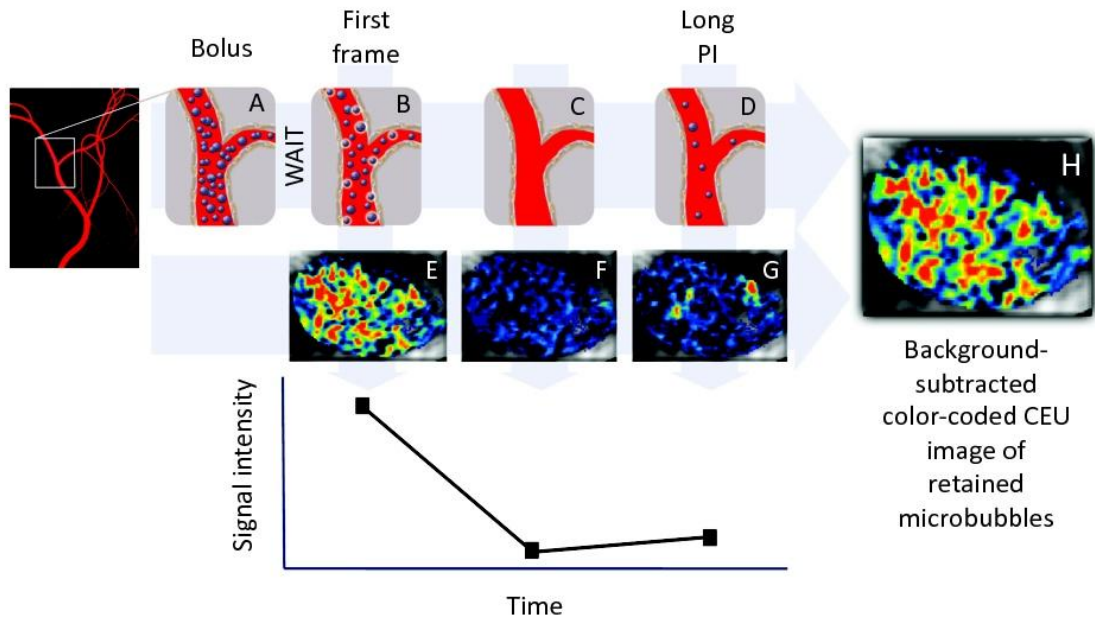


Figure 9.7 Acquisition protocol for targeted imaging using contrast-enhanced ultrasound molecular imaging in a rodent hindlimb. After an intravenous bolus of site-targeted microbubbles, their concentration in the circulation is very high (panel **A**). Ultrasound imaging is suspended, to allow the microbubbles to continually circulate and bind to their target receptors. After waiting a period of time (5-10 minutes), ultrasound imaging of the hindlimb muscle is commenced, where the first frame(s) of ultrasound detects mostly retained microbubbles with a small amount of signal related to circulating microbubbles (panels **B** and **E**). Further high power ultrasound imaging results in destruction of all bubbles within the muscle (panels **C** and **F**), and the signal within tissue drops. Subsequent imaging at long pulsing intervals detects any remaining freely circulating microbubbles (panels **D** and **G**). When the signal from freely circulating microbubbles is subtracted from the initial frame(s) (panel **E** minus panel **G**), this yields the signal from retained targeted microbubbles alone (panel **H**). The graph below demonstrates the signal intensity measurements at various time points after intravenous site-targeted microbubble bolus.

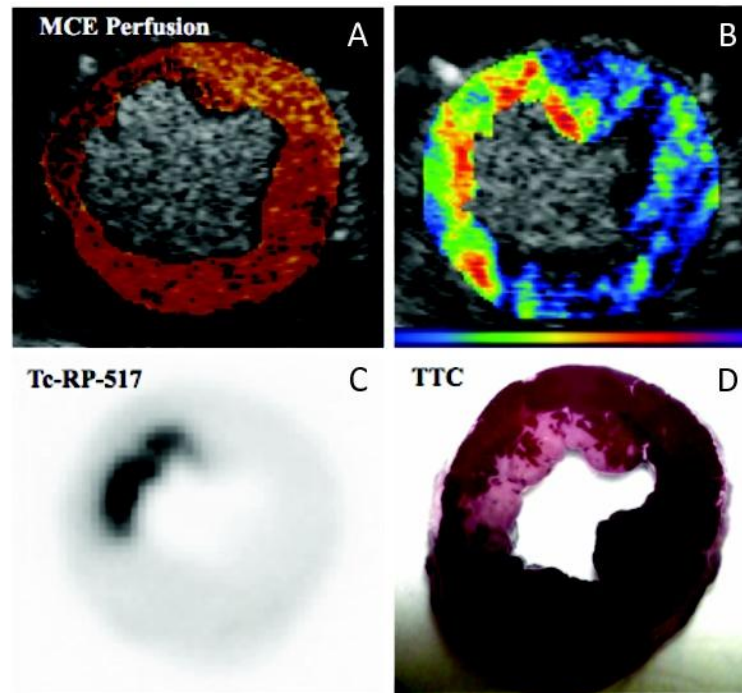


Figure 9.8 Myocardial contrast echocardiographic (MCE) molecular imaging of reperfusion injury/inflammation using leukocyte-targeted microbubbles in a canine model of ischemia/infarction-reperfusion. **A** Background-subtracted color-coded MCE short-axis image of myocardial perfusion showing a perfusion defect (dark region) in the anterior myocardium, where infarction has occurred. **B** Background-subtracted color-coded short-axis image of signal from retained leukocyte-targeted microbubbles demonstrating the area of inflammation within the myocardium, indicating area of reperfusion injury. This area of reperfusion injury corresponds to **C** ^{99m}Tc -RP517-labeled leukocyte accumulation by gamma camera imaging, and **D** infarct zone by post-mortem 2,3,5-Triphenyltetrazolium chloride (TTC) staining. (Reproduced with permission from Christiansen et al (30)).

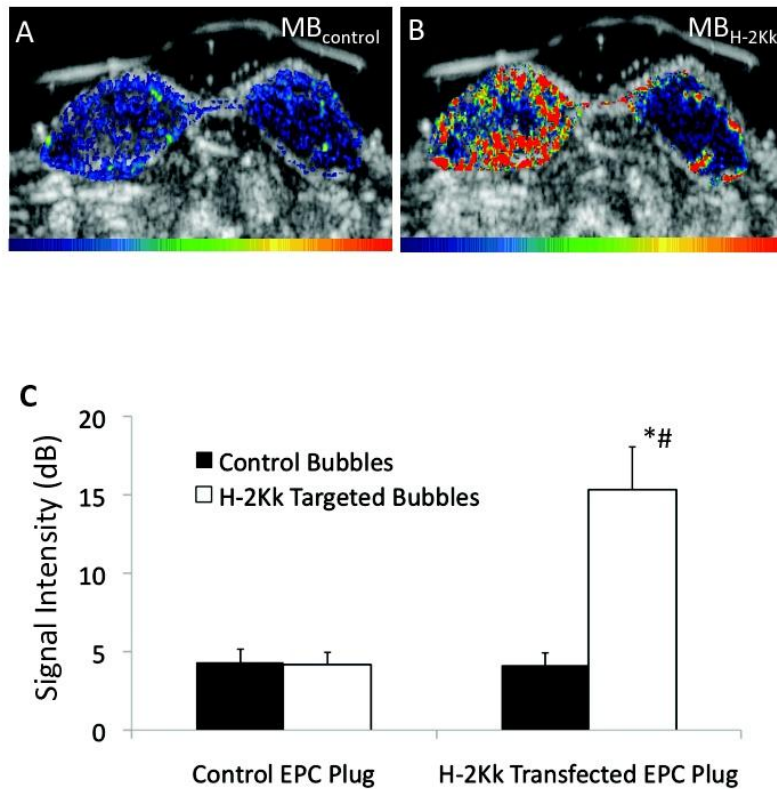


Figure 9.9 Molecular imaging of endothelial progenitor cell (EPC) engraftment. Background-subtracted color-coded contrast ultrasound images of EPC engraftment in supplemented matrigel plugs (left plug – EPCs transfected to express the cell surface marker H-2Kk; right plug – control EPC supplemented), after intravenous bolus injection of **A** control microbubbles - MB_{control}, and **B** H-2Kk-targeted bubbles – MB_{H-2Kk}. While there was minimal signal after control MB, there was a strong contrast ultrasound signal from H-2Kk-targeted bubbles in the left plug (H-2Kk-EPC supplemented) with only minimal signal in the control EPC supplemented right plug. **C** EPC-targeted contrast ultrasound imaging data. While there was minimal signal for control bubbles in both control EPC- and H-2Kk-EPC supplemented plugs (black bars), the signal intensity was greater for H-2Kk-targeted bubbles (white bars) in the H-2Kk-EPC supplemented, as compared to the control EPC supplemented right plug. * $p < 0.001$ versus MB_{control}, # $p < 0.005$ versus control mock-transfected EPC plug. (Reproduced with permission from Kuliszewski *et al* (54)).

12

Radionuclide Cell Labeling Methods

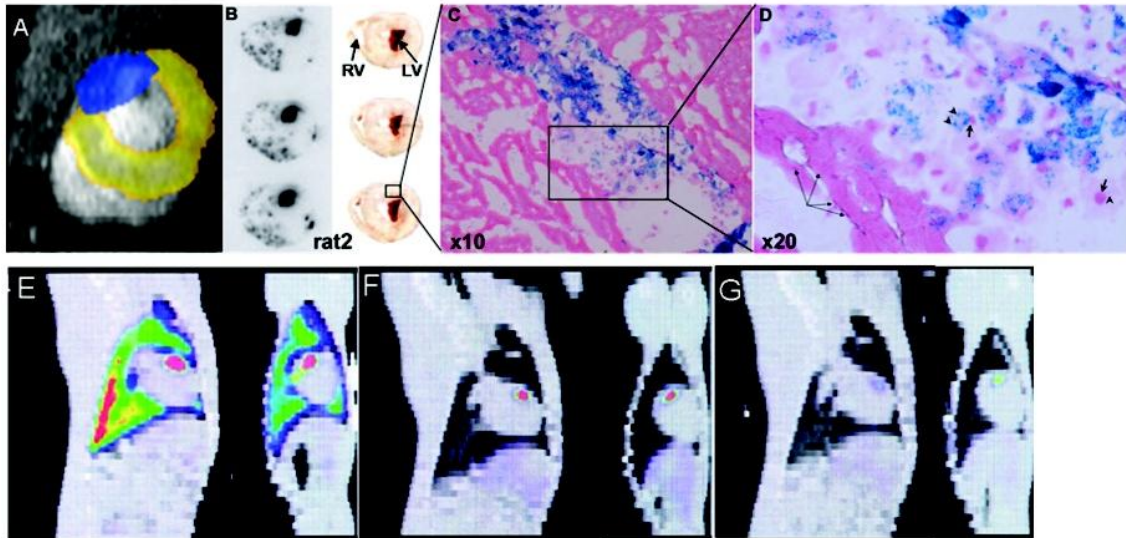


Figure 12.1 A Dual isotope SPECT images and coregistration with MR images: In-111 labeled stem cells were implanted in the infarcted rat heart; a dual energy window detects simultaneously [Tc-99m]sestamibi (pseudo-colored in yellow) and [In-111] (blue) signals; the SPECT images were coregistered on MRI image (grey). B Autoradiographs of heart sections obtained after transplantation of In-111 and Feridex double-labeled stem cells in the infarcted myocardium of a rat. C – D Prussian blue staining of iron for localization of the stem cells (reprinted from (12) with permission). E – G Homing of [In-111] labeled BMSCs to the infarcted heart (in dogs) after intravenous injection at day 1 (E), day 2 (F) and day 7 (G) by SPECT imaging. For each panel, sagittal (left) and coronal (right) view of fused SPECT (color) and CT (grey) images are shown. Initial retention of cells in the lung is indicated by strong In-111 signal in the lung (reprinted from (12) with permission).

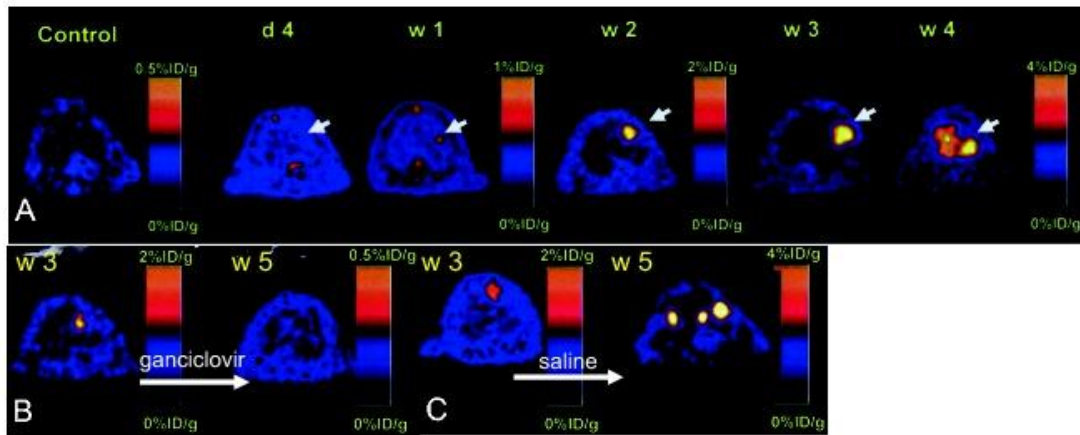


Figure 12.3 A In vivo tracking of stem cell survival and proliferation using the reporter gene method. Ten million (10^7) murine embryonic stem cells transfected with a truncated version of HSV1-tk were injected into the myocardium of a non-infarcted nude rat; PET was performed at day 4 and weeks 1, 2, 3, and 4. Approximately 1 mCi [$F-18$]9-[3-fluoro-1-hydroxy-2-(propoxymethyl)]guanine was injected intravenously for visualization of HSV1-tk-expressing cells. Positive signal was observed at 1 week after injection of cells, but control animals showed background activities only. Quantification of imaging signals showed a drastic increase of thymidine kinase activity from week 2 to week 4, corresponding to proliferation of embryonic stem cells into teratoma. **B – C** After administration of a pharmacological dose of ganciclovir (50 mg/kg twice daily for 2 weeks), [$F-18$] PET signal disappeared suggesting elimination of sr39tk expressing cells whereas [$F-18$] signal became stronger in saline treated rats. (reprinted from (53) with permission)

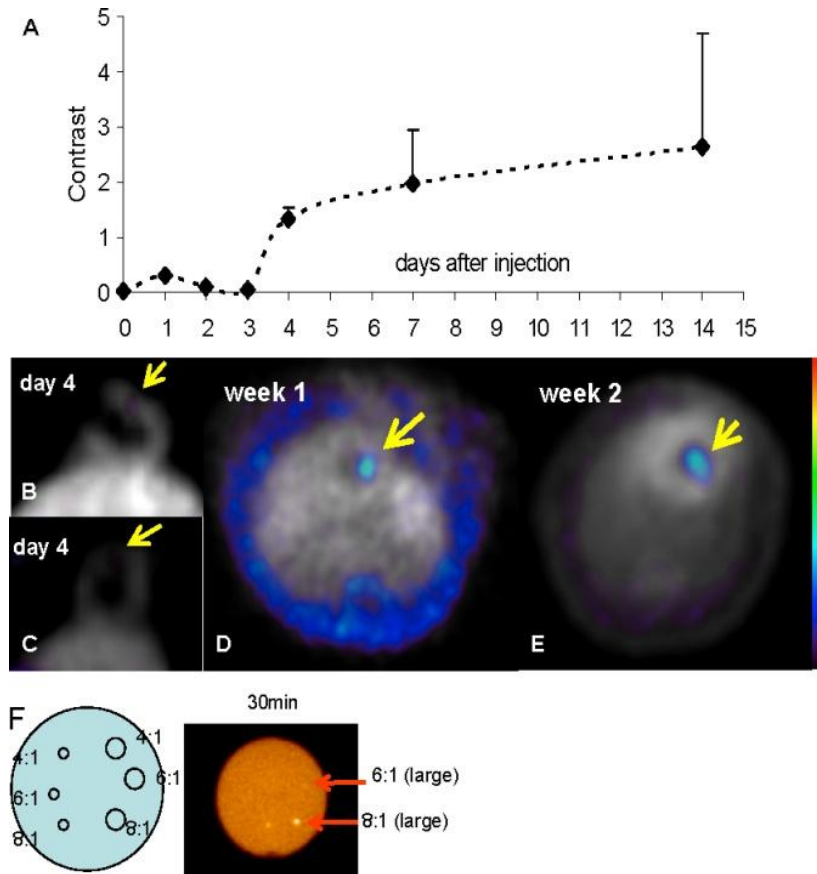


Figure 12.4 A Contrast of [F-18] images acquired at day 0-14 was estimated by $Contrast = \frac{meanVOIh - meanVOIref}{meanVOIref}$, where $VOIh$ is the volume of interest encompassing the hot spot

while $VOIref$ was placed on reference (septum) region of the myocardial wall. Images were shown for day 4 (B – C), week 1 (D) and week 2 (E) after injection of 5 million embryonic stem cells stably-expressing sr39tk. [N-13]ammonia image (shown in gray scale) provides the anatomical reference of the heart (myocardial wall in particular) to facilitate the localization of the F-18 signals (color scale). (F) A phantom study was performed to aid the estimation of the in vivo uptake ratio. Three small capillaries (ID = 0.75 mm) and 3 large capillaries (ID =1.75 mm) containing the activity concentration of 4:1, 6:1 and 8:1 respectively were scanned for 30 min. The contrast value of 1.3 was obtained from the large capillary with 8:1 concentration activity; the contrast matched that on day-4 [F-18]PET images acquired with the same scanning time, suggesting that activity ratio between the hot spot and surrounding myocardium could be $\geq 8:1$ (reprinted from (72) with permission).

13

Principles Of Bioluminescence Imaging And Its Application *In Vivo*

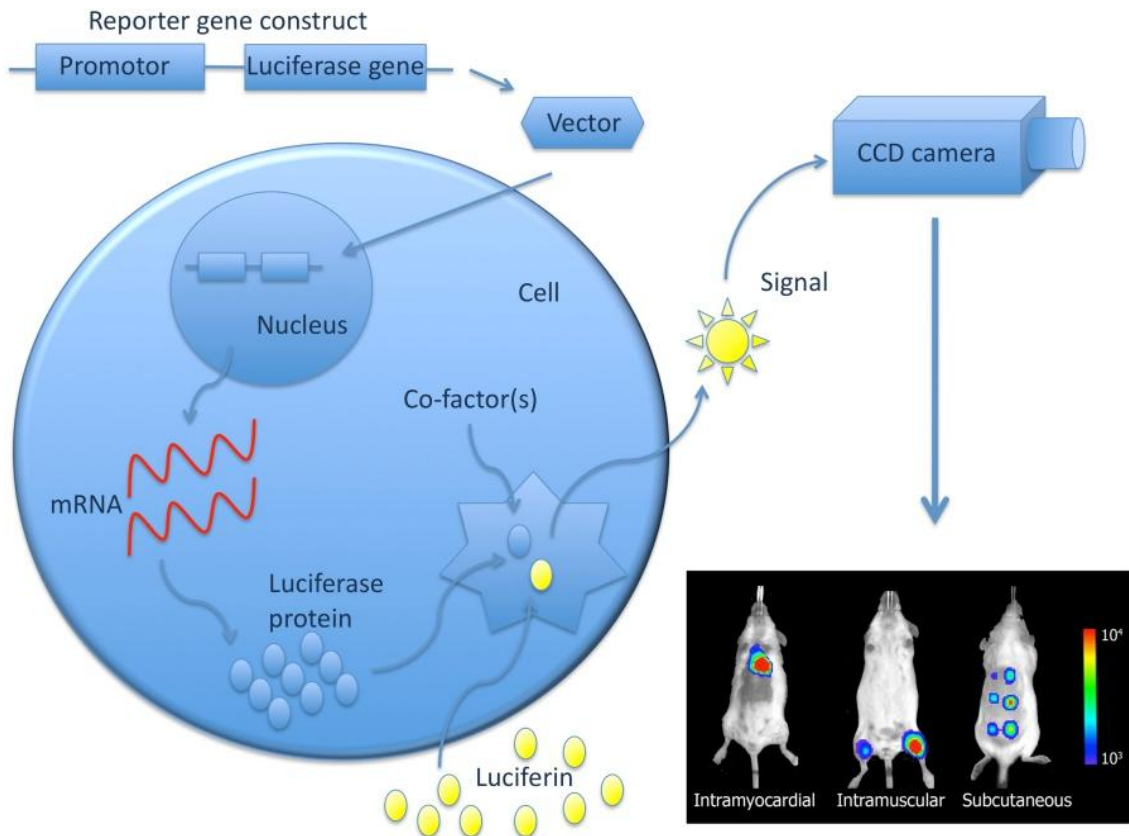


Figure 13.1 The concept of reporter gene imaging. A viral or non-viral vector delivers the reporter gene construct into the cell nucleus, to be transcribed to mRNA. Subsequent translation of the mRNA results in luciferase proteins. The luciferase proteins generate a signal once they interact with the reporter probe and the necessary co-factors. This signal is detectable by a charge-coupled device (CCD) camera. Stem cells containing the reporter gene can be tracked *in vivo* using a variety of cell transplantation models: intramyocardially, intramuscularly, or subcutaneously.

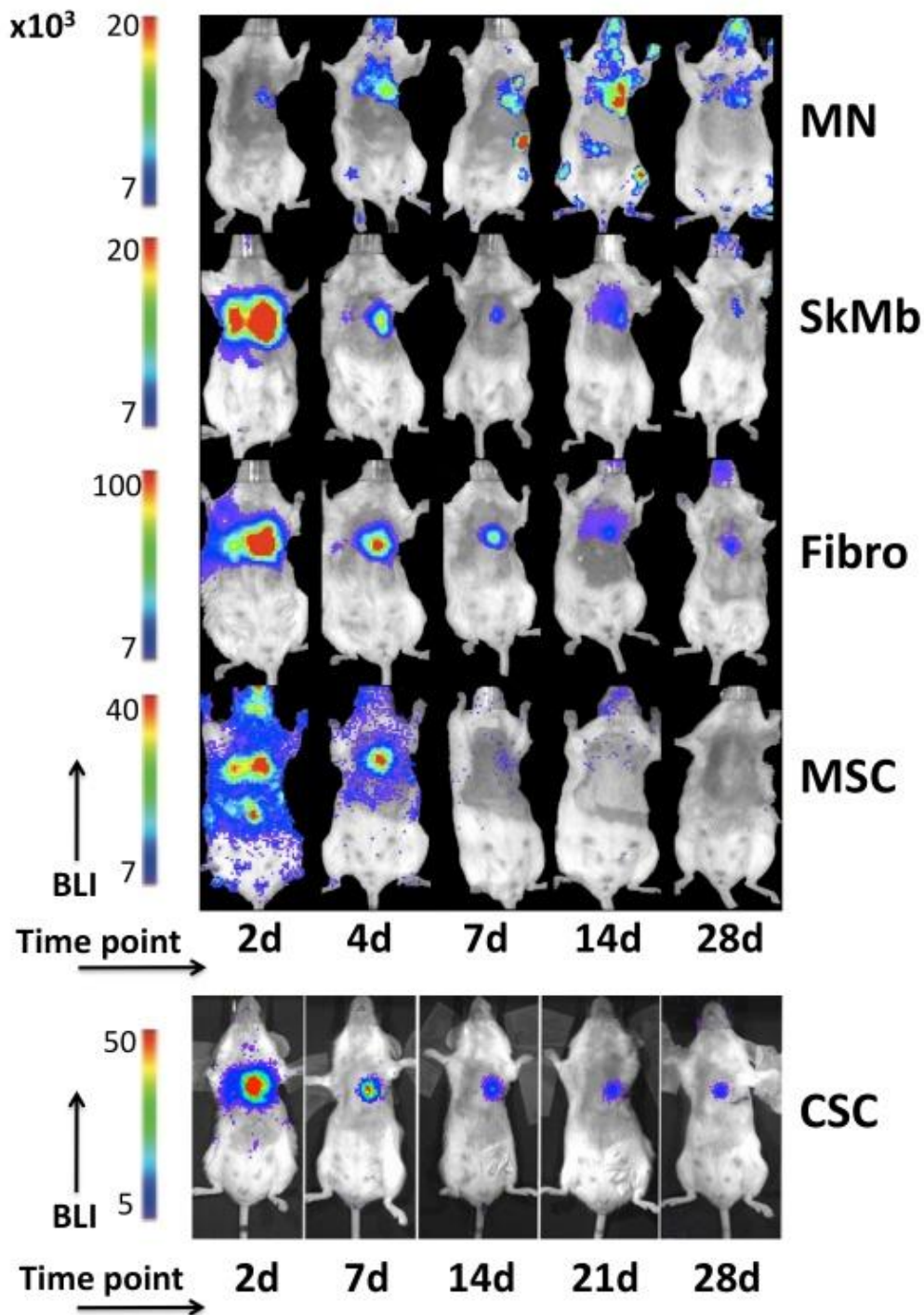


Figure 13.2 Tracking stem cell proliferation and survival *in vivo* using bioluminescence imaging. *In vivo* longitudinal survival BLI of mononuclear stem cells (MN), skeletal myoblasts (SkMb), Fibroblasts (Fibro), mesenchymal stem cells (MSC) and cardiac stem cells (CSC) transplanted from L2G transgenic mice to FVB mice. Scale bars present signal intensity in photons/s/cm²/sr. Images adapted from 1. Bogt, van der K. *et al.* [28] with permission from Wolters Kluwer, and 2. Li, Z. *et al.* [29] with permission from Elsevier.

14

Quantum Dot Labeling Methods

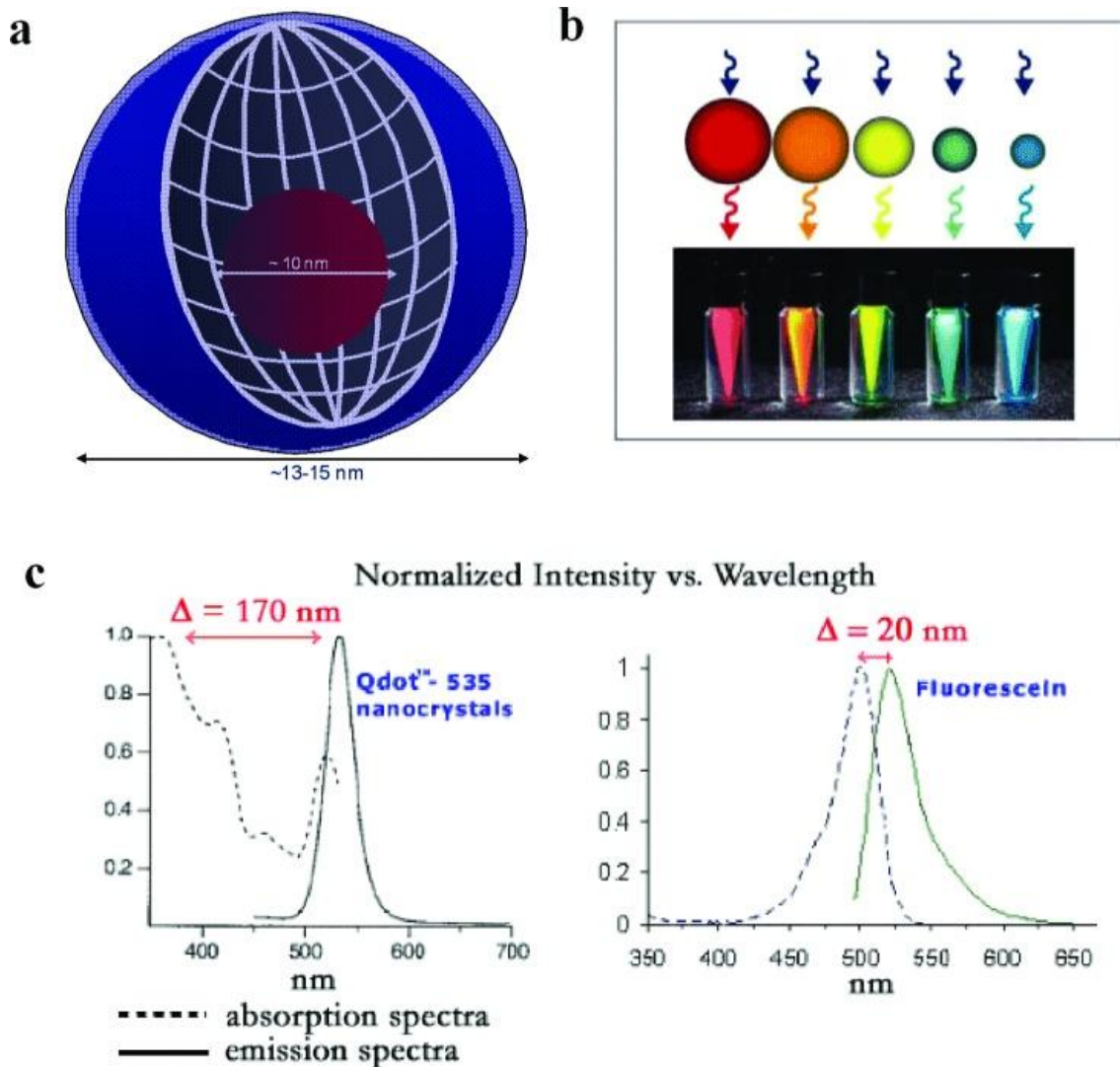


Figure 14.1 **A** Quantum dot (QD) nanoparticles are composed of a core semiconductor material (ie CdSe) and coated with a different semiconductor shell (ie ZnS). The particle is made biocompatible by virtue of an inert passivating coating. **B** QD particles emit unique wavelengths of fluorescent light upon excitation with a common incident light source (in this case, a handheld UV lamp), depending on the size of the QD core, a property known as tunability. **C** The Stokes' shift, or large difference between the wavelength of excitation and emission light, makes QD detection highly sensitive, and superior to conventional fluorescent dyes. [adapted with permission from Quantum dot corporation]

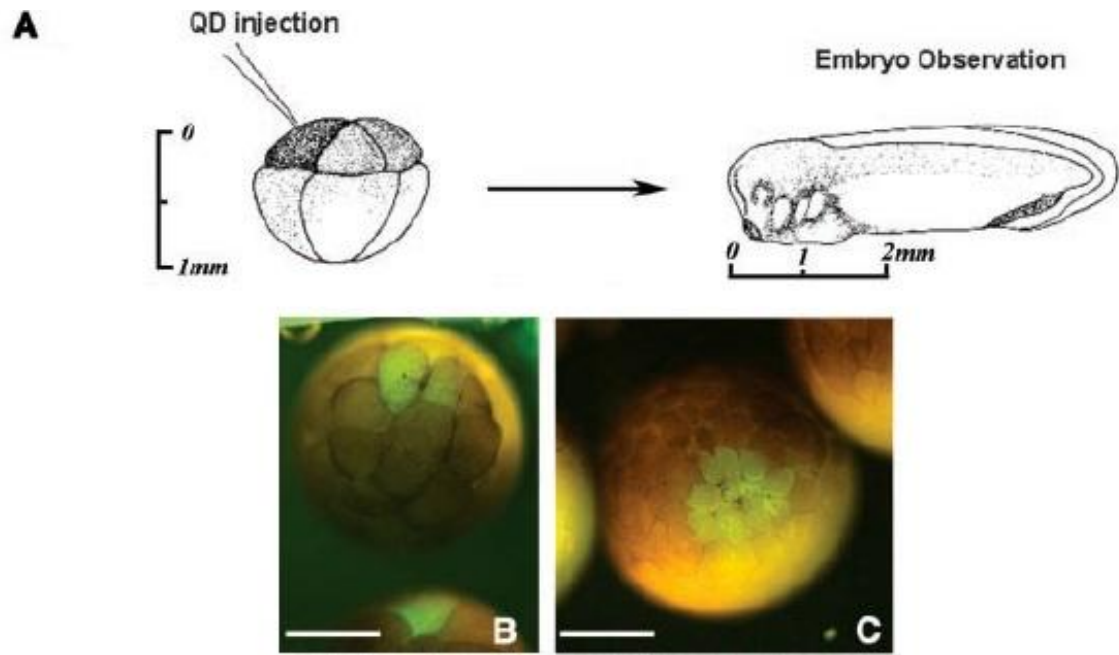


Figure 14.2 Xenopus lineage tracing **A** QDs were microinjected into a single blastomere of the Xenopus embryo. The embryos were then cultured until they reached various stages of development, at which point they were imaged. **B** One cell out of an eight-cell embryo is labeled with QDs. **C** Same embryo 1 hour after injection, depicting labeled daughter cells. Reprinted with permission from (Dubertret *et al.* 2002).

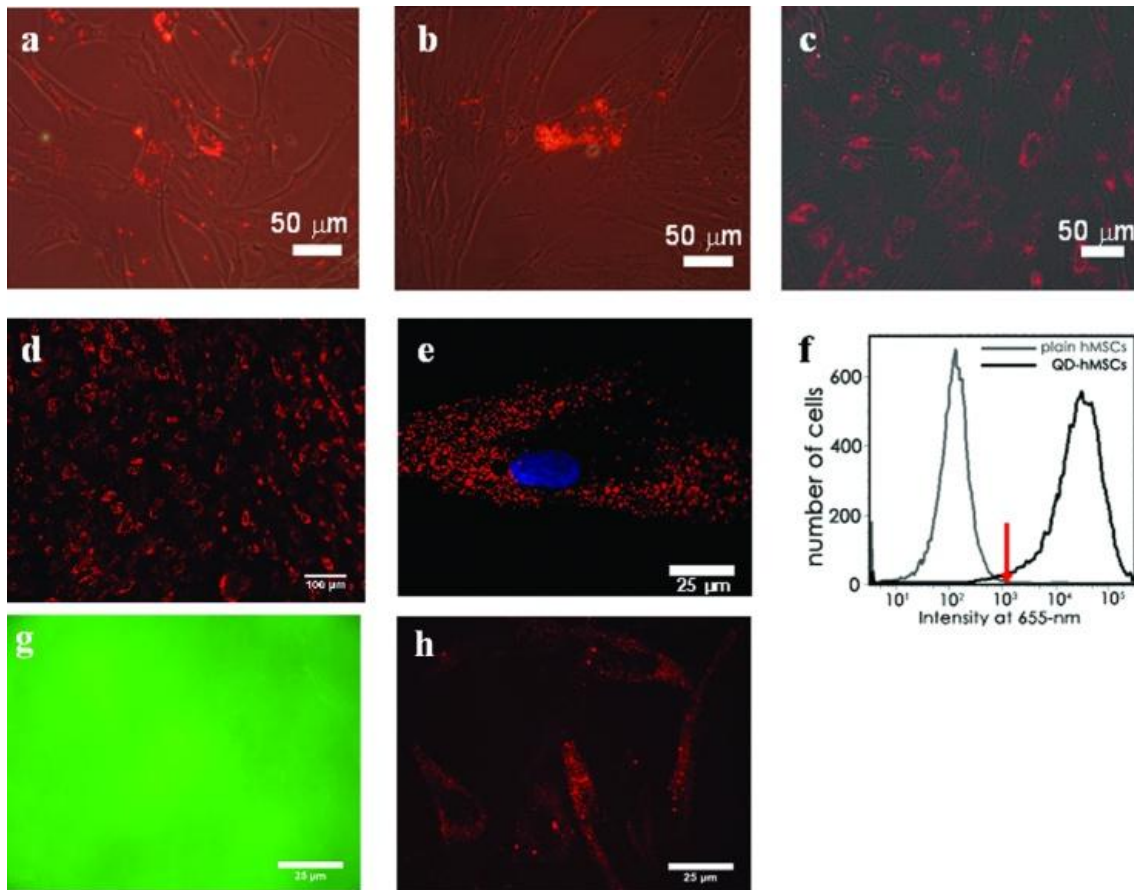


Figure 14.3 Quantum dots (QDs) were loaded into human mesenchymal stem cells (hMSCs) by three approaches. Panels a-c show images of QD fluorescence (655nm, red) with phase contrast overlays. **A** Electroporation of cells in media containing carboxylated-655nm QDs resulted in perinuclear aggregation of the dots, non-uniform labeling and cell death. **B** Use of thereceptor- mediated-based Qtracker kit (Quantum Dot, Inc) again resulted in non-uniform cellular loading with perinuclear aggregation, but with better cell survival than with electroporation. **C** In contrast, passively incubating hMSCs in naked QD medium resulted in nearly 100% loading with a pattern that extends to the cell borders. **D** The field in (C) is imaged for QD fluorescence without the phase overlay to demonstrate homogeneity and brightness. The intracellular QD cluster distribution is diffusely cytoplasmic (**D,E**) and largely excludes the nucleus (blue, Hoechst 33342 dye). **F** QD loading efficiency was analyzed using flow cytometry. The threshold for plain hMSCs (gray line) was set such that the intensity range encompassed at least 98% of the control cells (red arrow indicates upper bound of control range). QD-positive status was designated for all cells in the QD-hMSC sample having intensities above the range set for the control group. In four experiments, QD-positive cells (black line) were found in 96% of over 17,000 viable cells. Panels **C-F** adapted with permission from (Rosen *et al.* 2007). **G** GFP-transfected and **H**) QD-labeled hMSCs were each seeded onto a 100 μ m-thick extracellular matrix patch (porcine bladder) and imaged for their respective emissions. Only intracellular QD-fluorescence **H** is detectable above autofluorescence, whereas GFP-labeled cells cannot be seen above autofluorescence in (**G**).

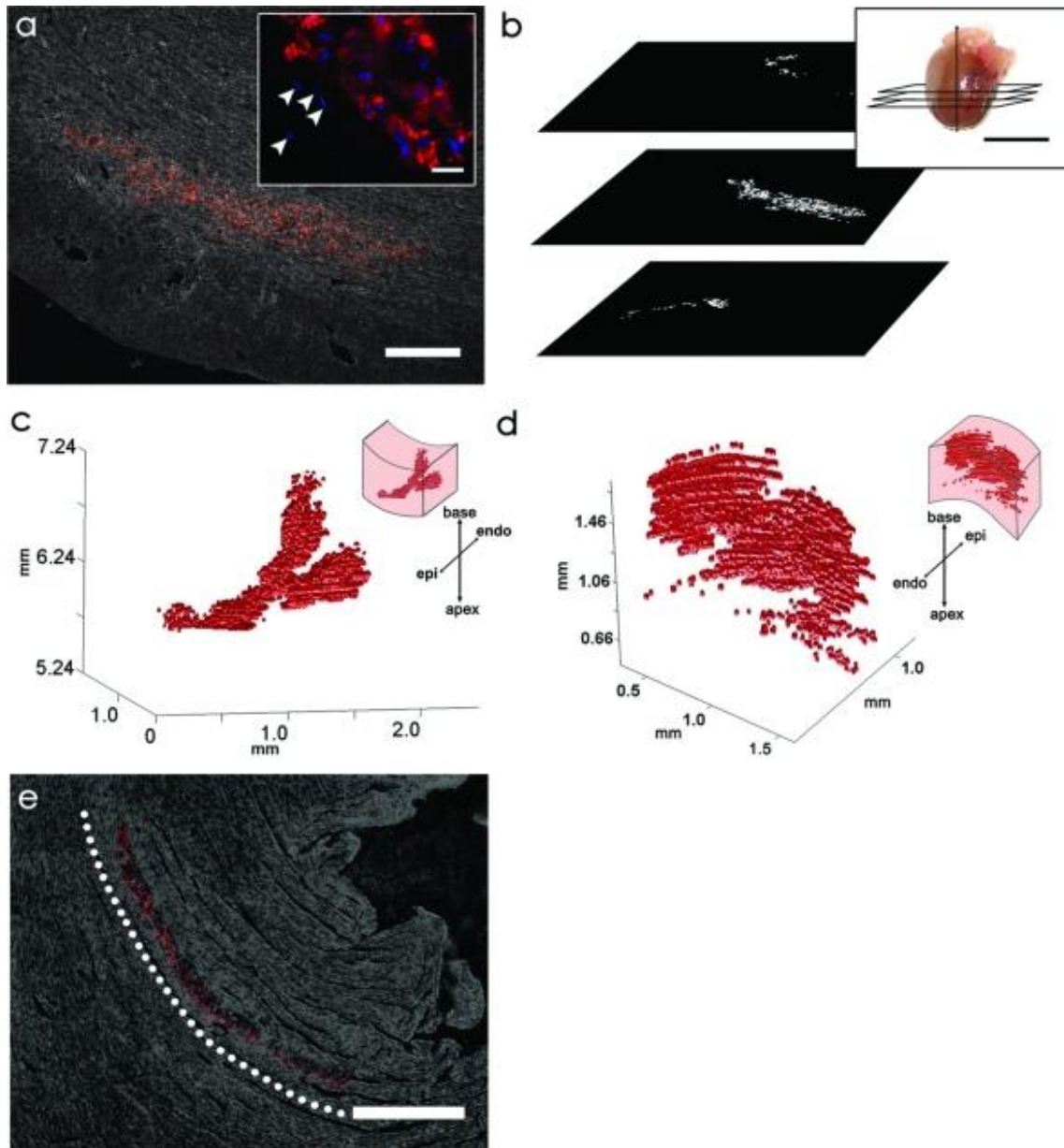


Figure 14.4 QDs can be used to identify single cells (hMSCs) after injection into the rat heart and further used to reconstruct the three-dimensional (3D) distribution of all delivered cells. Rat hearts were injected with QD-hMSCs and subsequently excised and processed for tissue analysis. Tissue sections were imaged for QD fluorescence emission (655 nm) with phase overlay. QD-hMSCs can be visualized at **A** low power and (inset) high power (Hoechst 33342 dye used to stain nuclei blue). In **A**, inset, endogenous nuclei can be seen adjacent to the delivered cells in the mid myocardium (arrows). **B** Binary masks (where white pixels depict QD-positive zones in the image) for all QD-positive sections were used to generate the 3D reconstruction of delivered cells in the tissue. **C** QD-hMSC reconstruction in an animal that was terminated 1 hour after injection. **D**: Reconstruction from an animal euthanized 1 day after injection with orientation noted in inset. **E** One day after injection into the heart, the pattern of QD-hMSCs is well organized and appears to mimic the endogenous myocardial orientation (dotted white line highlights myofibril alignment). Adapted with permission from (Rosen *et al.* 2007).

15

Magnetic Resonance Imaging Cell Labeling Methods

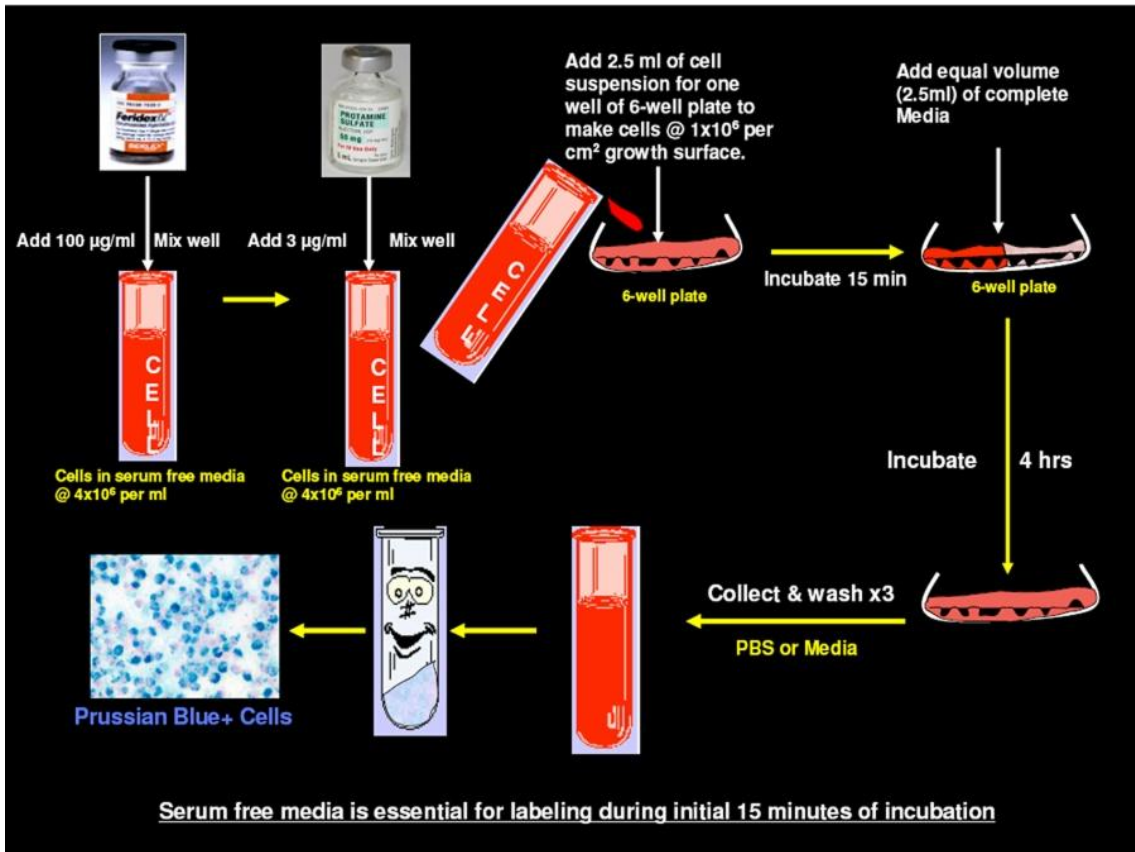


Figure 15.1 Schematic representation of the superparamagnetic iron oxide labeling procedure for suspension cells.

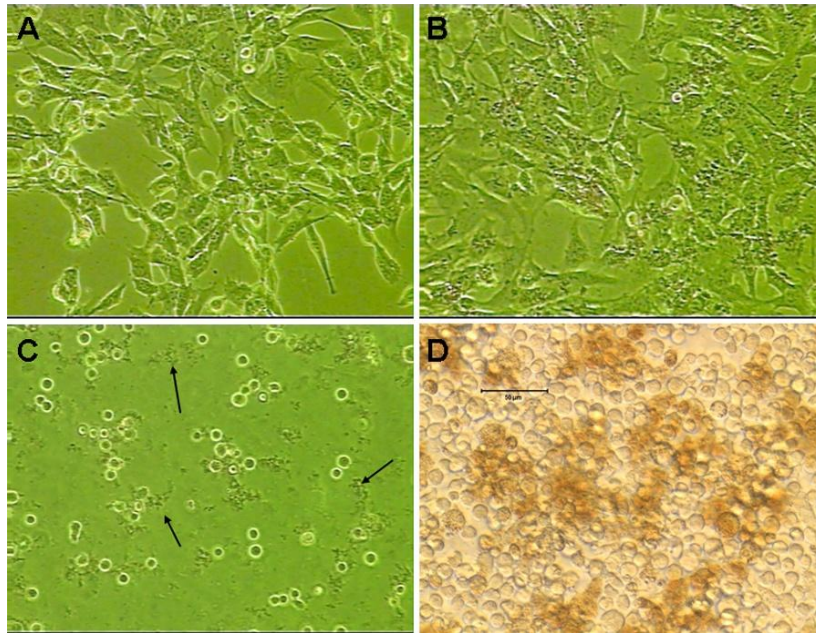


Figure 15.2: Importance of cell number during incubation. **A,B** Neural stem cells labeling (adherent cells) using ferumoxides and protamine sulfate. Ferumoxides was added to the cells (after getting rid of old media and washing with serum free media) at $100\mu\text{g/ml}$ and mixed well with the serum free media and then freshly prepared (making of stock solution of $1\text{mg}/1\text{ml}$ of distilled water) protamine sulfate was added to the media at $3\mu\text{g/ml}$. The images are obtained with an inverted microscope at $40\times$ magnification. Note there is no definite complexes seen five minutes after addition of ferumoxides and protamine sulfate (**A**) but small complexes (black dots) are seen attached to the cells at 4 hours (**B**). However, no large complexes are seen as all of the complexes distributed equally and get attached to the cells and there are no free complexes to make bigger chunks. (**C, D**) Hematopoietic stem cells labeling (suspension cells) using ferumoxides and protamine sulfate. Ferumoxides was added to the cells (after getting rid of old media and washing with serum free media) at $100\mu\text{g/ml}$ and mixed well with the serum free media and then freshly prepared (making of stock solution of $1\text{mg}/1\text{ml}$ of distilled water) protamine sulfate was added to the media at $3\mu\text{g/ml}$. Then the cells were plated in 6-well plate at a cell density of 2×10^5 and 1×10^6 cells per cm^2 of growth surface. Note the formation of chunk of complexes (arrows on **C**) within 5 minutes after incubation. There are no large complexes seen even after 4 hours of incubation (**D**) when the density of cells is maintained at 1×10^6 per cm^2 .

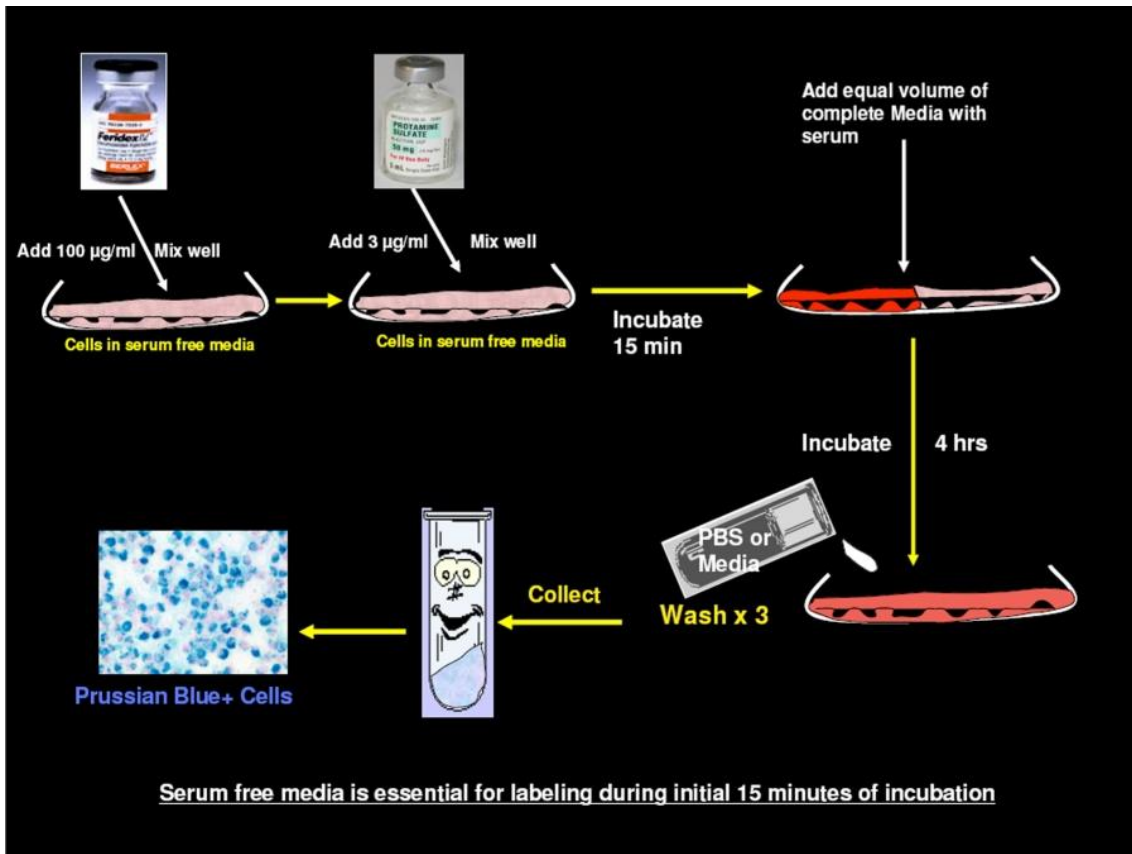


Figure 15.3 Schematic representation of superparamagnetic iron oxide labeling procedure for adherent cells.

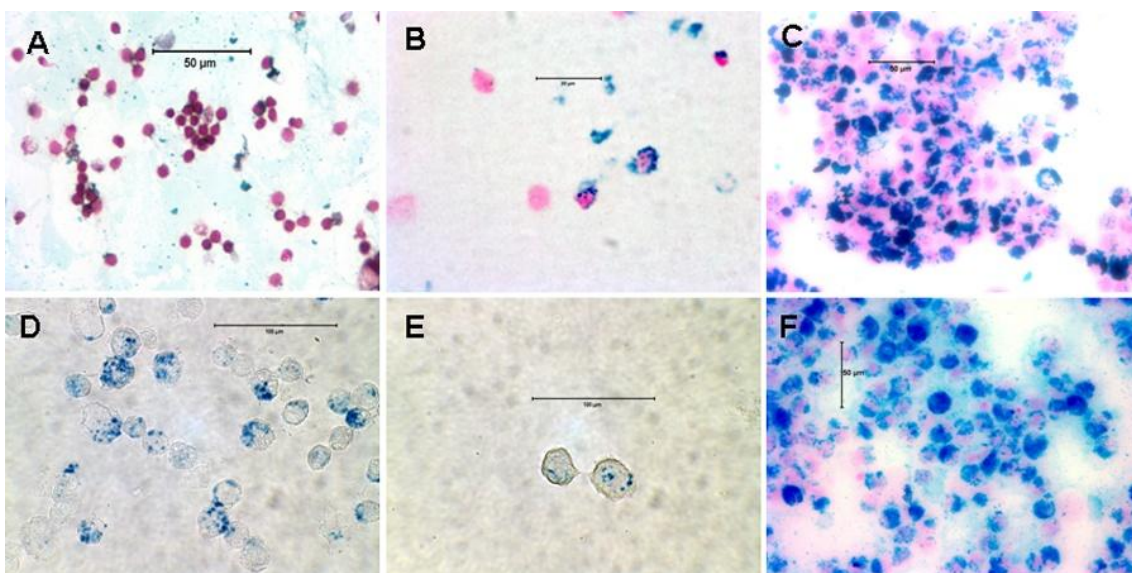


Figure 15.4 Representative images of different types of magnetically labeled cells. **A** Cytotoxic T-cells; DAB enhanced Prussian blue staining, bar represents 50µm. **B** Hematopoietic stem cells (CD34+/AC133+); Prussian blue staining, bar represents 20µm. **C** U251 human glioma cells; Prussian blue staining, bar represents 50µm. **D** Neural stem cells (C17.2); Prussian blue staining, bar represents 100µm. **E** Umbilical cord derived mesenchymal stem cells; Prussian blue staining, bar represents 100µm. **F** Umbilical cord blood derived immature dendritic cells; Prussian blue staining, bar represents 50µm.

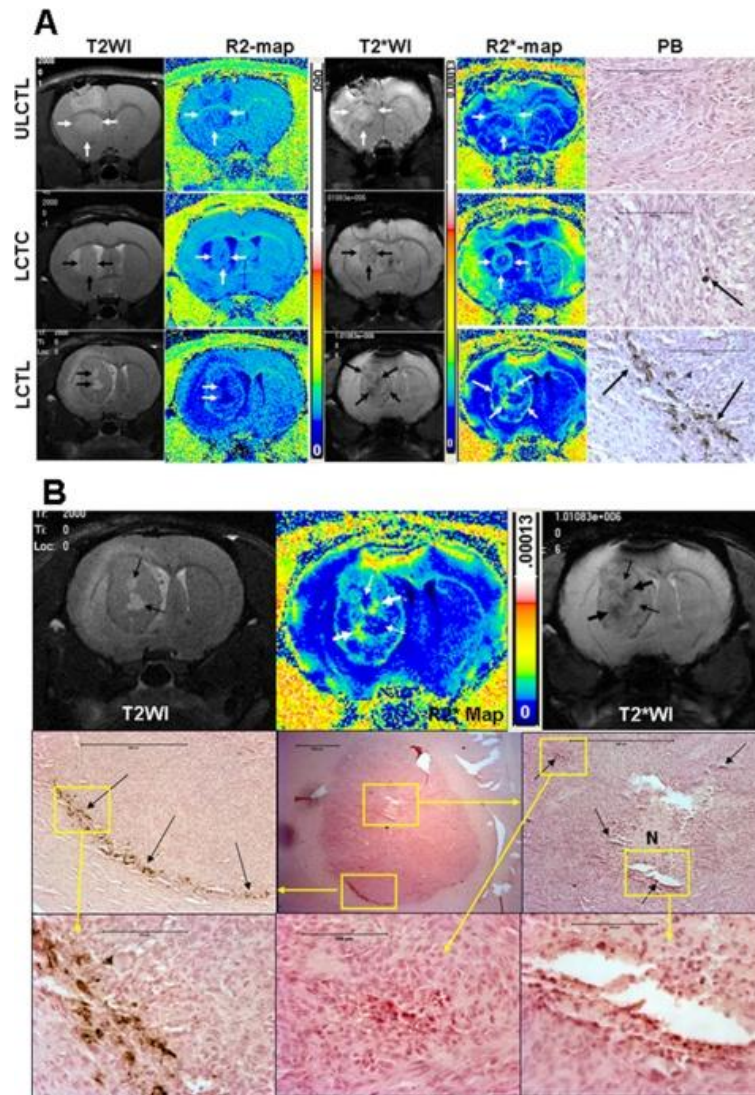


Figure 15.5 MRI and Prussian blue positive cells in tumors. **A** T2-weighted and T2*-weighted images and their corresponding R2 and R2* maps and DAB enhanced Prussian blue staining from representative animals that received unlabeled CTL (ULCTL, upper row), labeled control T-cells (LCTC, middle row) and CTL (LCTL, lower row). Both T2W and T2*W images show well established tumors in the brain, however, low signal intensity areas were only seen in tumors that received LCTC and LCTL. Corresponding R2* maps show high signal intensity areas. Animals that received LCTL show high signal intensity areas both at the peripheral and central part of the tumors (arrows). Corresponding DAB enhanced Prussian blues staining show multiple Prussian blue positive cells in tumors that received LCTL (arrows). There are a few Prussian blue positive cells seen in tumor that received LCTC (arrow). No definite Prussian blue positive cells were seen in tumor that received ULCTL. Areas of necrosis can easily be identified by comparing T2WI and R2 maps (thick arrows) in tumor that received LCTL (lower row). Bars on the images measure 100 μ m. **B** Detailed histological analysis of the tumor that received LCTL. Bars on the images measure 100 μ m. Upper panel: T2-weighted image (T2WI) and T2*-weighted image (T2*WI) show areas of necrosis (high signal intensity on T2WI and T2*WI and low signal intensity on R2* map). Thin arrows show the sites of necrosis and thick arrows show possible site of accumulated iron positive cells. Middle panel: Representative histological section with similar tumor orientation (within the constraints of the experimental limitations, i.e. 1mm thick MRI slices versus 10 μ thick histological section) show central necrosis (N) in the tumor with areas of iron positive cells (black arrows) seen in the central and peripheral part of the tumor that received iron labeled CTLs. Lower panel: Enlarged view of the boxed areas.

16

Ultrasound Cell Labeling Methods

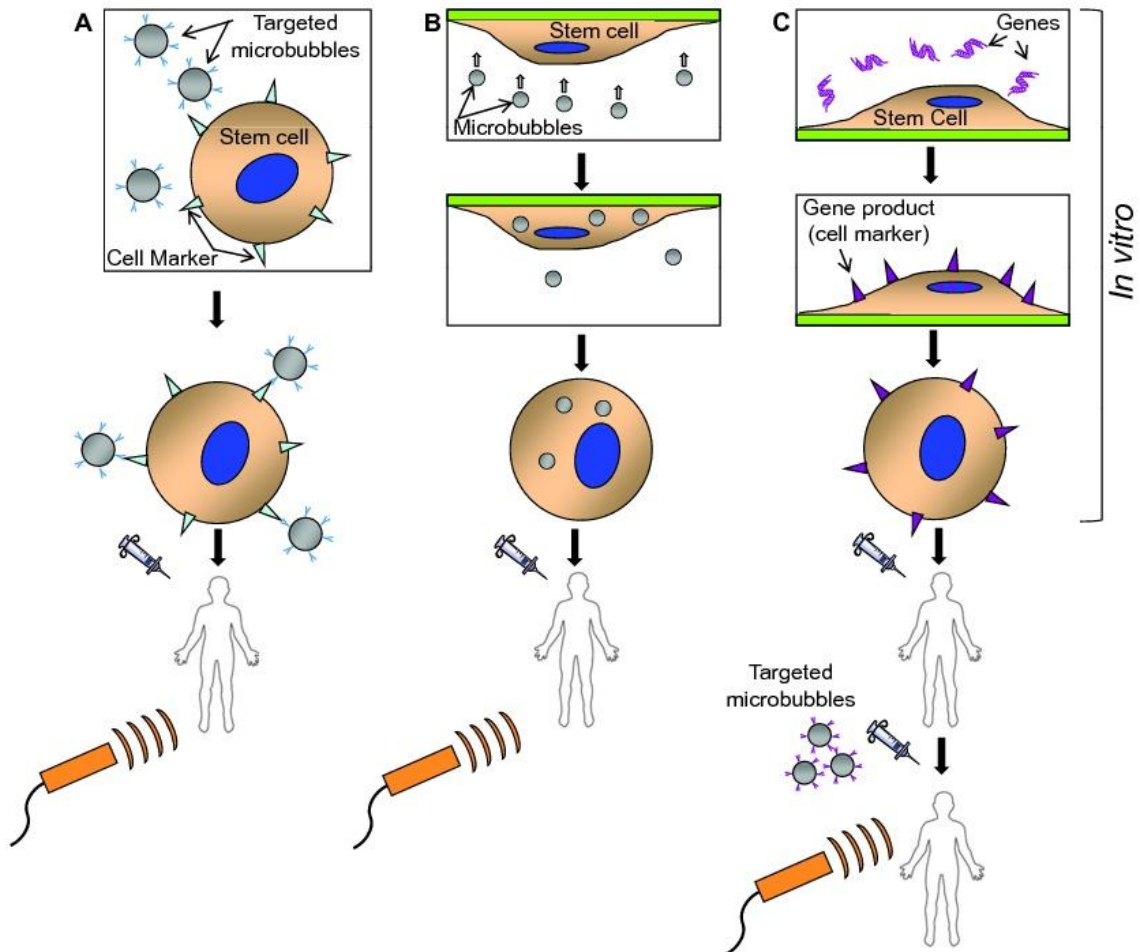


Figure 16.1 Schematic representation of potential approaches to labeling stem cells with microbubbles to enable ultrasound detection. **A** Microbubbles can be attached to the surface of suspended stem cells *in vitro* via a targeting ligand on the microbubble shell that binds to a specific stem cell marker. The labeled cells are then delivered, bearing the microbubbles on the cell surface; **B** Stem cells are labeled *in vitro* by internalization of the microbubbles. In the approach shown, culture plates are inverted, and microbubble interaction with stem cells is achieved by virtue of the buoyant properties of the microbubbles. The labeled stem cells are lifted and delivered, bearing the microbubbles within the cytoplasm; **C** Stem cells are labeled *in vivo*, after delivery, using microbubbles targeted to bind to a cell-specific marker. Prior to delivery, the stem cells are genetically modified *in vitro* to express a unique marker that serves as the microbubble target. Figure not drawn to scale.

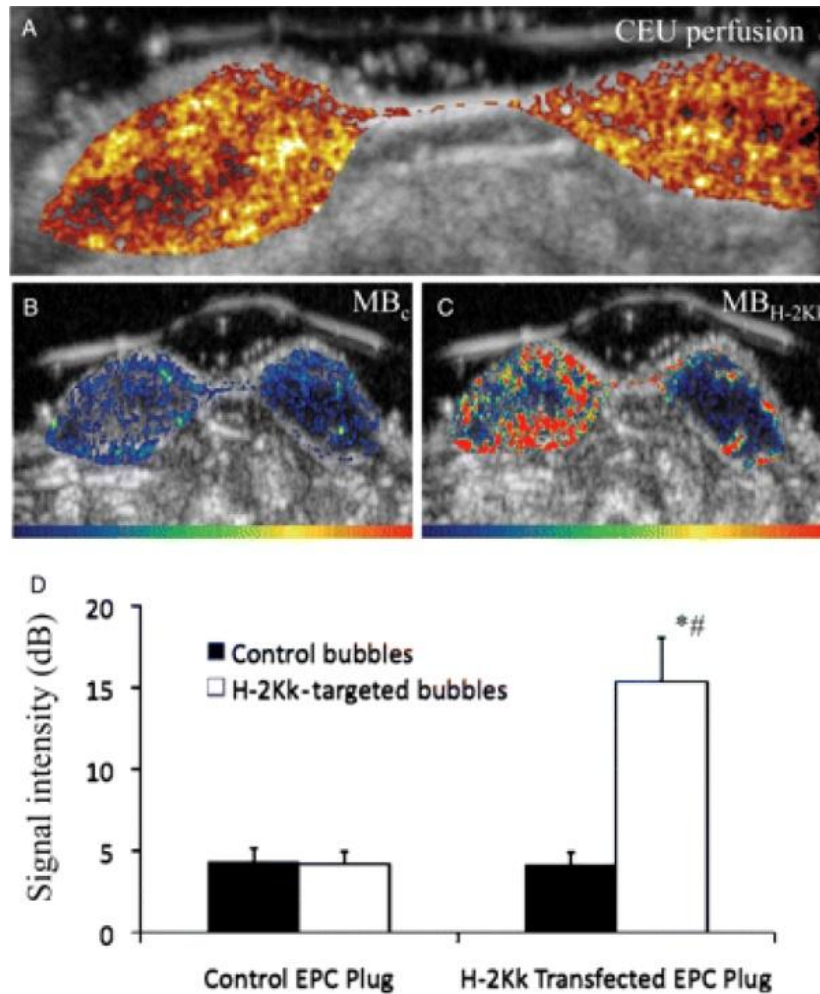


Figure 16.3 Ultrasound cell tracking using *in vivo* labeling of endothelial progenitor cells (EPCs) that were modified *in vitro*, prior to injection, by transfection with the H-2Kk gene. Matrigel plugs subcutaneously injected at 2 sites in rats were supplemented with H-2Kk- transfected EPCs (left plug) or control EPCs (right plug). **A** Background subtracted perfusion imaging of the plugs with non-targeted microbubbles. Delayed imaging of the Matrigel plugs after intravenous injection of **B** control microbubbles or **C** H-2Kk-targeted microbubbles. There was persistent contrast enhancement of the plug supplemented with H-2Kk-transfected EPCs after injection of the H-2Kk-targeted microbubbles. **D** Videointensity measurements of the Matrigel plugs under the various experimental conditions. (From Kuliszewski, M.A., *Cardiovasc Res.*, 83, 653, 2009. With permission.)

17

X-Ray-Guided Delivery And Tracking Of Cells

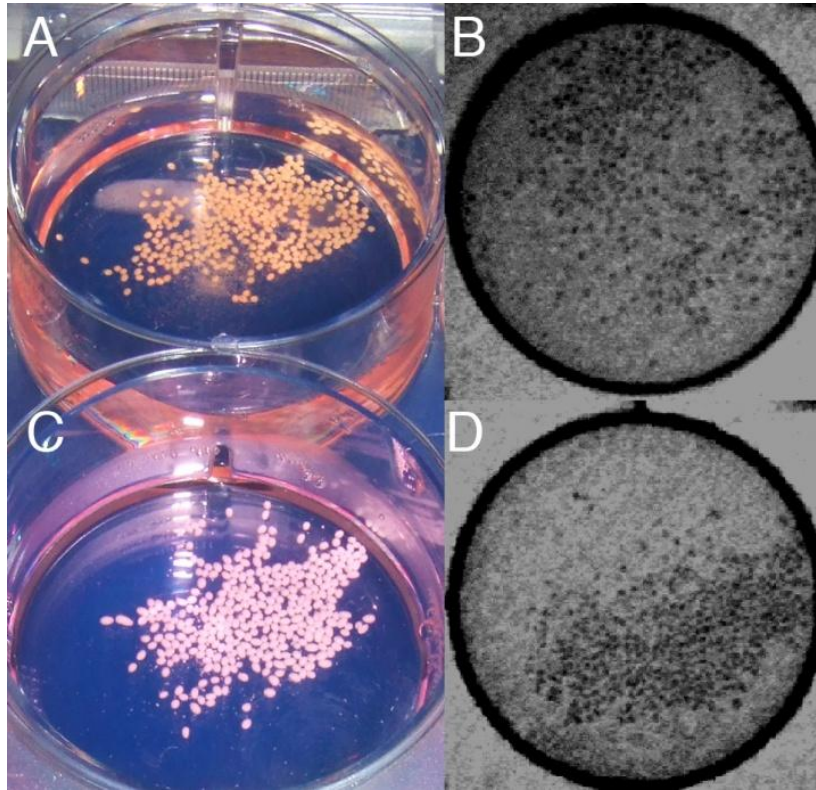


Figure 17.2 Macroscopic (A,C) and fluoroscopic (B,D) images of (A,B) Bi X-Caps and (C,D) Ba X-Caps. Single capsules can be clearly visualized. Reproduced with permission from (Barnett *et al.* 2006).

18

Toward Imaging Of Structure And Function

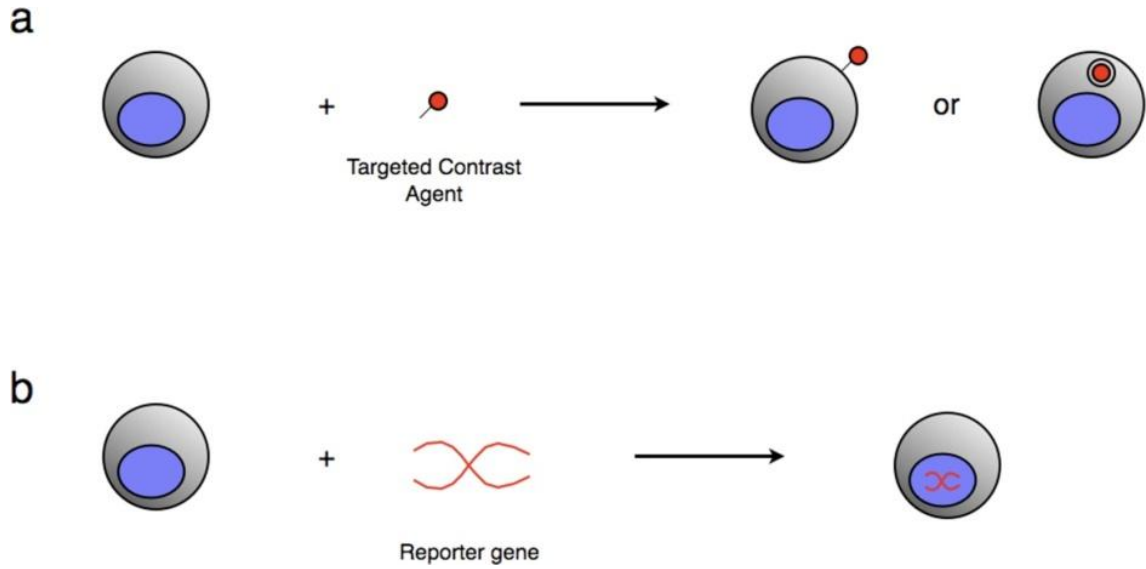


Figure 18.1 (a) Direct and (b) indirect methods of stem cell labeling.

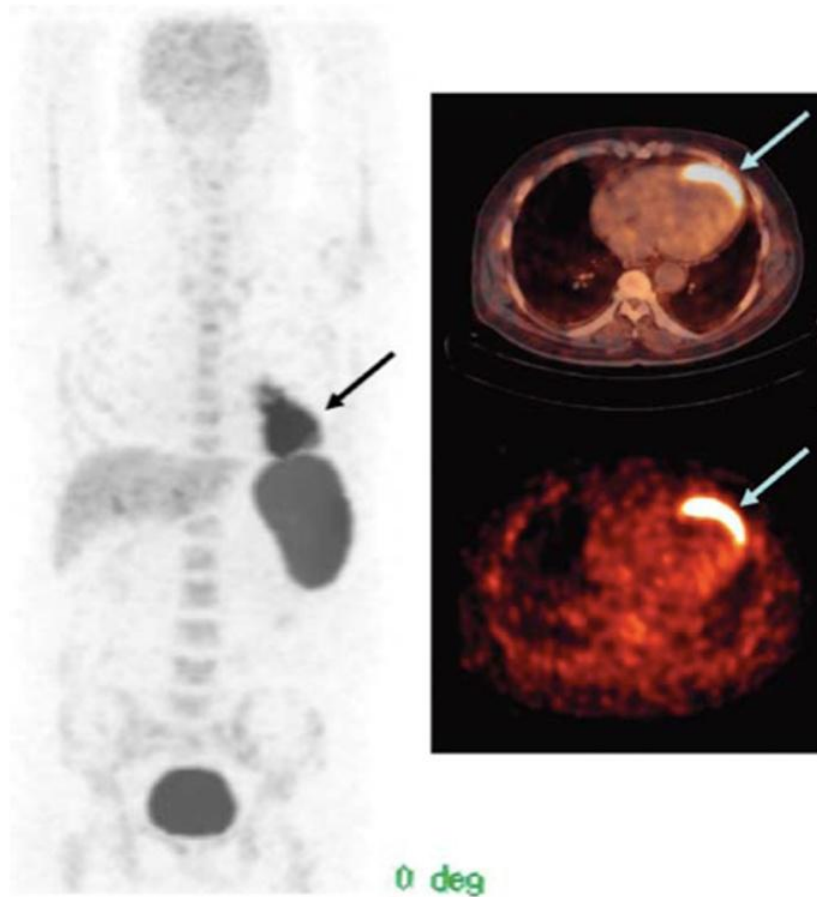


Figure 18.2 PET/CT images of 65-y-old man with history of anterior wall infarction. After percutaneous intervention, ^{18}F -FDG-labeled stem cells were injected via intracoronary catheter. PET/CT images were obtained 2 h after injection. Stem cell accumulation at myocardium is well visualized on transaxial views (arrow). Total amount of stem cells at myocardium was 2.1% of injected dose. Adapted from Figure 2 of (Kang *et al.* 2006).

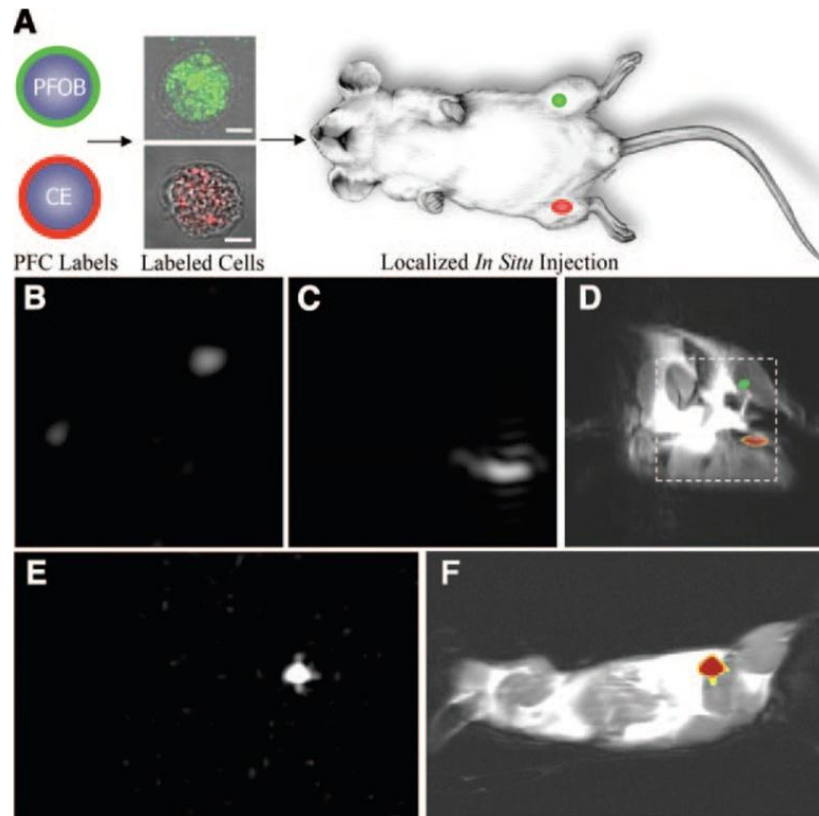


Figure 18.5 Localization of labeled cells after in situ injection by MRS/MRI. **A** To determine the utility for cell tracking stem/progenitor cells labeled with either perfluoro-octylbromide (PFOB, green) or crown ether (CE, red), nanoparticles were locally injected into mouse thigh skeletal muscle. **B–D** At 11.7 T, spectral discrimination permits imaging the fluorine signal attributable to $\sim 1 \times 10^6$ PFOB-loaded (**B**) or CE-loaded cells (**C**) individually, which when overlaid onto a conventional ^1H image of the site (**D**) reveals PFOB and CE labeled cells localized to the left and right leg, respectively (dashed line indicates $3 \times 3 \text{ cm}^2$ field of view for ^{19}F images). **E, F**) Similarly, at 1.5T, ^{19}F image of $\sim 4 \times 10^6$ CE-loaded cells (**E**) locates to the mouse thigh in a ^1H image of the mouse cross section (**F**). The absence of background signal in ^{19}F images (**B, C, E**) enables unambiguous localization of perfluorocarbon-containing cells at both 11.7 T and 1.5 T. Adapted from (Partlow *et al.* 2007).

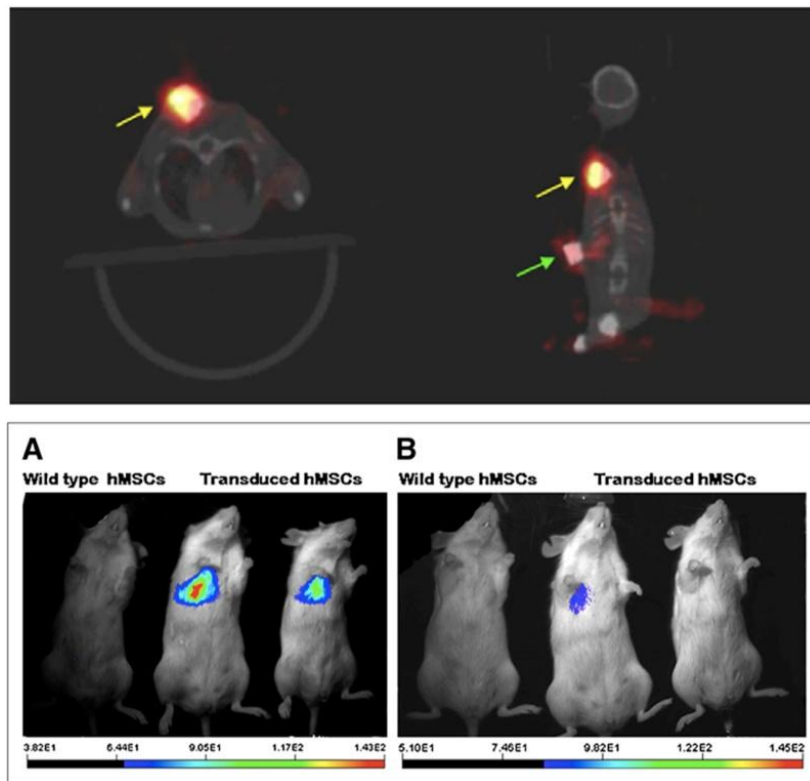
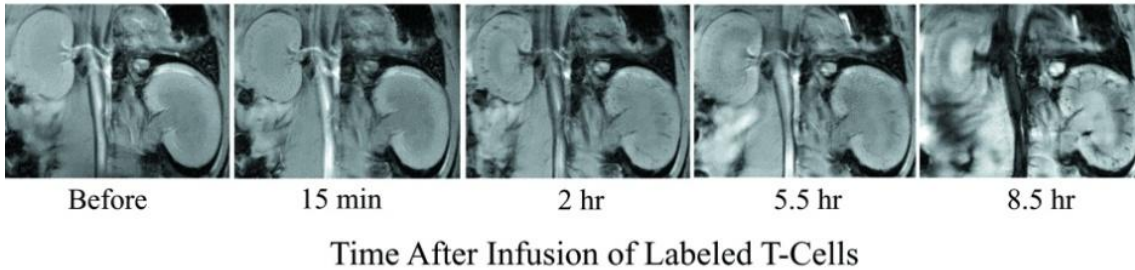


Figure 18.6 Top Overlay of PET (hot-metal pseudocolor) and CT (gray-scale) images: transaxial (left) and coronal (right) views. Although top-row cubes (yellow arrows) had strong PET signals, second-row cubes (green arrow), loaded with mixture of empty-vector-transduced and reporter-transduced hMSCs, had visible signal despite 1:4 dilution. Cubes were also visible on CT images. **Bottom** BLI of tail vein injected hMSCs 30 min after hMSC injection (**A**) and 24 h after hMSC transplantation (**B**). One control animal injected with wild-type hMSCs is shown on left, and 2 animals injected with reporter-transduced hMSCs are shown on right. Scale bar for luminescence intensity is shown at bottom. Adapted from (Love *et al.* 2007).

19

Other Non-Stem Cell Therapies For Cellular Tracking: Inflammatory Cell Tracking

A. MRI



B. Fluorescence

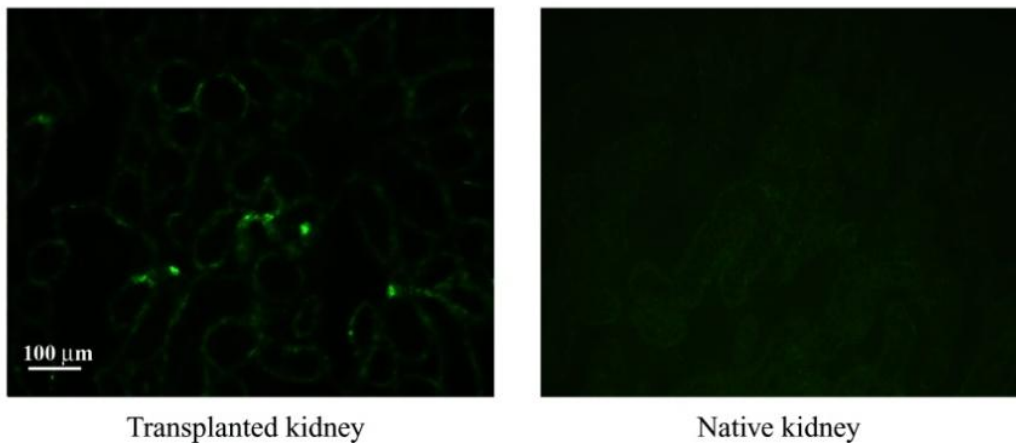
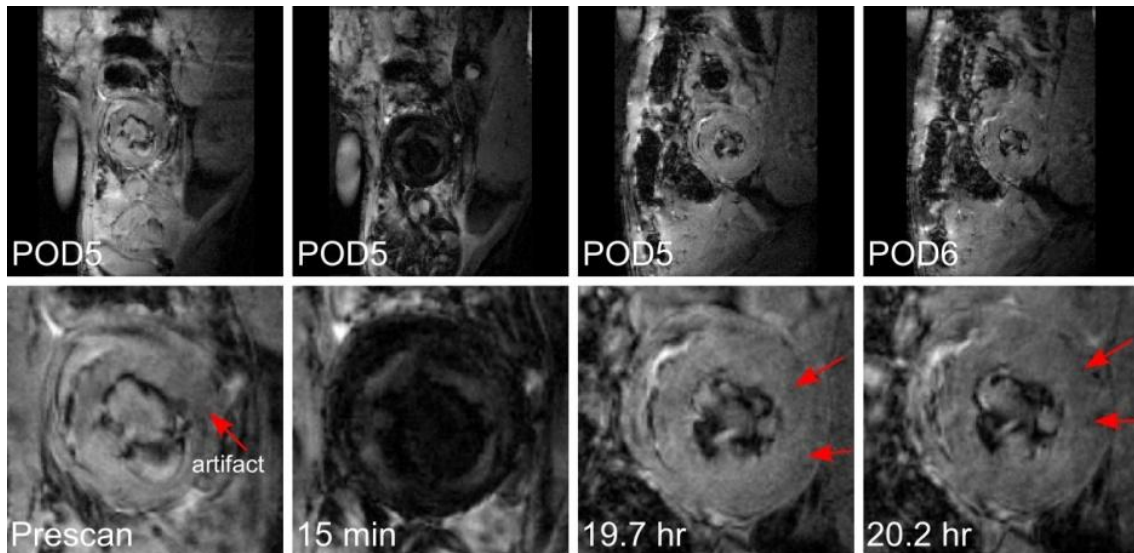


Figure 19.2 **A** Serial gradient-echo MR images of a rat with a transplanted kidney before and after infusion of CL-SPIO-Tat-FITC-labeled T cells on POD 4 where a BN rat was transplanted with a kidney from a DA rat; and **B** the corresponding fluorescence images of the allotransplanted and the native kidneys. A gradient-echo sequence was used to obtain the coronal MR images with the following parameters: TR = 100 ms; TE = 7.3 ms; NEX = 32; matrix size = 256 x 256; FOV = 6.4 x 6.4 cm; slice thickness = 1.4 mm with 0.1 mm slice gap for 5 slices. The MRI experiments were carried out in a 4.7-T Bruker AVANCE DRX MR instrument equipped with a 40-cm horizontal bore superconducting solenoid. [Reprinted from (Ho and Hitchens 2004) with permission].



0.156x0.156x1.5mm 0.156x0.156x1.5mm 0.156x0.156x1.5mm 0.156x0.156x1.2mm
 NA=4 NA=4 NA=4 NA=8

Figure 19.7 *In vivo* MR imaging of a rat allograft heart over time on POD 5 and 6 with Feridex labeling. The top row is the original *in vivo* image of the transplanted heart in the abdominal region. The bottom row is the corresponding magnified image of the heart. **A** The myocardial signal intensity is relatively uniform prior to Feridex injection. **B** The entire heart becomes dark 15 min after the intravenous injection of Feridex as the Feridex remains in the systemic circulation. **C** Focal hypointensity was observed 20 hours after the Feridex injection as the Feridex particles were incorporated into immune cells, mainly macrophages. **D** Thinner imaging slice with more signal averaging (to yield a higher signal-to-noise ratio) at similar time point shows better delineation of the focal hypointensities. Imaging parameter were as follows: TR around 1s, TE=8.1ms, in plane resolution is 156x156 μ m, slice thickness was 1.5 or 1.2 mm, number of average = 4 or 8, total data acquisition time was 14 (average 4) or 28 min (average 8). Arrows show image artifacts.

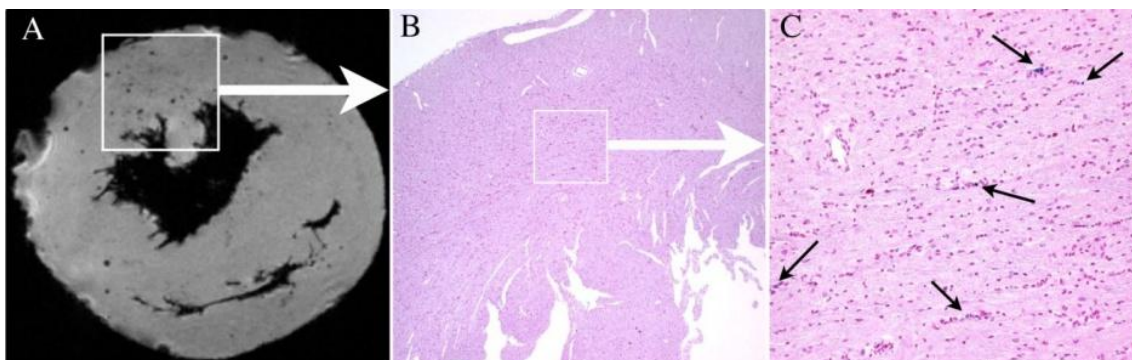


Figure 19.9 Correlation of MRM and iron staining of MPIO in a POD 94 allograft: Image from MRM shows the discrete and circular spots of hypointensity (**A**). These dark spots of hypointensity are due to the presence of MPIO particles, which was confirmed by the matching histological Perl's Prussian Blue sections for iron (**B**, 40X magnification) that correspond to the same area as the boxed region in MRM image (**A**). **C** shows the expansion of the boxed region in B (200X magnification). [Reprinted from Figure 3 of (Ye et al. 2008) with permission.]

20

Bioluminescence, Mri And Pet Imaging Modalities Of Stem Cell-Based Therapy For Neurological Disorders

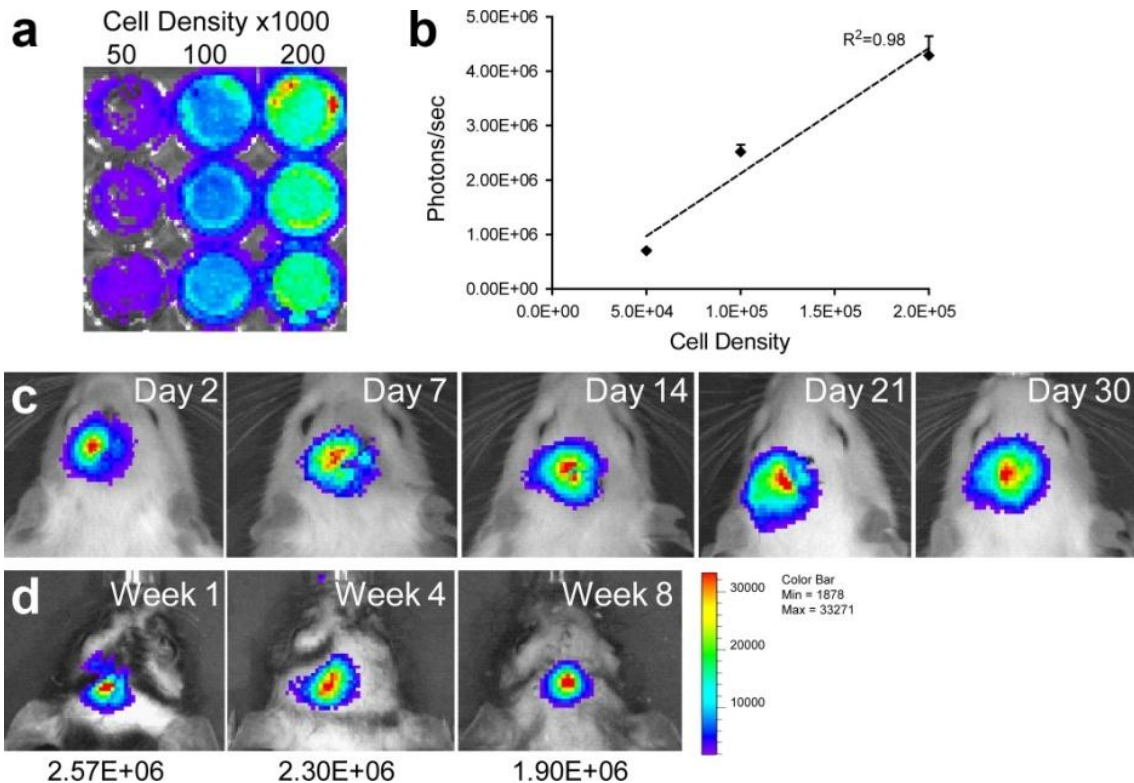


Figure 20.1 In vitro and in vivo bioluminescence imaging of the hNSCs. (a) In vitro imaging analysis of genetically engineered hNSCs show increasing fLuc activity with cell density and a linear correlation ($R^2=0.98$) (b). Data are representative of three independent experiments performed in triplicate. Representative BLI imaging of stroke-lesioned rats transplanted with the hNSCs and monitored for 4 weeks (c) and 8-week post-transplantation survival times (d). Quantitative analysis of the fLuc activity in these animals shows a stable BLI signal, which suggest the survival of the grafts and the non proliferative property of the hNSCs. Color scale bar is in photon/sec/cm²/sr. (reprinted with permission from Daadi *et al.*, *Mol Ther.* 2009 Jul;17(7):1282-91).

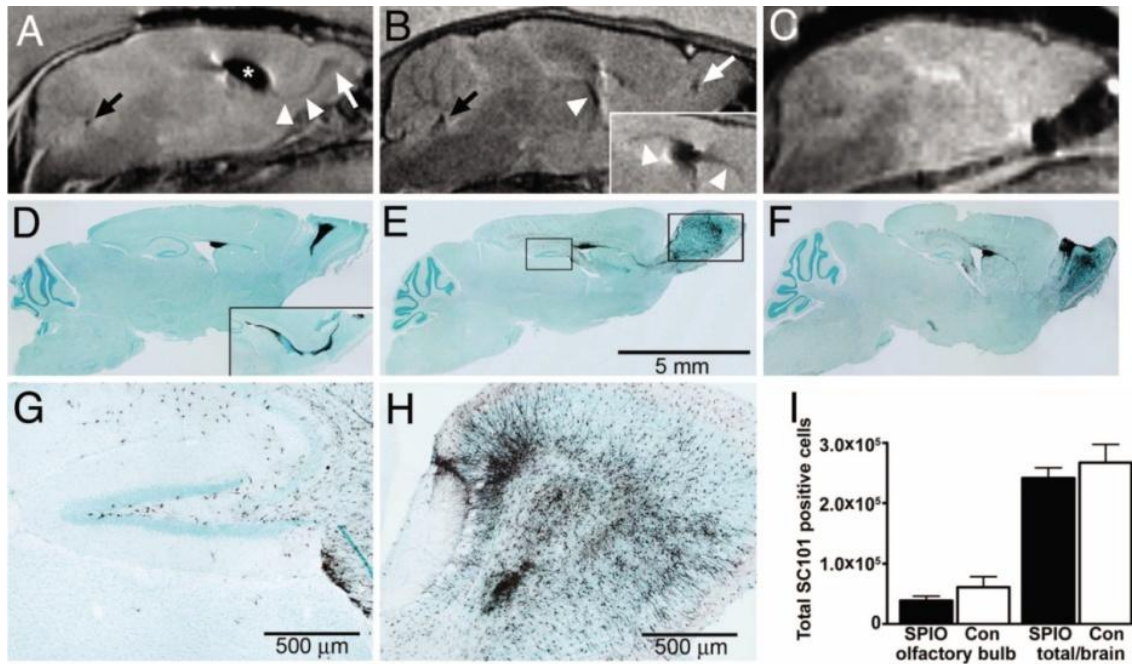


Figure 20.2 Migration and integration of SPIO-labeled human central nervous system stem cells (hCNS-SCNs). MRI detects widespread migration of SPIO-labeled hCNS-SCNs after intraventricular injection in the P0/P1 NOD-SCID mouse brain. (**A** and **D**) (**A**) Three weeks after transplantation, sagittal MRI shows hypointensities representing SPIO-labeled hCNS-SCNs in the lateral ventricle (asterisk), along the RMS, (arrowheads) toward the OB (arrow) and in the 4th ventricle (black arrow). (**D**) corresponding section stained with the human-specific cytoplasmic marker SC121. (Inset) Shows RMS in adjacent section. (**B** and **E**) (**B**) sagittal MRI 18 weeks after transplantation showing that hCNS-SCNs have integrated in the ventricular wall (arrowhead), in the core of the OB (white arrow) and in the fourth ventricle (black arrow). (Inset) Demonstrates migration along the corpus callosum (arrowheads). (**E**) Corresponding histological section. (**C** and **F**) (**C**) sagittal MRI of a control animal transplanted with unlabeled hCNS-SCNs 18 weeks after transplantation shows no cell signal. (**F**) Corresponding histological section. (**G–H**) Higher magnification sagittal images (areas boxed in Fig. **E**) show hCNS-SCNs in the CA1, CA3, and dentate gyrus of the hippocampus (**G**) and in the OB (**H**) of the NOD-SCID mouse. (**I**) There was a robust cell survival at 18 weeks after transplantation without statistically significant difference between SPIO-labeled ($n = 4$ animals) and unlabeled cells ($n = 3$ animals). Results are mean SEM. OB, olfactory bulb; RMS, rostral migratory stream; SVZ, subventricular zone. (reprinted with permission from Guzman *et al.*, *Proc Natl Acad Sci USA*, 2007 Jun 12;104(24):10211-6).

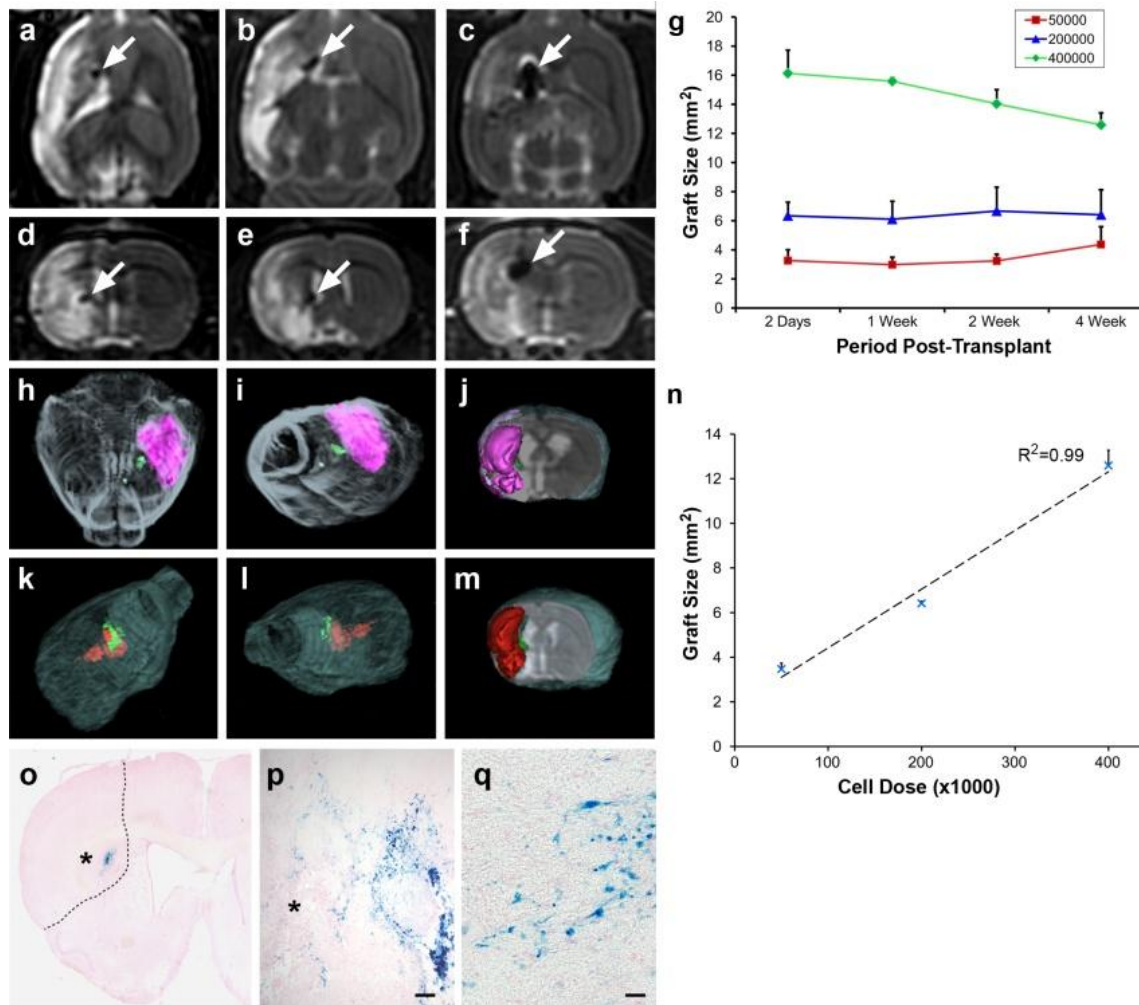


Figure 20.3 MRI imaging analysis of the hNSCs grafts in experimental stroke model. MRI horizontal (a, b, c) and frontal (d, e, f) scans show dose-dependant size of the SPIO-labeled hNSCs grafts as hypointense areas in the striatum (arrow) medially in the penumbral zone of the stroke distinguished as strongly hyperintense areas on T2-weighted images. The cell doses are 50,000 cells (a, d), 200,000 cells (b, e) and 400,000 cells (c, f). (g) Quantitative analysis of graft size, in consecutive coronal MRI scans, 600 μm spaced (Fig. S1, see Materials and Methods section) in the 3 animal groups (n=15) over the post-transplant survival time confirm the BLI imaging data and show a stable graft size demonstrating survival of the graft. Three-dimensional surface rendering reconstruction of grafted rat brain from high resolution T2-MRI illustrate the grafts (green) and stroke (pink, red) in a representative animal from the low-dose (h, i, j) and intermediate-dose group (k, l, m). The MRI measured graft size show a strong correlation ($R^2=0.99$) with the cell dose transplanted (n). (o, p, q) Histological analysis using Prussian blue staining for SPIO particles demonstrate cytosolic deposition of blue crystals in the grafted hNSCs and migration towards stroke area (asterisk in o, p). Interrupted line in o shows the boundary of stroke zone. Bars: (p) 50 μm ; (q) 20 μm . (reprinted with permission from Daadi *et al.*, *Mol Ther.* 2009 Jul;17(7):1282-91).

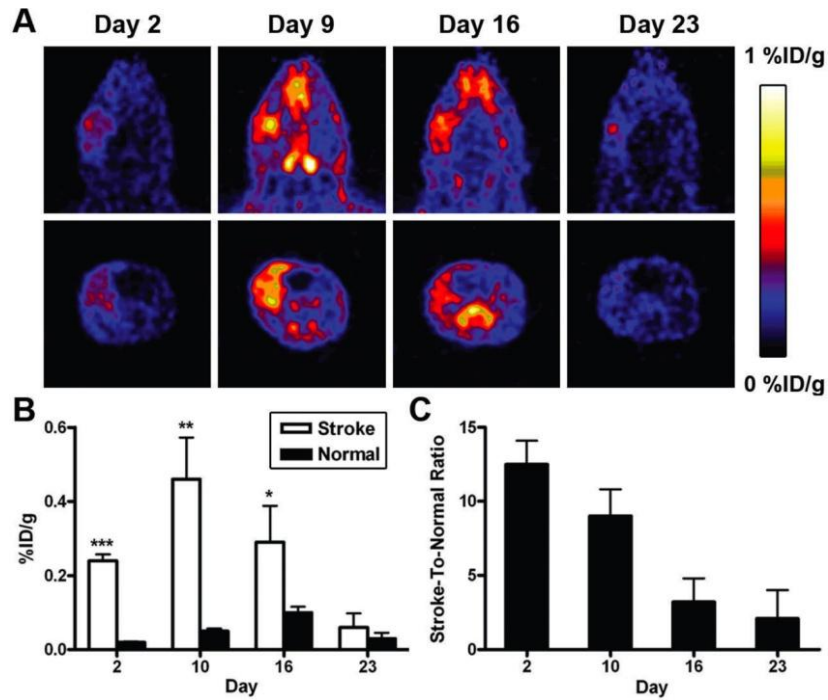


Figure 20.4 ^{64}Cu -DOTA-VEGF₁₂₁ PET of the dMCAo rats. **A** Axial and coronal PET images of the dMCAo rat brain at 2 hours postinjection of 1 mCi of ^{64}Cu -DOTA-VEGF₁₂₁. **B** ^{64}Cu -DOTA-VEGF₁₂₁ uptake in the stroke area and the contralateral brain. **C**, The ratio of ^{64}Cu -DOTA-VEGF₁₂₁ uptake in the stroke area vs the contralateral brain. n = 4; *P 0.05; **P 0.01; ***P 0.001. (reprinted with permission from Cai *et al.*, *Stroke*. 2009 Jan;40(1):270-7).

21

Clinical Application Of Non-Invasive Molecular Imaging In Cancer Cell Therapy: The First Reporter Gene Based Imaging Clinical Trial

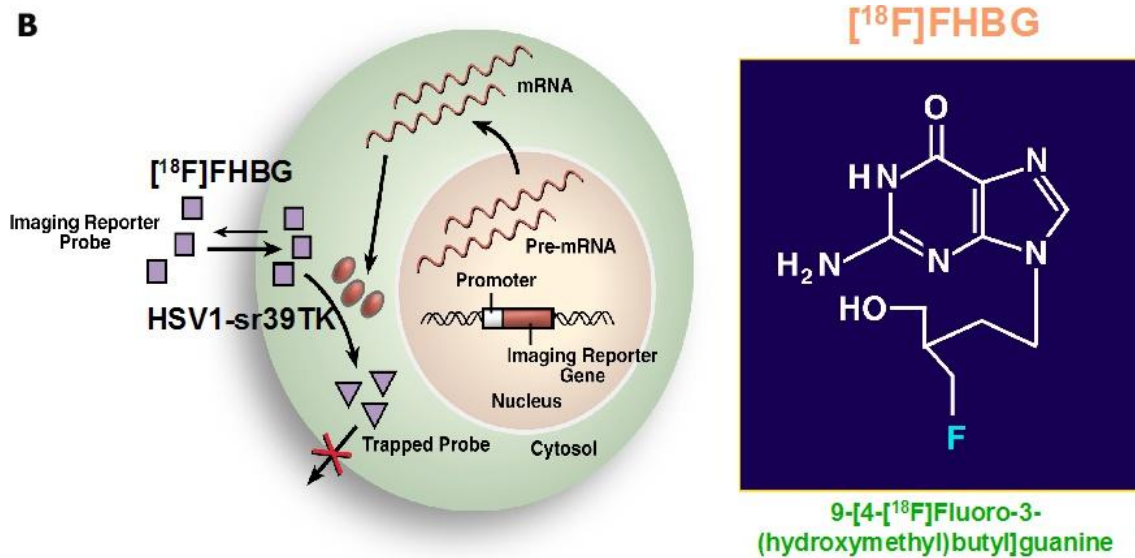


Figure 21.1 Diagram illustrating the mechanism of imaging an enzyme based PRG. HSV1-sr39tk is a mutant of Herpes Simplex virus type 1 thymidine kinase (HSV1-tk). The PRG HSV1-sr39tk, encodes the enzyme HSV1-sr39TK that can phosphorylate acycloguanosine and uracil nucleoside analogs. [¹⁸F]FHBG, a side-chain fluorine-18 radiolabeled analog of the drug Penciclovir, is an acycloguanosine analog, most efficiently phosphorylated through HSV1-sr39TK enzyme catalysis. Upon phosphorylation, [¹⁸F]FHBG cannot cross the membrane; hence cells expressing HSV1-sr39tk entrap [¹⁸F]FHBG. Above background accumulation of [¹⁸F]FHBG in the tissues of living mammals is an indication of the presence of HSV1-tk or HSV1-sr39tk expressing cells within the tissues.

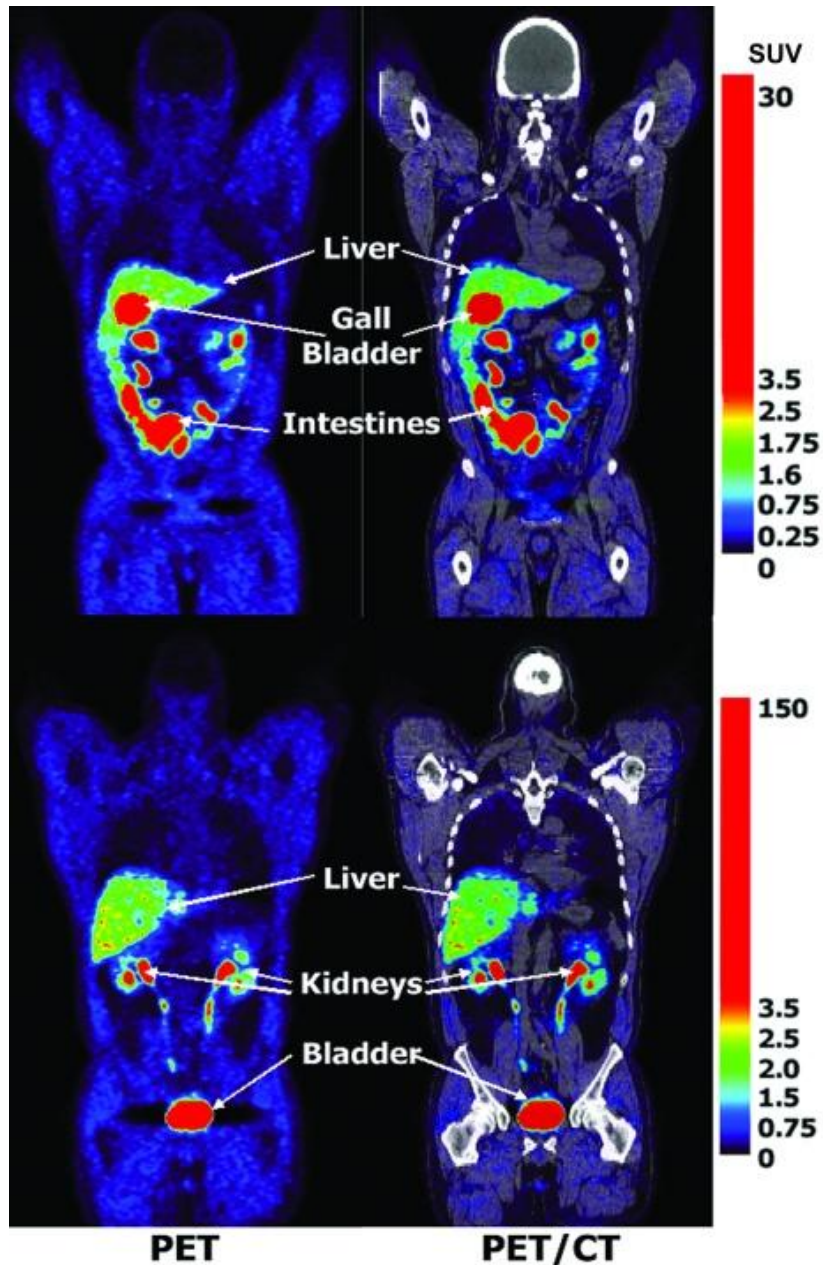


Figure 21.2 Whole-body PET and PET/CT images of [^{18}F]FHBG biodistribution in a human, two hours after its intravenous injection. Two coronal slices are shown to illustrate activity within the liver, gall-bladder, intestines, kidney's and bladder, which are organs involved with [^{18}F]FHBG's clearance from the body. Background activity in all other tissues is relatively low, due to the absence of HSV1-tk or HSV1-sr39tk expressing cells within the body of this human volunteer.

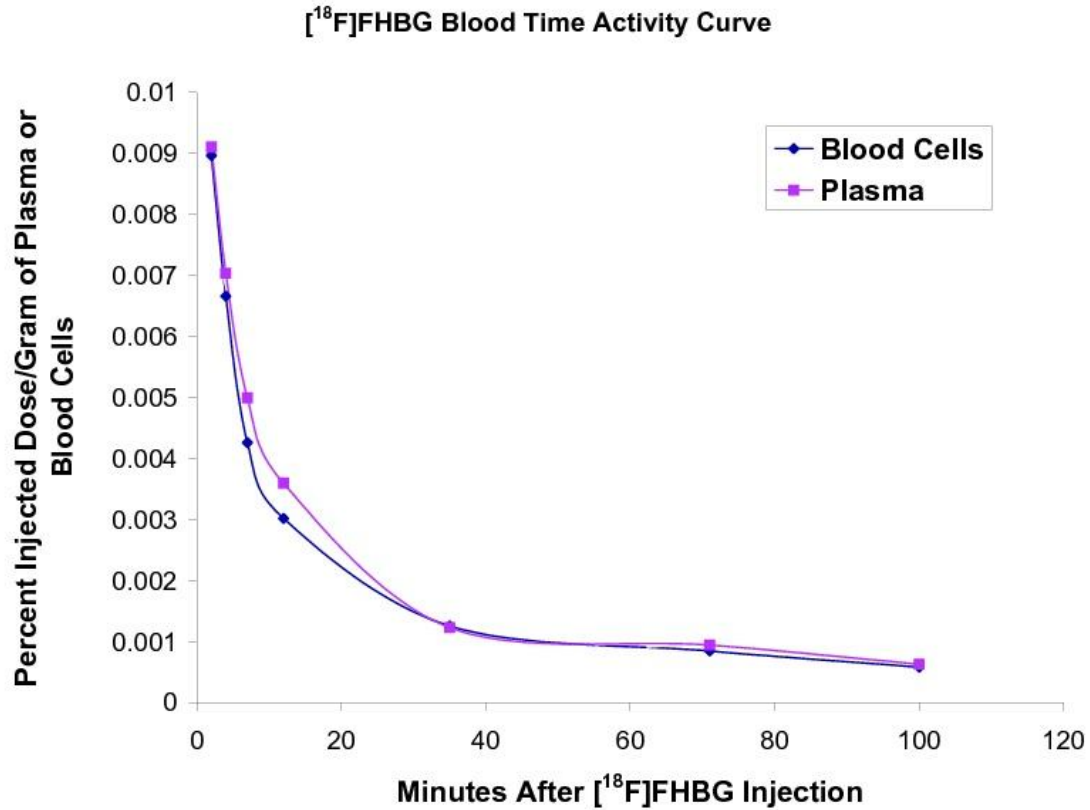


Figure 21.3 Blood time activity of [¹⁸F]FHBG in a female glioma patient volunteer. Half of the radiolabeled probe is cleared from plasma and blood cells in less than 10 minutes and only about 10% of the original activity is present after 40 minutes. Radioactivity measurements were decay corrected back to the injection time.

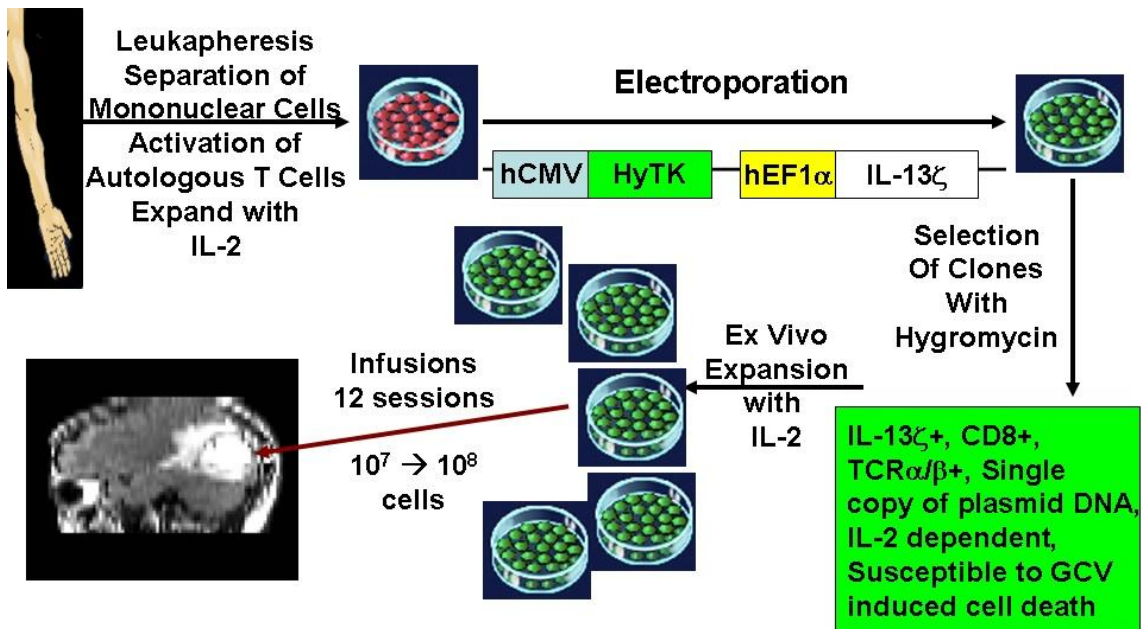


Figure 21.5 Description of the procedures involved in the preparation of genetically engineered CTLs and their infusion into the recurrent glioma tumor resection site.

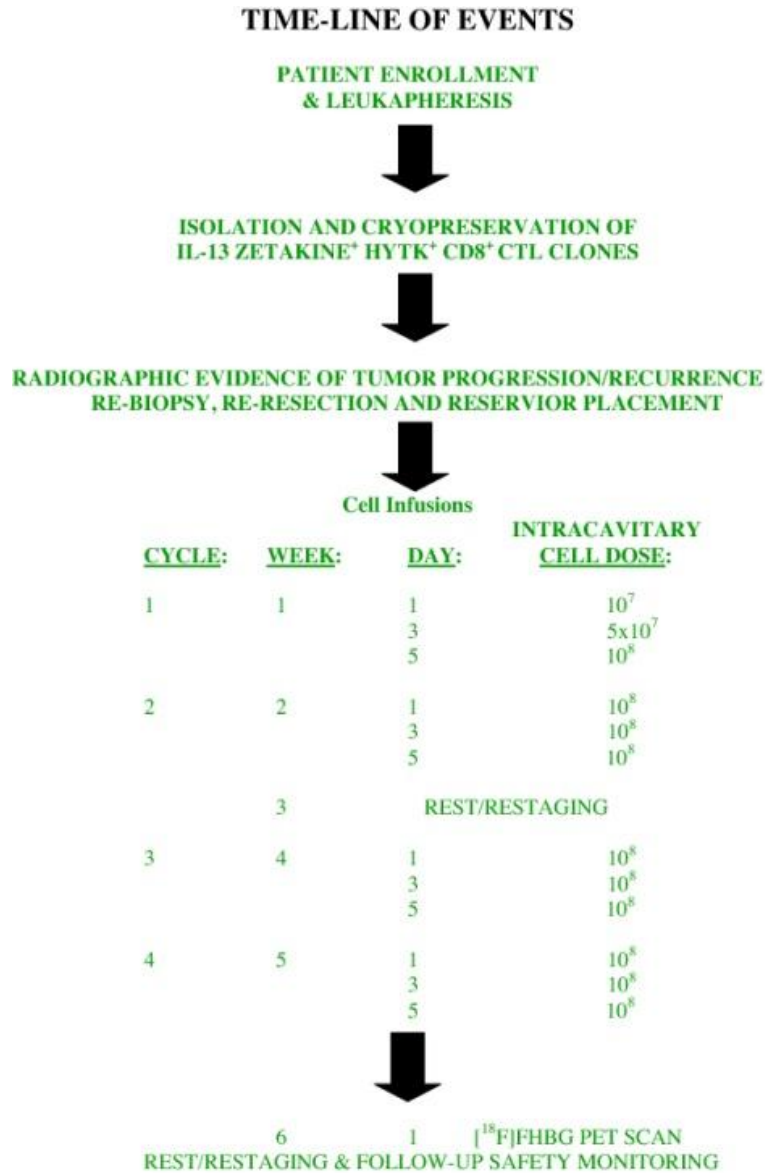


Figure 21.6 Time-line of CTL therapy and [¹⁸F]FHBG imaging

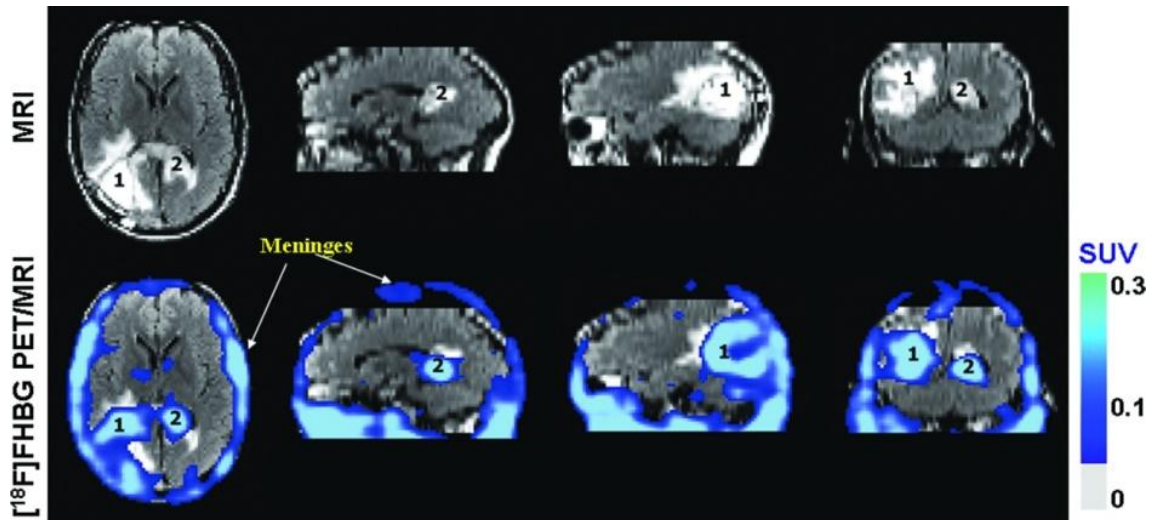


Figure 21.7 MRI and PET over MRI superimposed brain images of CTL patient #1. Images were acquired approximately two hours after $[^{18}\text{F}]\text{FHBG}$ injection. The patient had a surgically resected tumor (1) in the right parietal lobe and a new non-resected tumor in the center (2), near corpus callosum of his brain. The infused cells had localized at the site of tumor 1 and also trafficked to tumor 2. $[^{18}\text{F}]\text{FHBG}$ activity is higher than the brain background at both sites. Background $[^{18}\text{F}]\text{FHBG}$ activity is low within the Central Nervous System due to its inability to cross the blood brain barrier. Background activity is relatively higher in all other tissues. Activity can also be observed in the meninges. The tumor 1/meninges and tumor 2/meninges $[^{18}\text{F}]\text{FHBG}$ activity ratio in this patient was 1.75 and 1.57, respectively. Whereas the average resected tumor site/meninges and intact tumor site to meninges $[^{18}\text{F}]\text{FHBG}$ activity ratio in control patients was 0.86 and 0.44, respectively.

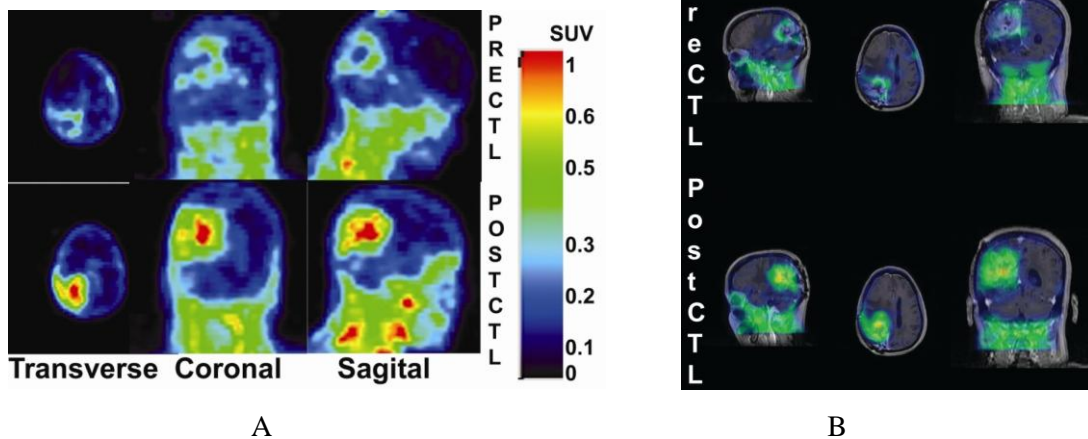


Figure 21.8. **A** $[^{18}\text{F}]\text{FHBG}$ PET images of the head of CTL patient #2, prior to initiation of CTL infusions and three days after completion of all CTL infusions. **B** $[^{18}\text{F}]\text{FHBG}$ head PET images superimposed over corresponding MRI images of CTL patient #2, illustrating increased $[^{18}\text{F}]\text{FHBG}$ accumulation after CTL infusions at the recurrent tumor resection site. Images acquired approximately 2 hours after bolus intravenous $[^{18}\text{F}]\text{FHBG}$ injection.

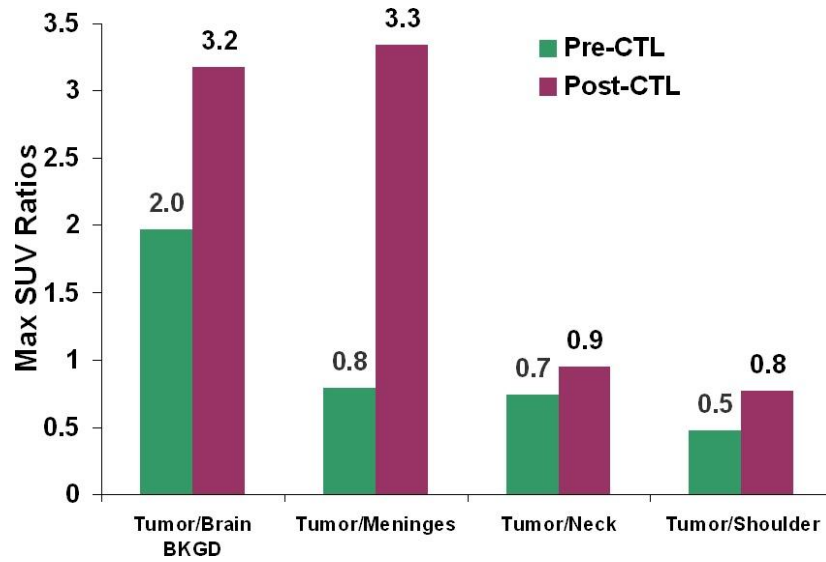


Figure 21.9 Ratios of ^{18}F FHBG signal intensity in tumor resection site over a brain background site, the surrounding meninges, neck and shoulder. All of the ratios increased after CTL infusions.

22

Clinical Cardiology Stem Cell Applications

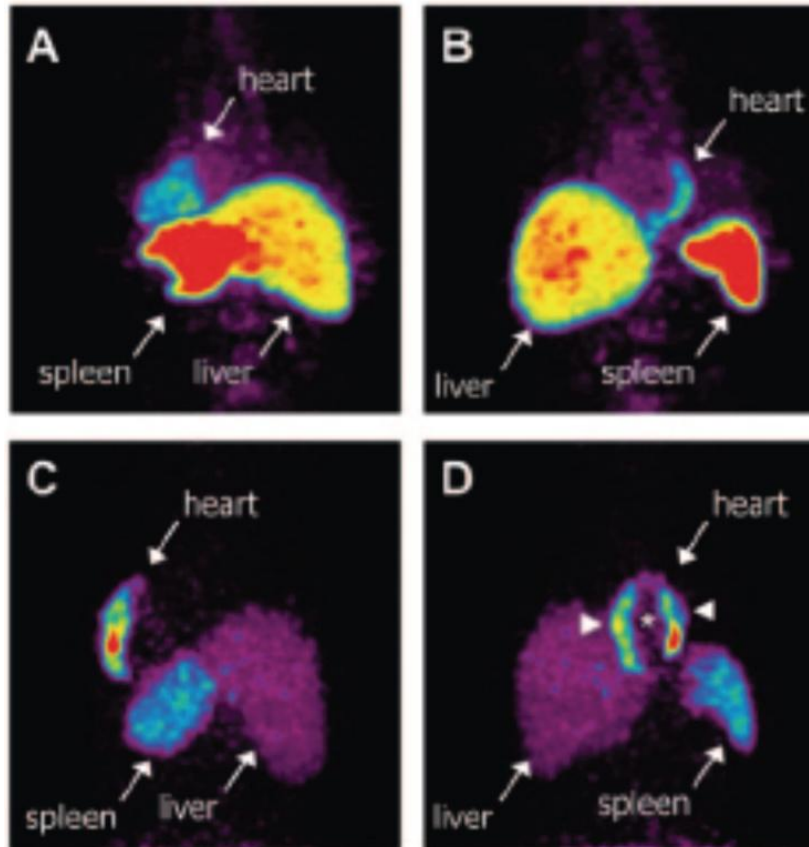


Figure 22.1 Left posterior oblique (A) and left anterior oblique (B) views are shown of the chest and upper abdomen of patient 2 taken 65 minutes after transfer of ^{18}F -FDG labeled, unselected BMCs into left circumflex. BMC homing is detectable in the lateral wall of the heart (infarct center and border zone), liver, and spleen. Left posterior oblique (C) and left anterior oblique (D) views of chest and upper abdomen of patient 7 taken 70 minutes after transfer of ^{18}F -FDG-labeled, CD34-enriched BMCs into left anterior descending coronary artery. Homing of CD34-enriched cells is detectable in the anteroseptal wall of the heart, liver and spleen. CD34-cell homing is most prominent in infarct border zone (arrowheads) but not infarct center (asterisk).

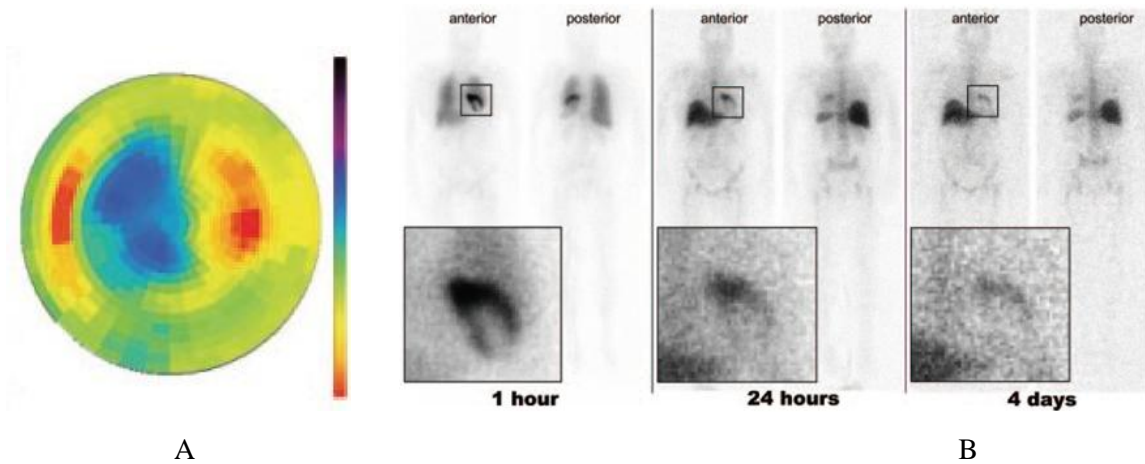


Figure 22.1 Clinical imaging of injected cells radiolabeled with Indium¹¹¹. The pictures and legend are verbatim from a paper published in *Circulation* (Schächinger et al)⁷² **A** FDG-PET imaging: Dark scale indicates low viability. **B** Imaging of ¹¹¹In distribution with gamma camera at 1 hour, 24 hours, and 4 days after infusion of ¹¹¹In-oxine-labeled CPCs. Anterior and posterior whole-body scans were acquired. The inserts show the heart at a higher magnification. Cardiac ¹¹¹In activity was highest immediately after infusion and progressively diminished in the lung and heart during the next days.